Acoustophoresis-assisted Fluid Jet Polishing

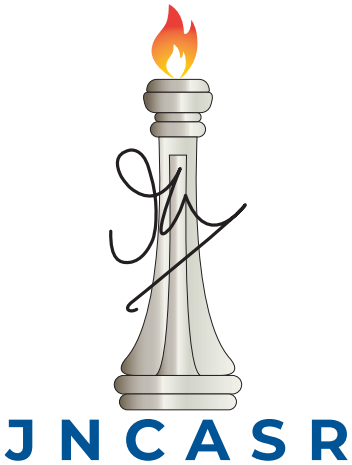

Anomitra Saha

Engineering Mechanics Unit
Jawaharlal Nehru Centre for Advanced Scientific Research

This dissertation is submitted for the degree of
M. S. (Engg.)

December 2024

Declaration

I hereby declare that except where specific reference is made to the work of others, the contents of this dissertation are original and have not been submitted in whole or in part for consideration for any other degree or qualification in this, or any other university. This dissertation is my own work and contains nothing which is the outcome of work done in collaboration with others, except as specified in the text and Acknowledgements.

Anomitra Saha
December 2024

CERTIFICATE

I hereby certify that the matter embodied in this thesis entitled **Acoustophoresis-assisted Fluid Jet Polishing** has been carried out by **Mr. Anomitra Saha** at the Engineering Mechanics Unit, Jawaharlal Nehru Centre for Advanced Scientific Research, Bengaluru, India under my supervision and that it has not been submitted elsewhere for the award of any degree or diploma.

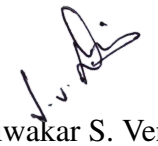

Dr. Diwakar S. Venkatesan
(Research Supervisor)

Acknowledgements

I want to start by first acknowledging my thesis supervisor, Dr. Diwakar S. Venkatesan, for giving me an exciting problem to work on. I am grateful to him for introducing me to acoustophoresis, giving me complete freedom to explore the problem, and for his support throughout my master's. I thank my course instructors, Prof. Ganesh Subramanian, Prof. K. R. Sreenivas, and Prof. Jaywant Arakeri, for their courses.

I owe a debt of gratitude to Dr. Abhijit Dhamanekar, without whose tutelage I could not have completed my work on the full spectrum of numerical simulations.

Regarding the theoretical discussion of my work, I am grateful to Dr. Pavan K. Singeetham and Sanagmesh for their indulgence.

Abstract

The current work proposes a novel technique of acoustophoretic-assisted Fluid Jet Polishing (FJP). The underlying principle involves migrating abrasive particles to desired locations (pressure nodes) within the jet using standing acoustic waves. The migration of particles occurs on account of the radiation force arising from the difference in the acoustic impedance of the particles and the carrier fluid. The current work analyzes the proposed FJP procedure using multiphase simulations involving a combination of Eulerian and Lagrangian approaches. The influence of acoustophoresis on circular and square cross-sectioned nozzles has been primarily evaluated. Though the pressure nodes in circular nozzles can help achieve precise annular erosion, they do not alter the inhomogeneous W-shaped erosion profile usually observed in conventional FJP systems. In contrast, the acoustic forcing in square cross-section nozzles propels the particles toward the jet axis, thereby manifesting a U-shaped erosion profile for specific operating conditions that have been identified via a systematic analysis. Such particle focussing/redistribution capabilities provide a unique means of controlling erosion, removing machining inhomogeneity, and enhancing the material removal rate during the FJP process.

Table of contents

List of figures

List of tables

Chapter 1

Introduction

1.1 General Overview

Machining or polishing processes that aim to remove or minimize surface imperfections are indispensable to many manufacturing systems. Surface polishing is generally carried out not only to increase the aesthetic appeal of products but also to perform various functional tasks such as reduction of friction, corrosion protection, and enhancement of durability. The extent of surface polishing ranges from coarse processes such as milling and grinding to refined procedures such as mechanical, chemical, electrolytic, ultrasonic, laser, and fluid jet polishing. In the current work, we focus on the last mentioned technique, i.e. Fluid Jet Polishing (FJP), wherein we address some of its challenges through a novel approach involving acoustophoresis. Before proceeding with the details of FJP and the proposed improvisation, we briefly review the other salient methods mentioned above.

(a) **Milling** (Fig. 1.1) is a process of eliminating material from a workpiece by advancing the cutter into the workpiece. The rapidly spinning cutter, with several teeth, is slowly pushed through the workpiece in a direction perpendicular to the axis of spin. With each pass of the milling cutter, the tool's cutting edges are repeatedly sliced into the material, shearing off chips from the workpiece.

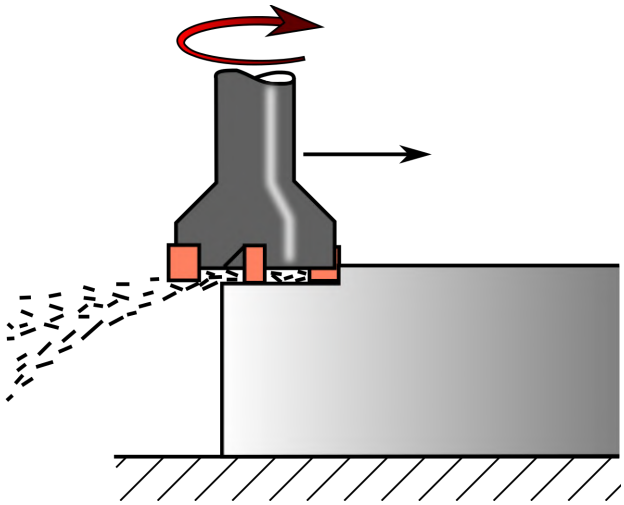

Fig. 1.1 Schematic of Face milling process (source:Wikipedia)

(b) **Grinding** (Fig. 1.2) is an intricate abrasive machining process that involves a rotating grinding wheel made of abrasive particles that act as miniature cutting tools. As the rotating grinding wheel comes in contact with the workpiece and passes over it, it removes a thin layer of material, achieving the desired shape and size. Critical components of a grinding operation include the rotating grinding wheel, the workpiece, and the coolant to reduce thermal damage due to heat generated during grinding.

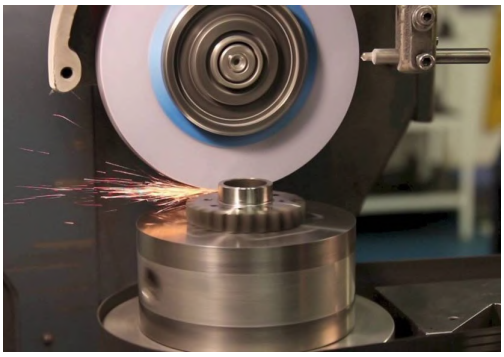

Fig. 1.2 Precision Grinding (source:at-machining.com)

(c) The process of polishing a surface involves minimizing or eliminating flaws such as unevenness, markings, and scratches in order to refine and improve it. The goal is to produce surfaces that are aesthetically pleasing, reflecting, and smooth. This method is used in several industries, such as automotive & optical components, woodworking, and jewellery polishing. There are several sub-techniques under this category and these are given below.

1. **Mechanical/Abrasive Polishing** - This technique uses instruments like polishing wheels, belt sanders, and rotary tools for a controlled and exact polishing operation.

2. **Chemical Polishing** - This technique, as shown in Fig. 1.3, involves using specialized chemical compounds to eliminate thin layers of the metal's surface, providing an improved and aesthetically appealing exterior.

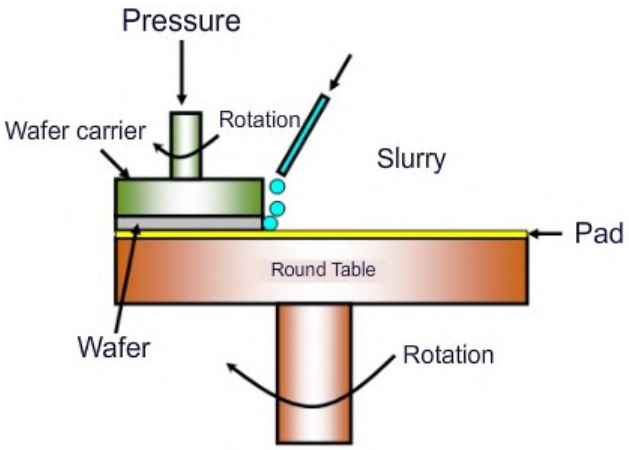

Fig. 1.3 Schematic of Chemo-mechanical polishing (source: Google)

3. **Electrolytic Polishing** (Fig. 1.4) - This process involves the application of an electric current to dissolve and remove surface imperfections using an electrolyte solution.

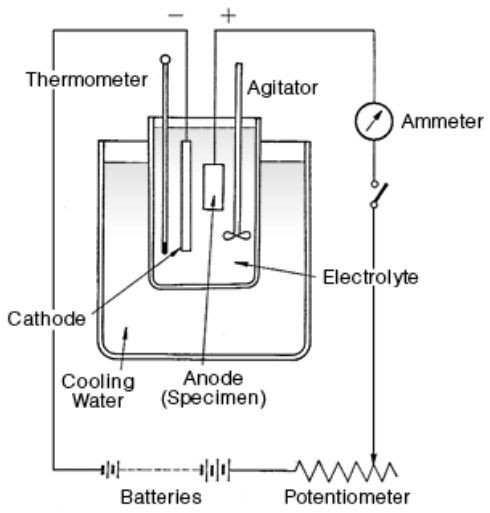

Fig. 1.4 Schematic of Electrolytic polishing (source:misumi-techcentral.com)

4. **Ultrasonic Polishing** - This non-traditional method leverages high-frequency vibrations to generate microscopic abrasive action on the surface being polished.

5. **Laser Polishing** - This technique (Fig. 1.5) employs a focused laser beam to selectively melt the surface of a material, resulting in a polished appearance.

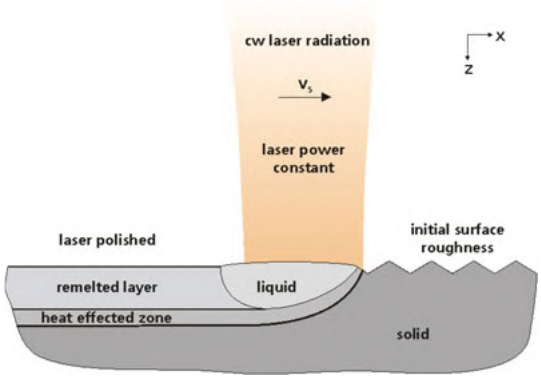

Fig. 1.5 Schematic of Laser polishing (source:sylas.com)

6. **Fluid Jet Polishing** - In this process, pressurized fluid with abrasive particles is issued from a nozzle and is impacted on the workpiece to polish or generate the desired pattern. Since FJP is the focus of the present work, we will discuss the phenomenon in more detail in the following section.

1.2 Fluid Jet Polishing (FJP)

FJP is a versatile procedure of impinging a surface with abrasive particles laden fluid jet, wherein the impact and shearing action between the erodents and the workpiece results in material removal (Fähnle *et al.* [23]). FJP is especially relevant in ultra-precise applications like polishing of micro-lens mold arrays, micro-channels, and micro-cusps. The material removal rate of the FJP process is quite predictable and easily controllable, thus allowing for intricate procedures like the deterministic finishing and the generation of functional surfaces with sub-micrometre resolution.

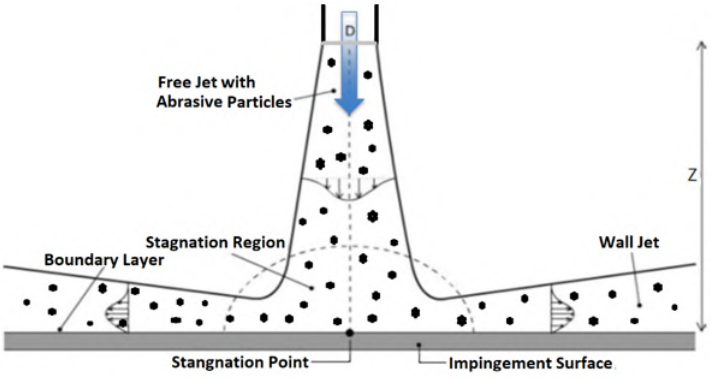

Fig. 1.6 Schematic of Fluid Jet Polishing

The fundamental idea behind FJP is derived from two quite distinct processes: bowl feed polishing and abrasive slurry jet machining. Slurry jet machining allows the cutting of both ductile and brittle materials due to the utilization of extremely high-pressure feeds. The machined surface produced is, however, of poor quality. On the contrary, bowl feed polishing results in a superior surface quality because of the significantly reduced impact force of the abrasive particles against the lap. Fluid jet polishing is an intermediate method that can be used to both shape and polish. It typically uses a low-pressure slurry jet. Since the particles move relatively slowly over the surface, the surface quality is substantially better than abrasive jet machining.

1.2.1 Salient characteristics of FJP

The removal of material in FJP is strongly linked to the hydrodynamics of jet impingement flow. The main zones in a jet impingement have been described below:

1. The area of the jet that is undisturbed by the impingement surface is known as the "free jet zone." A shear layer encompassing a potential core makes up the free jet zone. The shear layer has little effect on the fluid velocity or turbulence intensity within the jet's potential core. Both the jet's radial spread and core diameter decrease as a result of the shear layer entraining the surrounding fluid and producing significant levels of turbulence. A reduction of centre-line velocity and an increase in turbulence is observed at the downstream of the jet's potential core.

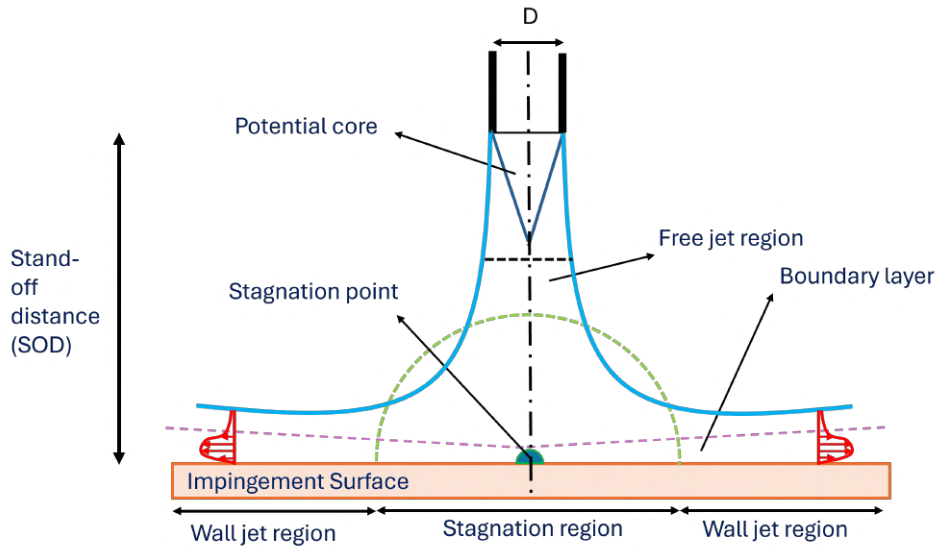

Fig. 1.7 Schematic of Jet Impingement

2. The impingement of the jet on the target surface creates a stagnation zone. Here, the jet's axial velocity reduces, and it is diverted in the radial direction within the stagnation zone. This zone begins when the jet's axial velocity decreases owing to the surface impact. Fitzgerald & Garimella [29] showed that in the vicinity of the target, i.e., H/D < 1.5, there is a rapid drop in the centre-line velocity as a result of the stagnation zone.

3. In the Wall Jet zone, the fluid accelerates horizontally. Here, the jet travels radially outward along the plate, entraining the surrounding air.

The particle carrying capacity of a fluid jet heavily influences the particle trajectories and the subsequent erosion profile. One way to characterize this entrainment relation between the carrying fluid and solid particles is using the Stokes number (St), defined as

$$St = \frac{\text{Particle's relaxation time}}{\text{Flow time scale}}. \tag{1.1}$$

When a flow has a high St, the particles have a high relaxation time. This means that the fluid flow cannot effectively entrain the particles, causing the particles to cross instead of following the fluid's streamlines. Conversely, low St flows more closely follow the streamlines because of the high entrainment capacity brought on by the particles' short relaxation times. In typical FJP systems, liquid-solid flow is considered to be in the low St category. Thus, the abrasives follow the streamlines, deviating away from the stagnation point.

The merits of the conventional FJP process have been listed below.

1. Relatively low erosion of machining tool due to FJP being a non-contact process.

2. Both roughness reduction and shape corrections are possible with one method.

3. Even complicated aspherical surfaces can be polished with FJP if proper time is allocated over the entire surface to ensure uniform material removal.

4. The slurry can be recycled, making the method environmentally friendly.

5. Temperature is well-regulated during the process.

6. Erosion profile can be customized with the use of nozzles with different dimensions.

Flipping to the other side, the main flaw of the FJP occurs at the stagnation point. It is devoid of any particle impacts owing to the fluid velocity being zero, which, in turn, makes the material removal process spatially inhomogeneous. The problem of spatial inhomogeneous erosion profile is amplified by random particle impacts due to the turbulence of the jet. This

typically results in a W-shaped erosion profile, whereas a U-shaped profile would be ideally desired from the FJP process. In addition, the erosion rate here is quite modest in comparison to other conventional polishing methods, thus requiring a longer time to complete a job. Plus, the number of particles impacting the desired area is quite small compared to the number of particles injected in the flow stream, signalling a significant wastage of abrasive particles. Also, there is considerable erosion of the nozzle wall as the particles are homogeneously dispersed inside the nozzle, which reduces the nozzle life and inhibits the repeatability of the machining.

Over the course of the last two decades, several diverse improvisations have been suggested to overcome the said drawbacks. Some of them will be discussed in the next chapter. In the current work, we propose a novel acoustophoretic-assisted FJP procedure. In this technique, the abrasive particles in the fluid media are redistributed within the nozzle using acoustic radiation pressure. Before proceeding further, we briefly look into the applications of FJP.

1.2.2 Applications of FJP

Polishing of optical Micro-Lens molds

Precision molds and mold grids are essential technical enablers for a wide range of manufacturing divisions, including fibre optic end-connectors, telecommunication terminals, cellphones, endoscopes, and consumer cameras (see fig(1.8)). In order to satisfy the strict criteria of form accuracy (< 60 nm P-V) and surface roughness (< 2 nm Ra) (Ra is a measure of average roughness given by the deviation of a surface from a mean height), post-polish processing of the surfaces is often necessary. It is quite challenging to meet these standards with conventional polishing processes. The potential to modify the beam size for attaining the aspheric features makes FJP a perfect method for micro-lens molds and mold arrays that require final finishing.

Fig. 1.8 Polishing of micro-mold (Source: Beaucamp *et al.* [5])

Polishing of Micro-channels

Microgrooves and channels can be polished using FJP using a tiny nozzle with a dimension of a couple of hundred microns. Matsumura *et al.* [66] state that a final surface polish of 25 nm Ra can clearly demonstrate the effective removal of milling marks and underlying crack damage (Fig. 1.9) within a micro-channel.

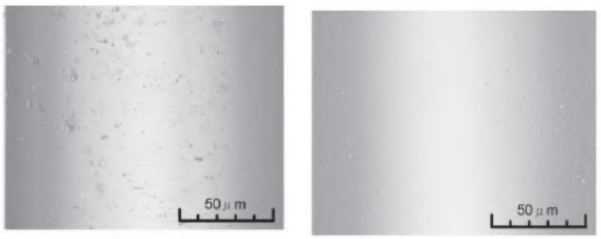

(a) (b)

Fig. 1.9 Micro-milled channel (a) before polishing (b) after polishing (source: Matsumura *et al.* [66])

Smoothing of Micro-cusps

Light diffraction and scattering from the fine cusps left behind by procedures like diamond tuning and micro-grinding can result in a highly noticeable decline in optical performance. Such micro-cusps can take a long time to remove using regular polishing tools. Beaucamp & Namba [6] demonstrated that the FJP technique has an excellent propensity to smoothen regular structures on such pre-machined surfaces.

Formation of Functional Surfaces

The material removal rate of the FJP process is steady and predictable under controlled conditions. It thus can be used to create functional surfaces with repeatable structures and patterns that are useful in controlled surface lubrication, microfluidics, and micro-electromechanical systems (MEMS). It was demonstrated (Fig. 1.10) by Cao *et al.* [14] that it is technologically possible to achieve a few nanometers of depth resolution and a few dozen nanometers of accuracy.

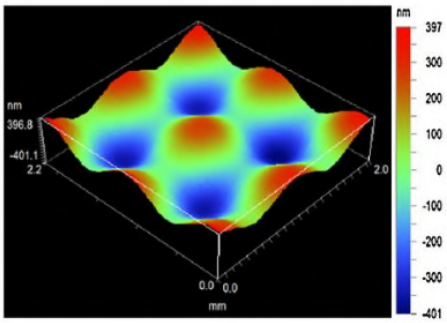

Fig. 1.10 Functional pattern generated on BK7 Glass Cao *et al.* [14]

All the above applications can largely benefit from any improvisation that overcomes the limitations of FJP, as mentioned in the previous subsection. In this regard, the current work proposes a novel technique of acoustophoretic-assisted FJP. Before proceeding into the details of this technique, we introduce acoustophoresis and related phenomena in the next section.

1.3 Acoustophoresis

Acoustophoresis is the process of manipulating particles within a fluid stream by means of sound waves. When a resonant acoustic excitation creates an acoustic standing wave, a particle inside it experiences time-averaged non-trivial forces. Depending on the properties of the fluid medium and the particles, i.e., their densities and compressibilities, the forces drive the particles toward the pressure or anti- nodes within the standing wave. These so-called "radiation" forces can be classified into two: primary radiation forces, which act directly on particles, and secondary radiation forces, which involve interactions between particles.

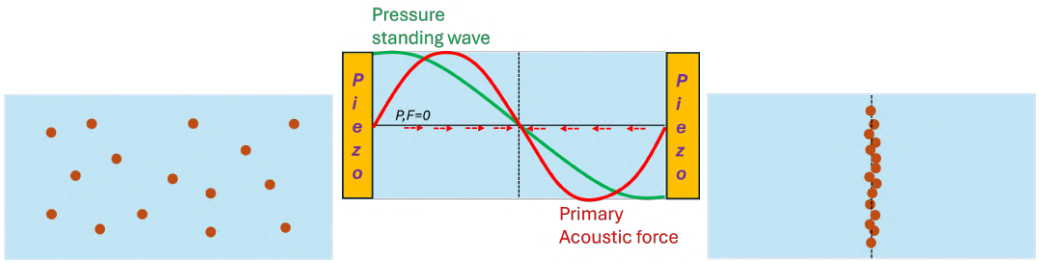

(a) (b) (c)

Fig. 1.11 Schematic of particle aggregation sequence (a)Initial particle distribution (b)$\lambda/2$ wavelength pressure resonance (c) final particle distribution

1.3.1 Primary Radiation Force

Since the acoustic impedance of the particle material and carrier fluid are typically different, an unbalanced acoustic radiation pressure is set up on the particle's surface within a standing wave. This unbalanced pressure results in a time-averaged force on the particles called the 'Primary Radiation Force' or simply the 'Acoustic Radiation Force' (Fig. 1.11).

1.3.2 Secondary Radiation Force

The secondary radiation force becomes relevant when multiple particles are present in the fluid media. The total inbound field on a particle is then the sum of primary and scattered fields emitted from the other particles. This inter-particle interaction gives rise to what is known as the 'Secondary Radiation Force'.

1.3.3 Acoustic Streaming

While acoustic radiation forces are a significant factor in particle manipulation, acoustic streaming (which originates from the fluid's viscous attenuation, thus causing a net displacement of the suspended particles) is another significant phenomenon used in the acoustic concentration/separation process. Time-independent flow patterns brought on by a sound field in a fluid define this phenomenon. It can be categorized into three varieties, each with an inherent length scale. The term 'Schlichting streaming' refers to streaming with vortices substantially smaller than the acoustic wavelength that transpires in the viscous boundary layer near a surface (Schlichting [81]). The origin of 'Rayleigh streaming' is due to the losses in boundary layers that create streaming vortices beyond the layer (Strutt [87]). The fluid's absorption causes 'Eckart streaming', which is a large-scale phenomenon. Eckart

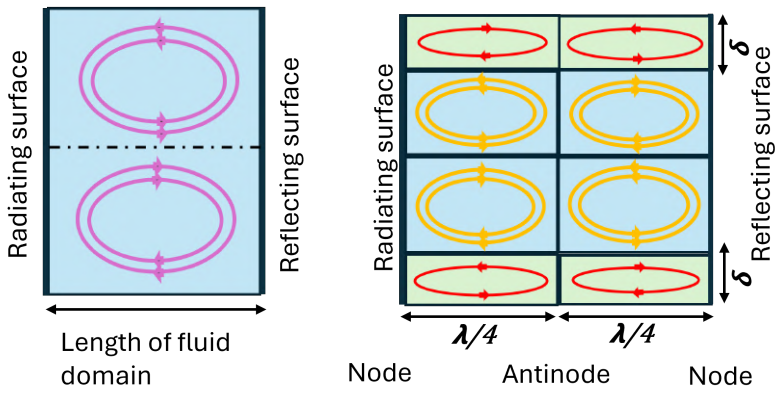

(a) (b)

Fig. 1.12 Schematic of (a) Eckart streaming (pink line) (b) Rayleigh streaming (orange line) and Schlichting streaming (red line)

streaming usually provides a flow in the direction in which the sound propagates, as opposed to a vortical pattern (Eckart [22]). Counter-flows, however, are inevitable in a closed system since the fluid cannot cross the boundary.

1.4 Thesis Overview

The current work presents a Proof-of-Concept study of a novel acoustophoresis-assisted Fluid Jet Polishing technique. Here, the abrasive particles are manipulated within the jet using standing acoustic waves that are formed perpendicular to the flow direction. The present work analyses this proposed technique through detailed numerical simulation involving a combination of Eulerian & Lagrangian approaches. The process of surface erosion has been modelled using empirical correlations that use particle trajectory information of the Lagrangian DPM model to arrive at the spatial erosion profile. The present effort has been primarily focused on two different cross-sections of the jet, viz. circular and square. While the circular cross-section provides the ability to perform precise annular erosion, the square cross-section is shown to manifest U-shaped erosion profiles for specific operating conditions that have been arrived at using detailed parametric analysis.

1.5 Thesis Outline

The current thesis proposes the novel acoustophoresis-assisted FJP process using six chapters, including the current 'Introduction' chapter. In Chapter 2, we begin with the literature survey and understanding of the state-of-the-art with respect to the Fluid Jet Polishing process. This is followed by describing the mechanisms and factors affecting the erosion process. A detailed note about the various theoretical and empirical erosion models present in the literature is provided. In addition to this, existing particle manipulation methods utilizing electrical, optical, magnetic, and acoustic fields are also briefly reviewed. Amongst these, a detailed account is given about different acoustophoretic applications.

In Chapter 3, the acoustic radiation force acting on a small spherical particle is developed using general perturbation theory. Specifically, the acoustic radiation force equations are derived for cylindrical and rectangular domains using the procedure outlined by Gor'kov [32]. This is followed by the details on the numerical methods used to solve the conservation equations of mass and momentum of fluid flow. The force balance equations that yield the particle trajectories are also discussed. Finally, a validation case is outlined which shows the applicability of a modified generalized erosion model.

Chapters 4 and 5 deal with the numerical modelling of acoustophoretic intervention in FJP with circular and square cross-sectioned nozzles, respectively. The most high-profile results obtained are the precise annular ring erosion pattern in Chapter 4 and the point erosion pattern in Chapter 5. The erosion depth profiles under different acoustic excitation frequencies are presented and are supplemented by particle impact position, angle, and velocity plots.

The thesis ends with Chapter 6, which provides the summary and conclusions of the current work along with the scope for future extension.

Chapter 2

Literature Review

In the available literature, there have been many investigations in the area of slurry jet impingement and allied erosion processes. An effort has been made to provide a holistic picture of the relevant research in the following sections.

2.1 State of the art

Several parametric analyses of experimental fluid jet polishing have been published in scientific texts. Fähnle *et al.* [23] presented Fluid Jet Polishing (FJP) as an innovative method of shaping and polishing wherein a pressurized slurry of a carrier fluid and abrasive particles is guided through a nozzle and made to interact with a workpiece to eliminate material from the substrate. The concentration, size & kind of erodent, fluid, pressure of the slurry, run time, target material, geometry, and the nozzle's placement with respect to the workpiece surface, all impact the removal rate and polishing process. Turenne *et al.* [90] experimentally evaluated the effect of solid particle concentration in a sand-water slurry direct jet impingement setup (see Fig.(2.1)). They discovered the power law dependence on the particle concentration, wherein with a one-third exponent, the models predict the fall of the erosion rate. Li *et al.* [59] described experimental measurements of liquid-solid particle jet impingement flow. Copper, Aluminium & Mild Steel were the target materials used, and the slurry flows used were - coal particles carried by kerosene, Alumina particles carried by water and Silicon-Carbide particles carried by water. Based on numerical analysis and an impingement angle test set at 90^o, Sugiyama *et al.* [88] approximately estimated the volume reduction caused by a single particle impact. The validity of the estimation for lower impingement angles was then discussed by comparing it to the actual test results.

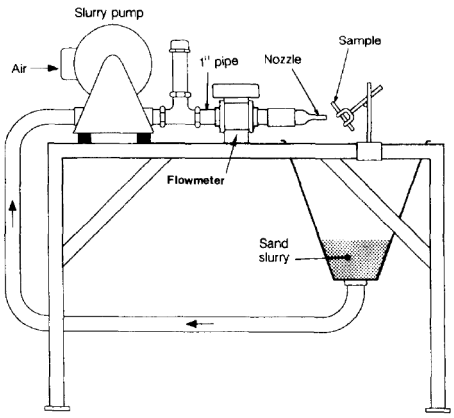

Fig. 2.1 Experimental apparatus used for slurry erosion tests by Turenne *et al.* [90]

The dependency of several significant FJP process parameters, including processing duration, erodent concentration, erodent diameter, particle velocity, and the impact of nozzle translation, on the material removal rate was reported by Booij *et al.* [11]. Fang *et al.* [24] examined how the properties of abrasive particles, the workpiece, and additional process variables like operating pressure and incident angle affected material removal and surface roughness. According to their experimental findings, the volumetric removal rate of glass is inversely related to the square of its Knoop hardness (H_k) and roughly proportional to the square root of its Young's modulus (E).

2.1.1 Improvisations in FJP

Over the course of the last couple of decades, scholars have tried to come up with advancements to overcome some of the drawbacks of the conventional FJP process. One of the major weaknesses of the FJP process includes the low material removal rate due to poor particle utilization as a large fraction of particles are simply carried away by the flow without striking the surface. Consequently, it takes longer to polish surfaces as compared to other methods. It has been widely documented that raising the slurry concentration and fluid pressure can accelerate the rate of material removal. However, both these options come with their associated issues. While the higher fluid pressure results in a poor surface finish, the high slurry concentration makes the jet unstable and leads to the slurry system's blockage.

Peng *et al.* [77] showed via theoretical analysis and experimental exploration that the abrasive particles' size has a significant impact on the rate of material removal and surface quality after processing. They posit that whereas material expulsion in the elastic mode has a significantly lesser removal rate and a more streamlined surface for smaller particles, material removal in the plastic mode has a greater removal rate and poorer surface texture

for larger-sized particles. As an alternative, Wang *et al.* [91] suggested the use of multiple jets to enhance the material removal rate. They proved through experiments and simulations that multi-jet polishing can remove material at a far greater pace than single-jet polishing. Moreover, it has higher polishing surface coverage efficiency due to the larger size of the polishing tool. However, there are a few issues with this technique including manufacturing of multi-jet tools, interference of adjacent jets, etc.It was demonstrated experimentally by Messelink *et al.* [69] that a well-controlled gas injection into the slurry stream prior to it reaching the nozzle can raise the footprint depth of the FJP process. Yu *et al.* [97] proposed an air-driven FJP process system (Fig.(2.2)(a)) in which the nozzle used the venturi method to draw the suspension into an air stream. A Gaussian-like removal form without oblique incidence is made possible by the compressed air, which also increases the kinetic energy of each abrasive. In both cases, mixing slurry with air bubbles remarkably increased the material removal rate. However, the bubbles were observed to break up the jet plume, which resulted in the loss of process stability and an inferior surface finish. Also, there is a lack of control over the size and number of micro-bubbles injected into the stream. As a remedy, Beaucamp *et al.* [5] proposed an ultrasonic cavitation-assisted FJP (Fig.(2.2)(b)) wherein the size and number of micro-bubbles could be controlled through the frequency and intensity of the ultrasound generator. They claimed that the material removal rate could be increased up to 380% and could even improve the surface finish when compared to normal FJP.

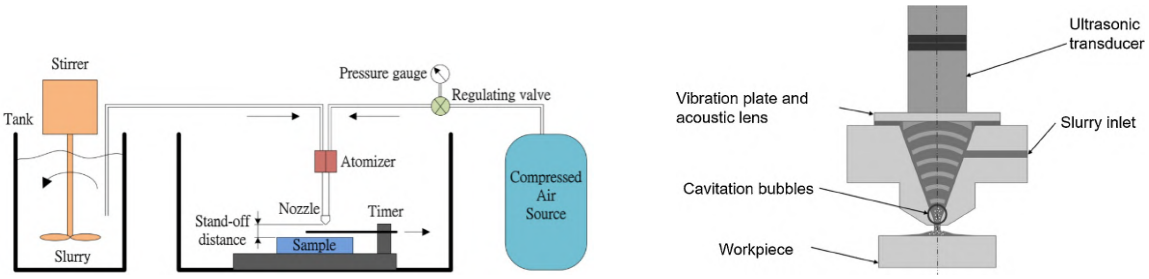

(a) (b)

Fig. 2.2 (a)Schematic of the air-driving FJP by Yu *et al.* [97] (b)Principle of ultrasonic cavitation assisted FJP by Beaucamp *et al.* [5]

Foldyna *et al.* [30] showed that ultrasonic excitation can also make the jet pulsatile, which helps enhance the impact force of the particles due to water hammer effect.When cutting different materials in a lab setting, ultrasonically modulated jets outperformed continuous jets in terms of performance. The nozzle excitation can also enhance the mixing of abrasive particles to boost the material removal rate as established by Hou *et al.* [45]. According to the polishing experiment results, adding ultrasonic vibration boosts the erosion depth,

which indicates that ultrasonic vibration significantly improved the micro-abrasive water-jet's machining capability. Alternatively, Qi *et al.* [79] showed that one can also vibrate the target surface using an ultrasonic agent to alter the particle impact positions. Through CFD simulations, they were able to notice a periodic change in the stagnation zone's static pressure, which leads to dynamic impacts of abrasives on the workpiece. These impacts not only raise the average erosion rate but also help to distribute the erosion area uniformly.

Nevertheless, all the above modifications still suffer from the limitation of inhomogeneous erosion of the target surface. Also, owing to the turbulent nature of the jet, the nozzle wall undergoes marked erosion. Consequently, there is a reduction in nozzle life and a lack of repeatability in the machining process.

2.2 Solid particle erosion mechanisms

Solid particle erosion is a process where the surface of a material is gradually worn away or degraded due to sustained impact of solid particles. This typically occurs when particles entrained in a fluid (air, water or any working fluid) impinge on the surface of a material. The impact of these particles causes localized stresses on the surface, leading to material removal through mechanisms such as abrasion, cutting, plowing, or fracture.
In the field of erosion research, the target materials are typically classified into ductile and brittle. These phrases describe the extremes of a spectrum on how a material reacts to loads and pressures from the outside. Brittle materials have a tendency to yield suddenly with slight deformation, while ductile ones deform notably before breaking.

2.2.1 Erosion mechanism in Ductile material

The ability of a material to be stretched, tugged, or twisted into thin wires or threads without breaking is known as ductility. It measures the amount of elongation or deformation the material can withstand under stress before completely failing. Metals are typically linked to ductility. A number of mechanisms have been proposed by several researchers for erosion in ductile materials. Finnie [26] put forward a micro-cutting framework in which he considered abrasive particles as cutting implements and tiny craters created as a result of particle impact at low grazing angles. The chip created by the earlier hit is eliminated by the following particles. This process works well, but, at low impact angles; at near-to-typical impact degrees, a significant inaccuracy manifests itself.

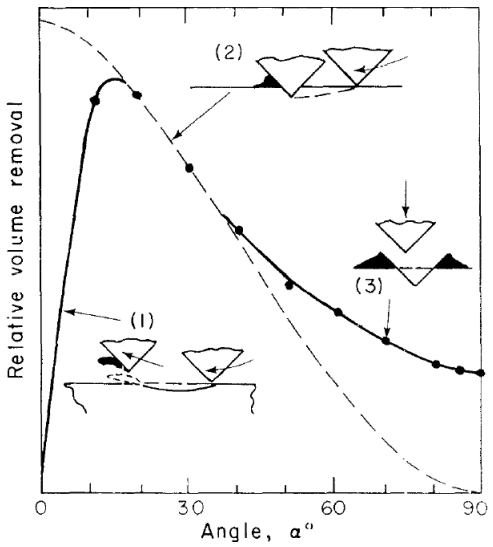

Fig. 2.3 Expected Variation of Volume Removal with Angle (Curves 1, 2) and Experimental Values (Curve 3) Normalized with Maximum Erosion (Finnie [28])

Later, Bitter [8] outlined solid particle erosion as a phenomenon marrying deformation and cutting which could explain the erosion damage at high impact angles. In his study, Hutchings [47] investigated a low cycle fatigue solid particle erosion theory for impact angles of 90^o. He looked at the connection between the erosion phenomenon and the rise in surface material plastic strain, hypothesizing that wear debris is eliminated at a critical plastic strain. A macroscopic solid particle erosion mechanism was postulated by Bellman Jr & Levy [7], who also believed that the loss of surface material might be explained as a hybrid process including extrusion and forging. During the process of solid particle erosion, particles striking the material surface form shallow craters or platelet-like pieces, which are then knocked out by the successive impact particles.

2.2.2 Erosion mechanism in Brittle material

A mechanical feature known as brittleness characterizes a material's propensity to fracture, shatter, snap, or crack under stress with little or no plastic deformation. Materials that are brittle do not exhibit any discernible yielding or elongation prior to breakdown. Brittle materials show abrupt and frequently catastrophic failure with little to no warning, in contrast to ductile materials, which can deform extensively before breaking. Materials that are brittle include glass, ceramics, and several varieties of cast iron.

It is commonly accepted that erosion in brittle materials is a result of crack formation upon impact of the abrasive particles as shown in Fig.(2.4). When a particle comes into contact with a brittle material, lateral and radial cracks form, and the lateral ones are responsible for

the majority of material removal. As a result of the solid particles' constant collision, the fissures progressively widen and allow surface material to be removed by breaking it up into tiny fragments.

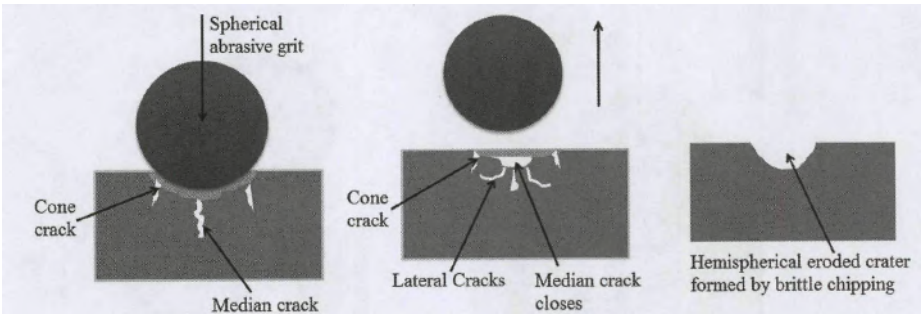

Fig. 2.4 Erosion mechanism in brittle material by Sooraj & Radhakrishnan [86] (a)development of cone crack and median cracks (b) Lateral cracks (c) eroded crater formed by impact

2.2.3 Factors affecting solid particle erosion

Solid particle erosion is influenced by various elements such as the properties of the abrasive particle, the target material, and the operating conditions. It is vital to ascertain these parameters to predict accurately the material removal due to particle erosion. The major factors that have been identified are

1. ***Particle Impact Speed :***
   Impact velocity is the velocity with which the abrasives hit the workpiece. According to the majority of the published works in erosion modeling, the erosion rate (ER) is given by a power law expression

$$ER \propto V_p^n \tag{2.1}$$

   Finnie [26] in his original theoretical work on erosion modeling set the exponent to 2 as he attributed this to the particle's kinetic energy before impact. Later in 1995, he argued that the velocity exponent is greater than 2 if particle rotation is taken into account. Tilly [89] suggested that there exists secondary erosion caused by particle fragmentation and that a velocity exponent greater than 2 was required to model the combination of primary and secondary erosion. Oka *et al.* [75] concluded that the exponent is a function of the hardness of the erosion material based on a large number of erosion tests. Most experimental studies suggest that the velocity exponent value is between 2.0 and 3.0.

2. ***Particle Impact Angle :***
   It has been well established that particle-impinging angle plays an important role in erosion wear. For ductile materials, the cutting action at shallow impact angles is more efficient than at larger angles. The erosion rate rises from normal impact to a maximum at a shallow impact angle and then drops to zero at glancing impact. For brittle materials, the erosion rate is maximum for normal impacts as the dominant erosion mechanism there is the repeated plastic deformation.

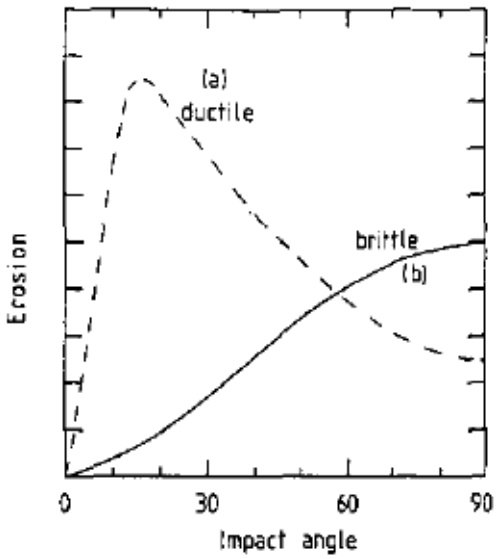

Fig. 2.5 Influence of impact angle on erosion of ductile and brittle materials (Hutchings [48])

3. ***Particle properties :***
   The main particle properties that heavily guide the erosion rate are size, shape and hardness. Increasing particle size causes a sharp increase in erosion rate, as reported by Liebhard & Levy [60], which links this result to an increase in kinetic energy. The mass loss ratio, however, plateaued above a certain size, and this behavior was attributed to the interaction between the incoming and rebounding particles as well as the size and quantity of particles striking the surface as can be seen in Fig.(2.6).

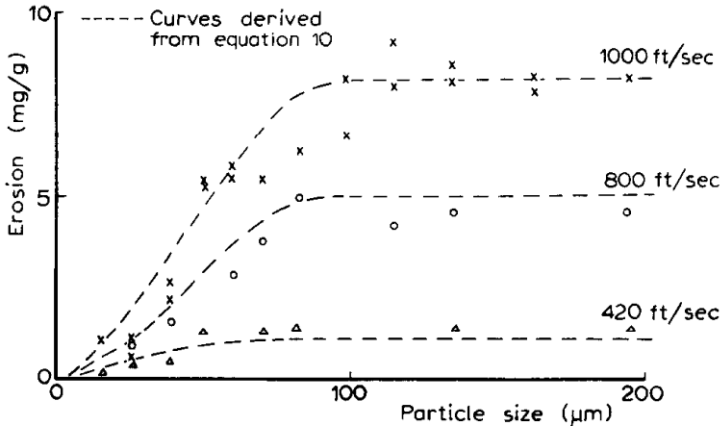

Fig. 2.6 Influence of particle size on erosion at different velocities (Tilly [89])

The effect of particle form on erosion was tested by Levy & Chik [58] on AISI 1020 steel with spherical and angular particles (Fig.(2.7)). They found that angular particles were capable of removing more mass as they formed sharp and deep craters unlike spherical particles which formed shallow and rounded craters. Furthermore, the Erosion/Corrosion Research Centre (E/CRC) at the University of Tulsa carried out extensive erosion experiments and defined a sharpness factor F_s. $F_s = 1, 0.5, 0.2$ for sharp, semi-rounded, and fully-rounded particles respectively.

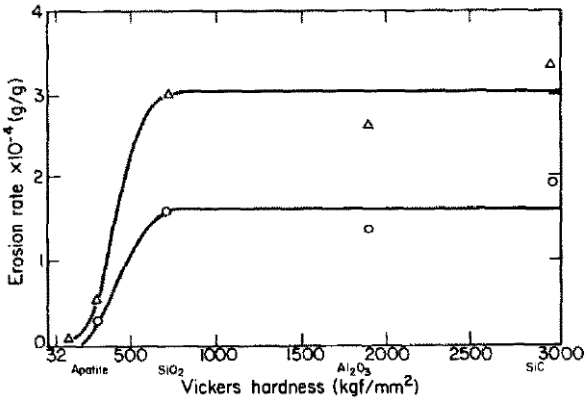

Fig. 2.7 Erosion rate of AISI steel 1020 by five erodent (Levy & Chik [58])

Particle hardness and erosion rate exhibit a power law connection, with an exponent of 0.89, as reported by Khanouki [52].

4. ***Properties of target Material :***
   Vickers hardness H_V is inversely associated with the volume loss of work-annealed material (Fig.(2.8)), according to Finnie [27]. In their investigation on the connection

between erosion damage and surface hardness, Oka *et al.* [74] found that, for all test materials, the recessed area increases as Vickers hardness decreases. Levy [57] conducted a set of erosion tests on a bunch of Ni and Co based alloys and various Vickers hardness and observed that softer material resulted in lower mass.

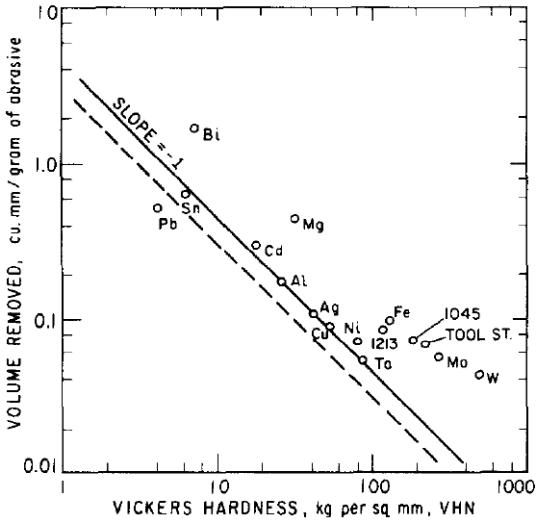

Fig. 2.8 Volume Removed (mm^3/g abrasive) versus Vickers Hardness (Finnie [27])

5. ***Particle Concentration :***
   Particle-particle interaction is a multifaceted phenomenon that requires consideration when the concentration of abrasive particles rises over that of a dilute mixture. In gas-solid erosion tests, KLEIS *et al.* [54] and Anand *et al.* [1] discovered that erosion rate falls with increasing particle flux. This discovery can be explained by the fact that particles that bounce off one another form a shield close to the target surface, preventing incoming particles from entering. The erosion ratio of Al samples under a slurry jet is found to decrease in accordance with the power law of the sand concentration, as reported by Turenne *et al.* [90]. This trend has been reported by several researchers since then.

6. ***Fluid flow dynamics :***
   It is integral to understand the flow field surrounding the abrasive particles and its effect on the erosion rate. Momentum exchange between the fluid and the abrasive particles determines the particle trajectory. Increasing the density and viscosity of the carrier fluid tends to increase the drag force acting on a particle, making the momentum exchange more efficient. The Stokes number (St), which is defined as the ratio of a particle's characteristic time scale to the flow's characteristic time scale, can be used to

represent the implication of fluid density and viscosity on particle pathways.

$$St = \frac{\tau_p U}{D} \tag{2.2}$$

where

$$\tau_p = \frac{\rho_p d_p^2}{18\mu_f}$$

is the characteristic time scale of the particle, U is the flow velocity and D is the characteristic dimension of the flow geometry (typically diameter).

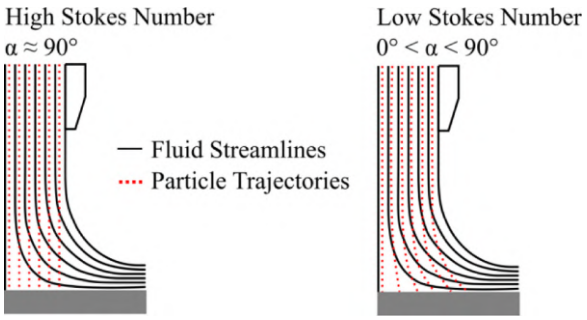

Fig. 2.9 Fluid streamlines and particle trajectories for high and low *St* jet impingement (Frosell *et al.* [31])

In gas-solid flows (high Stokes number), the particle inertia dominates and the effect of the flow field on the particle is negligible. Thus, solid particles impact the surface with an angle almost the same as the jet impingement angle. In liquid-solid flows (low Stokes number), the particles follow the flow streamlines more faithfully due to higher drag. Thus, in this regime, the particles strike the surface at a wide range of angles between 0^o to 90^o. This behavior is illustrated in the Fig(2.9). Mansouri *et al.* [64] conducted erosion experiments with air-sand and water-sand impingement jets. Their results show that high Stokes number flows(gas-solid) produce a U-shaped erosion profile whereas low Stokes number flows(water-solid) produce a W-shaped erosion profile.

2.3 Solid Particle Erosion Models

Several investigators have strived to relate solid particle erosion to several variables such as particle impact conditions and material properties in forms that can be called Erosion Models/equations. One of the earliest reported erosion equations was by Finnie (1960) in

which he obtained an expression for estimating the volume of material W removed by erodent particles.

$$W = \begin{cases} C\frac{MV^2}{\Psi pK}[sin(2\alpha) - \frac{6}{K}sin^2(\alpha)] & tan(\alpha) <= \frac{K}{6} \\ C\frac{MV^2}{\Psi pK}[\frac{Kcos^2(\alpha)}{6}] & tan(\alpha) > \frac{K}{6} \end{cases} \tag{2.3}$$

where K, Ψ, V, M, p are the ratio of vertical to horizontal frictional force, the depth of contact divided by the depth of the cut, the particle impact velocity, the total mass of erodents, and the eroding surface flow stress, respectively. Finnie suggested the other parameter values to be K=2, Ψ=1, and C=0.5. This model accurately predicted erosion at low-impact angles due to the cutting mechanism but proved short of the mark at high-impact angles as it didn't take into account the plastic deformation mechanism. Bitter [8] tried to improve on the previous model by including a plastic deformation mechanism which was expressed as

$$E_d = \frac{1}{2}\frac{M(V_p sin\theta - V_n)^2}{\varepsilon_b} \tag{2.4}$$

where E_d is the volumetric loss due to the deformation method. The energy needed to remove a unit volume of material owing to deformation is ε_b. The following expression was recommended for cutting erosion

$$\begin{cases} E_{c1} = \frac{2MV_p(V_p sin\theta - V_n)^2}{(V_p sin\theta)^{\frac{1}{2}}}(V_p cos\theta - \frac{C(V_p sin\theta - V_n)^2}{(V_p sin\theta)^{\frac{1}{2}}}\phi) & \theta <= \theta_{p0} \\ E_{c2} = \frac{\frac{1}{2}[V_p^2 cos^2\theta - K_1(V_p sin\theta - V_n)^{\frac{3}{2}}]}{\phi} & \theta > \theta_{p0} \end{cases} \tag{2.5}$$

where the energy needed to remove a unit of volume from the workpiece is ϕ, θ_{p0} is the impact angle at which the particle departs the surface and the horizontal velocity component becomes zero. The total erosion E_t can be written as a summation of the deformation and cutting mechanism

$$E_t = \begin{cases} E_d + E_{c1} & \theta <= \theta_{p0} \\ E_d + E_{c2} & \theta > \theta_{p0} \end{cases} \tag{2.6}$$

Neilson & Gilchrist [72] further streamlined Bitter's model as

$$E_t = \begin{cases} \frac{MV_p^2(cos\theta sin(n\theta))}{2\phi} + \frac{M(V_p sin\theta - V_n)^2}{2\varepsilon_b} & \theta <= \theta_{p0} \\ \frac{MV_p^2 cos^2\theta}{2\phi} + \frac{M(V_p sin\theta - V_n)^2}{2\varepsilon_b} & \theta > \theta_{p0} \end{cases} \tag{2.7}$$

Apart from these theoretical erosion equations, several attempts have been made to model erosion based on experimental results most of which follow a general form given by

$$ER = KV_p^n f(\theta) \tag{2.8}$$

where ER stands for erosion ratio, which is the mass of abrasive particles divided by the ratio of material loss, K is a constant depending on target material properties, and f(θ) is an impact angle function. McLaury [67] put forward an erosion equation for Carbon Steel and Aluminium in which the angle function was

$$f(\theta) = \begin{cases} a\theta^2 + b\theta & \theta <= \alpha \\ xcos^2\theta sin(w\theta) + ysin^2\theta + z & \theta > \alpha \end{cases} \tag{2.9}$$

where a,b,x,y,z are empirical constants given in the table below.

Material	**Carbon Steel**	**Aluminum**
A	1559 $BH^{-0.59}$	2.388e -7
α	15 degrees	10 degrees
a	-3.84e-8	-34.79
b	2.27e-8	12.3
w	1.0	5.205
x	3.147e-9	0.147
y	3.609e-10	-0.745
z	2.532	1.0

Table 2.1 Empirical constants in equation (2.9)

Haugen *et al.* [36] at Det Norske Veritas (DNV) in Norway came up with an erosion model after conducting numerous experimental tests with different materials and presented a polynomial angle function

$$f(\theta) = \sum_{i=1}^{8} (-1)^{i+1} A_i (\frac{\theta\pi}{180})^i \tag{2.10}$$

where the A_is are given in the following table

A_1	A_2	A_3	A_4	A_5	A_6	A_7	A_8
9.37	42.295	110.864	175.804	170.137	98.298	31.211	4.170

Table 2.2 Constants in equation (2.10)

Zhang *et al.* [98] at E/CRC based on a series of tests on Inconel 718 material suggested an

erosion equation in the following form

$$ER = C(BH)^{-0.59} F_s V_p^n f(\theta) \tag{2.11}$$

$$f(\theta) = \sum_{i=1}^{5} A_i \theta^i \tag{2.12}$$

where BH is the Brinell hardness of the target material, and F_s is the particle shape factor. The empirical constants were set to be n=2.41 and C=2.17e-7. The values of A_i are given in the following table

A_1	A_2	A_3	A_4	A_5
5.4	-10.11	10.93	-6.33	1.42

Table 2.3 Values of A_i in equation (1.12)

Oka *et al.* [75] proposed an empirical erosion equation based on extensive erosion tests and several important factors such as particle impact speed and angle, particle and target material properties, relaxation of target material, and particle size. The so-called Oka model is

$$\left.\begin{aligned} &ER = g(\theta) E_{90} \\ &g(\theta) = (sin\theta)_1^n (1 + H_v(1 - sin\theta))^{n_2} \\ &E_{90} = K(H_v)^{k_1} (\tfrac{V_p}{V'})^{k_2} (\tfrac{D_p}{D'})^{k_3} \\ &n_1 = s_1 (H_v)^{q1}, \quad n_2 = s_2 (H_v)^{q2}, \quad k_2 = 2.3 (H_v)^{0.038} \end{aligned}\right\} \tag{2.13}$$

where E_{90}, $g(\theta)$, θ, H_v, V_p, $V^{'}$, D_p and $D^{'}$ are the erosion rate at orthogonal impact, the erosion rate at any impact angle, the Vickers hardness, the particle impact velocity and the reference impact velocity, the particle diameter and the reference diameter, respectively.

2.4 Particle Manipulation Techniques

Particle manipulation techniques of suspended micro-particles (e.g. micrometer-sized solid objects, biological cells, and immiscible droplets) are essential in various fields such as material science, biotechnology, and micro-engineering. These cover, among other things, sorting, focus, separation, rotation, automatization, and cell handling applications. Manipulation techniques can typically be categorized into three categories viz. classic manipulation techniques, manipulation using external fields, and manipulation using hydrodynamic mechanisms.

Large-scale applications are usually best served by traditional techniques like sedimentation, centrifugation, and filtration, which depend on mechanical contact or properties that are dependent on gravity. Sedimentation has the plus points of being inexpensive and easy to set up but is defeated if drag forces or Brownian motion dominate over the buoyancy forces for example in a turbulent suspending medium. Centrifugation uses centrifugal force to improve sedimentation efficiency by a few orders of magnitude but has to deal with the presence of moving parts.

Various hydrodynamic mechanisms have been applied to the manipulation of particles. These techniques can be classified into two groups: the vortical flow methods and the cross-stream migration-based methods. The lift force that particles encounter in a shear flow is referred to as the movement of suspended particles across the stream in a constrained flow. The force is contingent on the parameters of the particle and carrier fluid in addition to the flow field, and it is perpendicular to the flow direction. This comprises dean flow, deformability-selective cell separation, viscoelastic focusing, and inertial effects. (Karimi *et al.* [51]). Microfluidic channels with focusing, pinching, and extraction zones make use of inertial effects. This permits, among other things, size fractionation, or the concentration of particles in a particular area of the channel. Particles in a shear-thinning liquid flow have been moved toward the walls via viscoelastic focusing, and in an elastic fluid flow, they have been moved toward the center line. Dean flow generates symmetrical vortices by taking advantage of the discrepancy in velocities in curved channels. Using short-range forces, vorticity can be utilized to gather particles from various directions and capture them. As a result, particles can be sorted, released, and trapped. Methods to produce vortices include geometrical channel modifications, electroosmosis, dielectrophoresis, and acoustic streaming. Applications include using a stagnation area (Kreft *et al.* [56]) or AC electro-osmosis (Du *et al.* [21]) to capture DNA. The techniques can be very useful for detecting and analyzing low-diffusivity substances, like DNA. Vorticity-induced entrapment can improve the Brownian transport to a limited sensor surface.

Different external fields like optical, electric, magnetic, and acoustic can be employed to control manipulate particles at the micro and nano scales non-invasively. A well-known technique of using extremely concentrated light beams to capture and control microparticles is optical tweezers (Clement-Sengewald *et al.* [16]). The forces that push the particles along the beam—repulsive scattering or radiation pressure forces and attractive optical gradient forces—are in balance when particles are confined in the beam. Among other things, optical tweezers have been used to capture metal particles, dielectric spheres, and cells. They are

perfect for applying forces to biological samples and observing how they react because they provide extremely precise measurements (one such example is shown in Fig.(2.10)). On the downside, optical tweezers require complicated, costly, and difficult-to-miniaturize setups that run the risk of heating up the sample and damaging it.

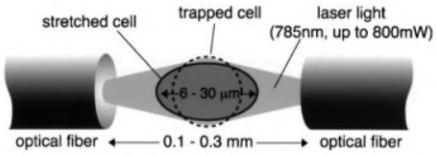

Fig. 2.10 Stretching of cell trapped in an optical stretcher by Guck *et al.* [34]

Dielectrophoresis (DEP) is a process where a suspended particle's dipole moment is induced by a gradient in the electrical field (Pohl *et al.* [78],Schnelle *et al.* [82]). When a particle has a higher polarization than the carrier medium, it experiences attractive forces toward increased field density, known as positive DEP. On the other hand, when a particle has lower polarization, it experiences repulsive forces, known as negative DEP (see Fig.(2.11)). DEP works well for size fractionation because the force increases as the particle's volume decreases. Relaince on medium conductivity, particle polarizability, or current-induced heating, however, are possible disadvantages.

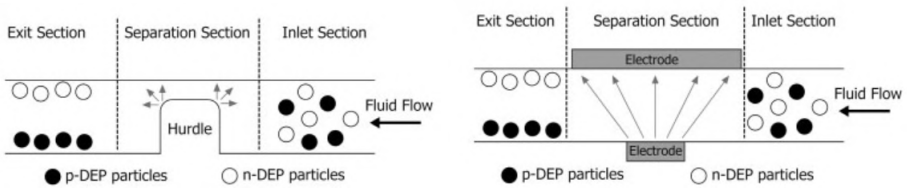

(a) (b)

Fig. 2.11 Schemtaic of DEP based microfluidic devices (a)non-uniform electric field by means of insulating hurdle (b)non-uniform electric field by means of asymmetric electrodes (Çetin & Li [15])

Magnetic forces affect particles in a varying magnetic field. These particles can be ferromagnetic, paramagnetic, or diamagnetic. Typically, super-paramagnetic nanoparticles are used, as they have no magnetic memory (Pamme [76]). Micrometer-sized particles usually exhibit hysteretic magnetization behavior. Paramagnetic particles are attracted to the maximum magnetic field. The advantages include relatively high forces in a short range and the ability to manipulate many particles. However, the force field is typically highly

inhomogeneous.

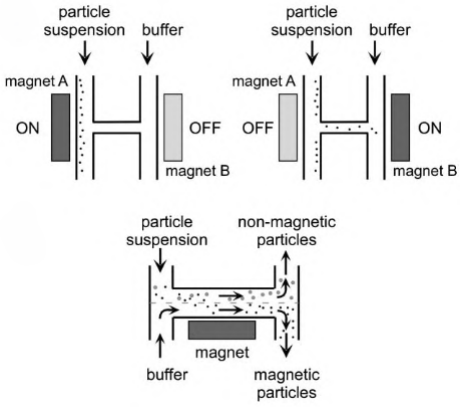

Fig. 2.12 Priciple of H-shaped magnetic separators by Pamme [76]

2.4.1 Acoustophoresis

This particular technique has been presented in greater depth as it is central to the subject matter of this thesis. The process of acoustophoresis, sometimes called acoustic or ultrasonic particle entrapment, uses the forces of acoustic radiation acting on particles within an acoustic field. In a standing wave field, Higher-density and higher-compressibility particles usually gather in the pressure nodes, whereas lower-density and lower-compressibility particles usually collect in the pressure anti-nodes (Muller *et al.* [71],Bruus [13]).

Historical development of Acoustic Radiation Forces

By integrating the entire acoustic pressure field on the body's surface, King [53] calculated the radiation pressure on a hard spherical body freely suspended in an inviscid fluid. Yosioka & Kawasima [96] extended the earlier research to compressible spheres, finding good agreement between theory and experiment. They reported the equation for mean radiation force in a plane standing wave as

$$< F_s(x) >= 4\pi\kappa a^3 < \overline{E_s} > K_s(\lambda,\sigma) sin(2\kappa x) \tag{2.14}$$

where a, κ, K_s and $< \overline{E_s} >$ are particle radius, wavenumber, acoustic contrast factor and energy density respectively. The assumption taken in this computation is that the particle radius a is much smaller than the sound wavelength λ. Crum [19] examined the acoustic radiation force in a stationary wave on fluid droplets and found that the total force can be

described as the addition of the force that would be achieved if the droplet were a hard sphere and the force that would come from its compressibility.

A force between two spheres that are closely spaced in an acoustic field was expressed by König [55].Subsequently, Bjerknes *et al.* [9] computed the repulsive and attractive forces between cyclically fluctuating spheres without taking the principal sound field into account. Thus the acoustic interaction force is often referred to as $'Bjerknes'$ force. Using the assumption that the particle radius a and the inter-particle distance d are significantly lower than the wavelength, Weiser *et al.* [94] computed the interaction force between two equivalent compressible spheres in a plane stationary wave as

$$< F_i(x) >= 4\pi a^6 \{ \frac{(\rho_0 - \rho)^2 (3cos^2(\theta) - 1)}{6\rho d^4} v^2(x) - \frac{\omega^2 \rho (\beta_0 - \beta)^2}{9d^2} p^2(x) \} \tag{2.15}$$

where β_0 and β are respectively the carrier fluid's and the particles' compressibilities; θ is the angle between the centreline of the particles and the transmission direction of the incoming sound wave; the velocity and pressure of the undisturbed incoming field at the particle's position are denoted by $v(x)$ & $p(x)$. The particle's direction with relation to the incoming field determines the first term on the right-hand side of equation (2.15). If the particle orientation matches the direction in which sound travels ($\theta = 0$), The initial term indicates a contribution of repelling force. Attractive force contribution arises when the particle centerline is aligned orthogonal to the wave direction. In the formula (2.15), the second term on the right-hand side symbolizes an attracting force, which is independent of particle orientation. The interaction force in a plane stationary wave will lead the particles to group together in the nodal or anti-nodal planes of the sound field.

The acoustophoresis approach avoids some of the disadvantages of the other methods while offering some special benefits of its own. With periodic force fields, it enables the synchronous and simultaneous manipulation of many particles without physical contact. The pressure field is created through combining a solid surface's vibration to the liquid, usually using a piezoelectric transducer operating at frequencies ranging from upper kHz to lower MHz. A standing pressure field with a wavelength usually much greater than the size of the particles is formed when an acoustic wave reflects at the boundaries of an enclosed volume (such a closed cavity or droplet) because of the difference in acoustic impedance. In this scenario, the periodic nature of the field can be used to trap all the suspended particles in the liquid at various locations simultaneously. It can be used on large-scale systems as well as microfluidic ones because it is chemically inert and non-destructive physically. (Hawkes *et al.* [38], Oberti *et al.* [73]). Due to its high cell viability, acoustophoresis can control cells for several hours or days to come. Particles with optical, electrical, or magnetic properties can

all be treated with the same approach. Combining the technique with additional techniques is possible (Ravula *et al.* [80]).

Cell Viability

A large number of documented applications for ultrasonic-wave (USW) particle manipulation are centered around biological cells. As a result, the subject of cell viability becomes crucial. With the primary benefit of eliminating high-speed rotational motion, Doblhoff-Dier *et al.* [20] demonstrated how their new sonic double chamber improved scalability and might be applied to safeguard biomass in the fermentor or as a replacement for centrifugation. Böhm *et al.* [10] studied the exposure of *Petunia hybrida* cell suspensions to two different types of ultrasonic field. They found that standing wave cells suffer far less damage than those in a propagating wave because the cells in a propagating wave likely to stay evenly distributed in the suspending fluid and are, therefore, subjected to sonic pressure and displacement amplitudes that do not disappear on a time average. According to the experimental data, there are no direct or delayed harmful impacts on cells in a microfluidic system that are dealt with and confined by USWs. Hultström *et al.* [46] measured the multiplication rate of anchored cells as a function of ultrasonic inhalation duration in a USW microfluidic chip.

Filtration and Concentration

Filtering particles is an often documented application of ultrasonic radiation forces, with the goal of either eliminating undesired particles from a fluid medium or concentrating particles before additional examination. Cousins *et al.* [17] demonstrated a technique for separation of blood plasma from whole blood by using USW. At half wavelength radial separations, the cells cluster together. Gravity causes the clusters to enlarge and accumulate sediment as shown in Fig.(2.13). They noted that the clarity attained is a major advancement over the previously documented version.

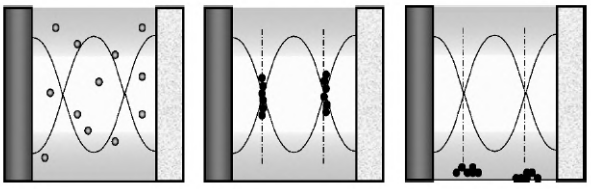

Fig. 2.13 Schematic of enhanced sedimentation by Hill & Harris [42]

An alternate filtering method gathers particles inside a portion of the channel's cross section by use of radiation forces, which are subsequently used to draw the particles out of a concentrated outlet and the residual liquid from a cleared outlet. Large-scale implementation of this can be accomplished by retaining particles on several nodal planes and permitting the flow to diverge across the resonator (Hill & Wood [43]). On the other hand, at the microfluidic scale, there is only one nodal plane since the channel widths are usually smaller than a wavelength. A half-wavelength standing wave is excited within a conduit that is filled with particles from the fluid. Particles are driven to the nodal plane in the chamber's center as they travel through the standing wave. This makes it possible to extract concentrated particles from the flow's center and to extract clarified fluid from the higher, lower, or both outlets, as seen in this example (Hawkes & Coakley [39]).
Utilizing a USW field's radiation effects to alter a porous mesh's filtration properties is an intriguing substitute for the filtration methods previously discussed. The method uses a high-porosity polyester mesh to allow fluid particles to pass through. Since the pore size might exceed the particle size by up to two orders of magnitude, the particles do not become stuck in the mesh. Yet, acoustic radiation forces have a tendency to retain particles on the mesh elements when the mesh is activated ultrasonically, producing an efficient filter (Wang *et al.* [93]).

Particle Trapping

A focused USW application using lateral radiation forces is described by Hertz [41]. An attempt was made to alleviate some of the shortcomings of using an optical trap by looking into that method. In this example, a strong lateral energy gradient in the standing wave is produced by combining focused ultrasound with two opposing concave transducers (see Fig.(2.14)). In addition to being confined laterally at the field's focus, where they can be retained against the flow of the surrounding fluid, particles in the field agglomerate at a pressure node.

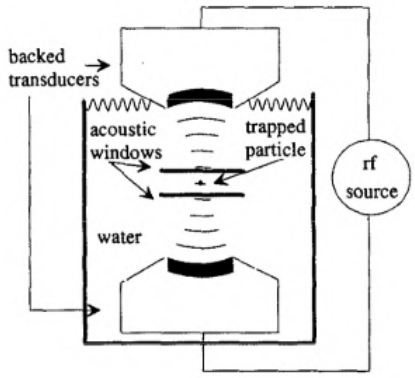

Fig. 2.14 Schematic by Hertz [41]

The application of USW trapping to enhance particle interaction within the trap is made possible by its range of action and secondary radiation forces that have a tendency to attract particles. This has been utilized to interact antigen-coated latex beads and speed up the meningitis agglutination test (Barnes *et al.* [4]). Not only do USWs capture particle aggregation, but they also induce streaming in their surroundings. Mass transfer from the surrounding fluid to the aggregate can be improved via streaming effects as well as static suspension within a moving fluid. This technique was applied by Morgan *et al.* [70] to quickly assess a multicellular spheroid's exposure to a toxicant in motion.

Sensor Enhancement

A container of fluid with parallel, plain edges resonates when pulsed at frequencies of integer multiples of half wavelengths across the domain. In these scenarios, the boundaries will align with maximum pressure and minimum velocity, causing the particles in close proximity to the boundary to be driven towards it instead of a nodal plane that is distant from the surface. As shown by Hawkes *et al.* [40], this has the ability to carry particles to a sensor surface and greatly increase the sensitivity of the sensor system.

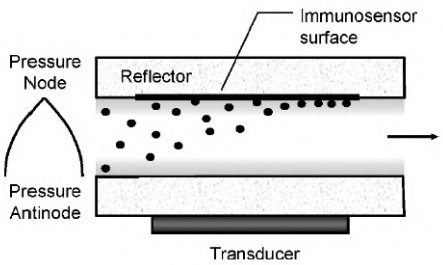

Fig. 2.15 Schematic of sensor enhancement by Hill & Harris [42]

Particle Washing

The laminar flow properties that are built into microfluidic devices are utilized in this application. When two fluids come into contact with one another, they can flow beside one another without significantly mixing. Then, if the acoustic nodes are placed correctly, particles in fluid (B) can be transferred by radiation forces into fluid (A). The fluids can then be divided at the outlets, resulting in the continuous movement of particles from one fluid to another as shown in Fig.(2.16). Using yeast particles, Hawkes *et al.* [37] proved this approach, and a washing rate of roughly 80% could be attained.

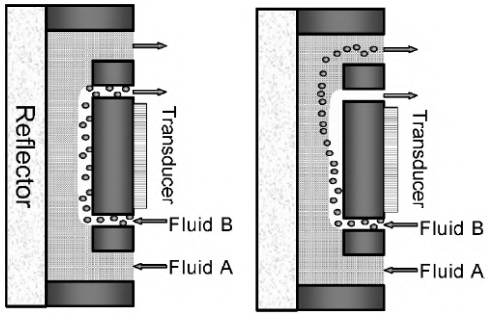

(a) (b)

Fig. 2.16 Principle of cell washing (a) Only diffusion mixing without acoustic field (b) Acoustic radiation force driving particles across the fluid-fluid interface (based on Hawkes *et al.* [37])

Particle Fractionation

Particle fractionation makes it possible to separate a mixture of various particles based on physical characteristics like size and density. By taking advantage of the fact that larger particles translate across laminar flow streams more quickly and that force is related to the cube of particle radius, ultrasound can be utilized to fractionate continuously (Masudo & Okada [65]).

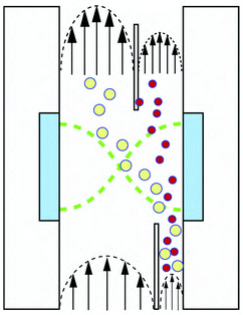

Fig. 2.17 Diagram of the half-wavelength based resonator described by Johnson & Feke [50] for particle size separation

Frequency switching is an additional method of separation in which the acoustic resonator alternates between various resonance modes at predetermined intervals. A two-particle alignment onto the distinct pressure nodes of the distinct frequencies can be achieved by adjusting the amplitude of the used actuation frequency and the actuation intervals appropriately (see Fig.(2.18)). In a device that had a flow coordinated with the frequency swapping between a single node and a triple node resonance, Mandralis & Feke [62] first studied the phenomena known as synchronized ultrasonic flow field fractionation.

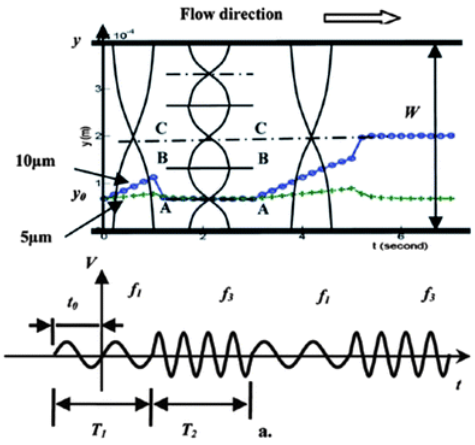

Fig. 2.18 Schematic of particle separation by frequency switching as outlined by Liu & Lim [61]

2.5 Critical Summary of the Literature

From the detailed inspection of the available literature, one can make the following observations:

1. The erosion process in conventional FJP has been extensively studied, showing a W-shape erosion profile for normal impingement angle.
2. No erosion model can claim universal applicability as they are very regime-specific.
3. Several improvisations have been put forward to aid the low material removal rate of conventional FJP, however, the inhomogeneous erosion profile remains unaddressed.
4. A detailed review of particle manipulation techniques reveals the suitability of acoustophoresis. To the best of our knowledge, we are not aware of works that employ acoustic fields to manipulate particles in the FJP process.

2.6 Thesis Objectives

As mentioned earlier, the current work presents a Proof-of-Concept study of a novel acoustophoresis-assisted Fluid Jet Polishing technique. The phenomenon is explored here through detailed numerical simulation involving a combination of Eulerian & Lagrangian approaches. Correspondingly, the objectives of this thesis are :

1. Study of pressure fields and acoustic radiation forces on suspended particles in fluid media in different geometric configurations.
2. Developing a computational model to mimic the FJP process.
3. Numerical modeling of acoustophoretic intervention in circular FJP.
4. Numerical modeling of acoustophoretic intervention in square FJP.
5. Characterization of square FJP with a detailed parametric analyses.

Chapter 3

Mathematical Background

In this chapter, the mathematical framework is developed to deal with the non-linear effects of acoustic radiation force acting on particles in an acoustic field. The governing equations for analyzing such acoustophoretic effects are essentially the mass balance, momentum balance, and thermodynamic equation of state. These non-linear governing equations would be decomposed into equations of increasing orders of magnitude by using the perturbation theory to evaluate the forcing on the particles.

The chapter also deals with the equations for computational modelling of the particle-laden fluid jet impingement process, which involves multiphase flow equations for modelling the continuum and Lagrangian equations for particle dynamics.

Finally, the experimental findings of a few small-scale acoustophoresis experiments in different geometric domains have also been presented.

3.1 Acoustofluidics: Governing Equations

The density, pressure, and velocity fields of the fluid domain are represented by their Eulerian descriptions, ρ (**x**,t), p (**x**,t), and v (**x**,t), under the assumption that the fluid is isotropic and Newtonian. The Navier-Stokes equations governing the fluid flow are presented in vector formulation as follows.

$$\frac{\partial \rho}{\partial t} + \nabla.(\rho \mathbf{v}) = 0 \tag{3.1}$$

$$\rho(\frac{\partial \mathbf{v}}{\partial t} + \mathbf{v}.\nabla\mathbf{v}) = -\nabla p + \mu\nabla^2\mathbf{v} + (\frac{\mu}{3} + \mu_B)\nabla\nabla.\mathbf{v}. \tag{3.2}$$

Here, μ and μ_B are the dynamic and bulk viscosity, respectively. The overall processes are assumed to be isothermal, and hence, the energy equation is not explicitly considered in the current work. The equation of state here describes acoustic pressure as a function of

density.

$$p = p(\rho) \tag{3.3}$$

3.2 Perturbation Theory

In the perturbation theory, the desired solution is expressed as a power series, referred to as a perturbation series. The departure from the precisely solvable zeroth-order field is quantified by a 'small' parameter called the perturbation coefficient, ε. Here, ε is the acoustic Mach number, defined as the ratio of peak acoustic particle velocity to the local speed of sound, c_0. The contribution of the acoustic field to the pressure, density, and velocity fields are considered to be small perturbations, p_1, ρ_1, and $\boldsymbol{v}_1$ to the steady, equilibrium base state of p_0, ρ_0 and $\boldsymbol{v}_0$.

Thus, any variable according to perturbation theory can be expanded as

$$y = y_0 + \varepsilon y_1^{'} + \varepsilon^2 y_2^{'} + \varepsilon^3 y_3^{'} + ... + \varepsilon^n y_n^{'} \tag{3.4}$$

This expression can be implicitly written as

$$y = y_0 + y_1 + y_2 + y_3 + ... \tag{3.5}$$

where

$$y_n = \varepsilon^n y_n^{'}$$

The acoustic variables can, therefore, be expressed as

$$p = p_0 + p_1 + p_2 + ... \tag{3.6}$$

$$\rho = \rho_0 + \rho_1 + \rho_2 + ... \tag{3.7}$$

$$\boldsymbol{v} = \boldsymbol{v}_0 + \boldsymbol{v}_1 + \boldsymbol{v}_2 + ... \tag{3.8}$$

The subscripts '0', '1', '2', and so on represent the zeroth-, first-, and second-order variables, respectively. Since the third- and higher-order acoustic variables have a far smaller effect on the acoustophoretic motion of particles than the first three orders, they are disregarded. The state relation for the pressure can be expanded using a Taylor series as

$$p = p_0 + (\frac{\partial p}{\partial \rho})(\rho - \rho_0) + \frac{1}{2}(\frac{\partial^2 p}{\partial \rho^2})(\rho - \rho_0)^2$$

$$\text{i.e., } p = p_0 + c_0^2(\rho_1 + \rho_2) + \frac{1}{2}(\partial_\rho c^2)_0(\rho_1 + \rho_2)^2 \tag{3.9}$$

where

$$\frac{\partial p}{\partial \rho} = c_0^2$$

is the isentropic speed of sound. The continuity and the momentum equations can be rewritten in the following form.

$$\partial_t \rho = -\nabla.(\rho \boldsymbol{v}) \tag{3.10}$$

$$\rho \partial_t \boldsymbol{v} = -\nabla p - \rho(\boldsymbol{v}.\nabla)\boldsymbol{v} + \mu\nabla^2\boldsymbol{v} + \beta\mu\nabla(\nabla.\boldsymbol{v}) \tag{3.11}$$

3.2.1 Zeroth order perturbation expansions

Taking the perturbation expansions of the acoustic variables in the zeroth order, we get

$$\begin{aligned} p &= p_0 \\ \rho &= \rho_0 \\ \boldsymbol{v} &= \boldsymbol{v}_0 \end{aligned} \tag{3.12}$$

The velocity at the base state is assumed to be zero as the fluid is quiescent. Thus,

$$\boldsymbol{v} = 0$$

Now, substituting these variables in the equations (3.10) and (3.11), we get

$$\begin{aligned} \partial_t \rho_0 &= 0 \\ \nabla p &= 0 \end{aligned} \tag{3.13}$$

3.2.2 First order perturbation expansions

Taking the perturbation expansions of the acoustic variables up to the first order, we get

$$\begin{aligned} p &= p_0 + c_0^2\rho_1 \\ \rho &= \rho_0 + \rho_1 \\ \boldsymbol{v} &= \boldsymbol{v}_1 \end{aligned} \tag{3.14}$$

Now, substituting these variables in the equations (3.10) and (3.11), we get

$$\begin{aligned} \partial_t \rho_1 &= -\rho_0 \nabla.(\boldsymbol{v}_1) \\ \rho_0 \partial_t \boldsymbol{v}_1 &= -c_0^2 \nabla\rho_1 + \mu\nabla^2\boldsymbol{v}_1 + \beta\mu\nabla(\nabla.\boldsymbol{v}_1) \end{aligned} \tag{3.15}$$

3.2.3 Second order perturbation expansions

The first-order fields arising from the acoustic excitation are assumed to have harmonic dependence. Thus, they do not contribute to any time-averaged effect since these quantities reduce to zero when integrated over a time period of oscillation. Hence, we move on to the second-order expansions.

$$\begin{aligned} p &= p_0 + c_0^2\rho_1 + p_2 \\ \rho &= \rho_0 + \rho_1 + \rho_2 \\ \boldsymbol{v} &= \boldsymbol{v}_1 + \boldsymbol{v}_2 \end{aligned} \tag{3.16}$$

Substituting these in the Eqns. (3.10) and (3.11), we get

$$\partial_t \rho_2 = -\rho_0 \nabla.(\boldsymbol{v}_2) - \nabla.(\rho_1 \boldsymbol{v}_1) \tag{3.17}$$

$$\rho_0 \partial_t \boldsymbol{v}_2 = -\nabla p_2 - \rho_1 \partial_t \boldsymbol{v}_1 - \rho_0 (\boldsymbol{v}_1.\nabla)\boldsymbol{v}_1 + \mu \nabla^2 \boldsymbol{v}_2 + \beta\mu \nabla(\nabla.\boldsymbol{v}_2) \tag{3.18}$$

Now, time-averaging the above equations over a time period of wave oscillation, we have

$$\rho_0 \nabla. < \boldsymbol{v}_2 > = -\nabla. < \rho_1 \boldsymbol{v}_1 > \tag{3.19}$$

$$\nabla < p_2 > = - < \rho_1 \partial_t \boldsymbol{v}_1 > -\rho_0 < (\boldsymbol{v}_1.\nabla)\boldsymbol{v}_1 > + \mu < \nabla^2 \boldsymbol{v}_2 > + \beta\mu \nabla(\nabla. < \boldsymbol{v}_2 >) \tag{3.20}$$

The terms inside angular brackets are time-averaged quantities. Neglecting the small contributions from viscous terms, we get

$$\nabla < p_2 > = - < \rho_1 \partial_t \boldsymbol{v}_1 > -\rho_0 < (\boldsymbol{v}_1.\nabla)\boldsymbol{v}_1 > \tag{3.21}$$

Substituting the first-order expansion of the Navier-Stokes equation (3.15) in the above expression, we obtain

$$\nabla < p_2 > = - < \rho_1 (\frac{-c_0^2}{\rho_0} \nabla \rho_1) > -\rho_0 < \frac{1}{2} \nabla \boldsymbol{v}_1^2 >$$

$$\nabla < p_2 > = \frac{1}{2} \frac{c_0^2}{\rho_0} \nabla < \rho_1^2 > - \frac{\rho_0}{2} \nabla < \boldsymbol{v}_1^2 > \tag{3.22}$$

Consequently, the second-order acoustic pressure in the inviscid bulk, temporally-averaged, is given by

$$< p_2 > = \frac{\kappa_0}{2} < p_1^2 > - \frac{\rho_0}{2} < \boldsymbol{v}_1^2 > \tag{3.23}$$

where

$$\kappa_0 = \frac{1}{\rho_0 c_0^2}$$

is the compressibility of the fluid.

3.3 Acoustic radiation force on a spherical particle

The following assumptions have been made prior to deriving the acoustic radiation force.

1. The wavelength of the acoustic field, 'λ', is much greater than the spherical particle radius, 'a'.

2. Owing to the small size of the particles, the first-order scattering theory is considered.

3. Multiple scattering or secondary scattering events are not considered.

4. The fluid is assumed to be inviscid.

Subsequently, the acoustic radiation force is obtained by evaluating the surface integral of the temporally averaged second-order pressure p_2 and momentum flux tensor $\rho_0 < \boldsymbol{v}_1 \boldsymbol{v}_1 >$ over any closed surface enclosing the particle as

$$F_{rad} = -\oint \{< p_2 > \boldsymbol{n} + \rho_0 < (\boldsymbol{n}.\boldsymbol{v}_1)\boldsymbol{v}_1 >\} ds$$

i.e.,

$$F_{rad} = -\oint \{(\frac{\kappa_0}{2} < p_1^2 > -\frac{\rho_0}{2} < \boldsymbol{v}_1^2 >)\boldsymbol{n} + \rho_0 < (\boldsymbol{n}.\boldsymbol{v}_1)\boldsymbol{v}_1 >\} ds \tag{3.24}$$

Following the procedure established by Gor'kov [32], the velocity potential, Φ, is written as a sum of the incident and the scattered parts.

$$\Phi = \Phi_{in} + \Phi_{sc} \tag{3.25}$$

Φ_{sc} is derived entirely from incident field quantities. After some algebraic simplifications, the potential, 'U', corresponding to the acoustic force, 'F', that acts on a small spherical particle in an ideal fluid and an arbitrary acoustic field can be written as

$$U = 2\pi R^3 [f_1 \frac{< p_{in}^2 >}{3\rho c^2} - f_2 \frac{\rho < v_{in}^2 >}{2}], \tag{3.26}$$

where $< p_{in}^2 >$ and $< v_{in}^2 >$ are the mean square variations in the pressure and velocity value at the particle location. Here, the velocity potential can be written as

$$\begin{aligned} p_{in} &= -\rho \frac{\partial \Phi_{in}}{\partial t} \\ v_{in} &= \nabla \Phi_{in}. \end{aligned} \tag{3.27}$$

The factors 'f_1' and 'f_2' are the monopole and dipole scattering coefficients, respectively and are expressed as

$$\begin{aligned} f_1 &= 1 - \frac{\rho c^2}{\rho_p c_p^2} \\ f_2 &= 2\frac{(\rho_p - \rho)}{(2\rho_p + \rho)} \end{aligned} \tag{3.28}$$

Here, the quantities with subscript 'p' refer to the particles. Finally, the acoustic force acting on the particle can be computed by using the relation

$$F = -\nabla U \tag{3.29}$$

3.3.1 Cylindrical Domain

We now investigate the acoustic radiation force components and the nodal surfaces in a cylindrical frame of reference (Barmatz & Collas [3]). For cylindrical domains, the spatial directions are designated by (ϕ, r, z), and the normal modes are given by the integer quantum numbers (m, n, n_z), respectively. Correspondingly, the velocity potential for a standing wave in the cylindrical system is given by

$$\Psi_{in} = -\Psi_o J_m(k_{mn} r) cos(m\phi) cos(k_{n_z} z) sin(\omega t) \tag{3.30}$$

Here, the wavenumber k is written as

$$k = \omega / c = (k_{mn}^2 + k_{n_z}^2)^{1/2} \tag{3.31}$$

with

$$\begin{aligned} k_{mn} &= \frac{\pi \alpha_{mn}}{a} \\ k_{n_z} &= \frac{\pi n_z}{l_z} \end{aligned} \tag{3.32}$$

α_{mn} is the n^{th} solution of the relation,

$$\frac{d[J_m(\pi\alpha)]}{d\alpha} = 0 \tag{3.33}$$

J_m is the Bessel function of order m. Here, rigid boundary conditions have been assumed. Ψ_0 is the amplitude of the incoming acoustic wave and is defined as the ratio of acoustic particle velocity (v_0) to the wavenumber. In this thesis, the acoustic particle velocity of $v_0 = 10m/s$ has been used throughout. We will quantify the influence of such a velocity consideration in Chapter 5.

According to Eq.(3.27), the acoustic pressure and velocity field for any mode can be written as

$$p_{in} = \Psi_o \rho \omega J_m(k_{mn}r)cos(m\phi)cos(k_{n_z}z)cos(\omega t) \tag{3.34}$$

$$v_{in} = -\frac{k_{mn}\Psi_o}{2}[J_{m-1}(k_{mn}r) - J_{m+1}(k_{mn}r)]cos(m\phi)cos(k_{n_z}z)sin(\omega t)\hat{e}_r + \frac{m\Psi_o}{r}J_m(k_{mn}r)$$
$$sin(m\phi)cos(k_{n_z}z)sin(\omega t)\hat{e}_\phi + k_{n_z}\Psi_o J_m(k_{mn}r)cos(m\phi)sin(k_{n_z}z)sin(\omega t)\hat{e}_z \tag{3.35}$$

The time-averaged and squared values of these quantities are

$$< p_{in}^2 >= \frac{\Psi_o^2 \rho^2 \omega^2}{2} J_m(k_{mn}r)^2 cos^2(m\phi)cos^2(k_{n_z}z) \tag{3.36}$$

$$< v_{in}^2 >= \frac{k_{mn}^2\Psi_o^2}{4}[J_{m-1}(k_{mn}r) - J_{m+1}(k_{mn}r)]^2 cos^2(m\phi)cos^2(k_{n_z}z) + \frac{m^2\Psi_o^2}{2r^2}J_m(k_{mn}r)^2$$
$$sin^2(m\phi)cos^2(k_{n_z}z) + \frac{k_{n_z}^2\Psi_o^2}{2}J_m(k_{mn}r)^2 cos^2(m\phi)sin^2(k_{n_z}z) \tag{3.37}$$

Substituting these variables in Eq. (3.26) gives the expression for the acoustic force potential in a cylindrical domain as

$$U = \pi R^3 \rho \Psi_o^2 [\frac{f_1\omega^2}{3c^2}J_m(k_{mn}r)^2 cos^2(m\phi)cos^2(k_{n_z}z) - \frac{f_2}{2}\{\frac{k_{mn}^2\Psi_o^2}{4}[J_{m-1}(k_{mn}r) - J_{m+1}(k_{mn}r)]^2$$
$$cos^2(m\phi)cos^2(k_{n_z}z) + \frac{m^2\Psi_o^2}{2r^2}J_m(k_{mn}r)^2 sin^2(m\phi)cos^2(k_{n_z}z)$$
$$+ \frac{k_{n_z}^2\Psi_o^2}{2}J_m(k_{mn}r)^2 cos^2(m\phi)sin^2(k_{n_z}z)\}] \tag{3.38}$$

Consequently, the acoustic radiation force along the radial direction can be determined from Eq.(3.29) as

$$F_r = -\frac{\partial U}{\partial r}\hat{e}_r$$

$$\begin{aligned} F_r = -\pi R^3 \rho \Psi_o^2 [\frac{f_1 \omega^2}{3c^2} k_{mn} J_m(k_{mn}r)(J_{m-1}(k_{mn}r) - J_{m+1}(k_{mn}r)) cos^2(m\phi) cos^2(k_{n_z}z) \\ - \frac{f_2}{2}\{\frac{k_{mn}^3}{4}(J_{m-1}(k_{mn}r) - J_{m+1}(k_{mn}r))(J_{m-2}(k_{mn}r) - 2J_m(k_{mn}r) + J_{m+2}(k_{mn}r)) cos^2(m\phi) cos^2(k_{n_z}z) \\ + m^2 sin^2(m\phi) cos^2(k_{n_z}z) \frac{r^2 J_m(k_{mn}r)(J_{m-1}(k_{mn}r) - J_{m+1}(k_{mn}r)) - 2rJ_m(k_{mn}r)^2}{r^4} \\ + k_{n_z}^2 k_{mn} J_m(k_{mn}r)(J_{m-1}(k_{mn}r) - J_{m+1}(k_{mn}r)) cos^2(m\phi) sin^2(k_{n_z}z)\}]\hat{e}_r \end{aligned} \quad (3.39)$$

Similarly, the acoustic radiation force along the other two spatial directions can be written as

$$\begin{aligned} F_\phi = \frac{\pi R^3 \rho \Psi_o^2 m sin(2m\phi)}{r} [\frac{f_1 \omega^2}{3c^2} J_m(k_{mn}r)^2 cos^2(k_{n_z}z) + \frac{f_2}{2}\{-\frac{k_{mn}^2}{4}(J_{m-1}(k_{mn}r) - J_{m+1}(k_{mn}r))^2 \\ cos^2(k_{n_z}z) + \frac{m^2}{r^2} J_m(k_{mn}r)^2 cos^2(k_{n_z}z) - k_{n_z}^2 J_m(k_{mn}r)^2 sin^2(k_{n_z}z)\}]\hat{e}_\phi \end{aligned} \quad (3.40)$$

$$\begin{aligned} F_z = \pi R^3 \rho \Psi_o^2 k_{n_z} sin(2k_{n_z}z) [\frac{f_1 \omega^2}{3c^2} J_m(k_{mn}r)^2 cos^2(m\phi) + \frac{f_2}{2}\{-\frac{k_{mn}^2}{4}(J_{m-1}(k_{mn}r) - J_{m+1}(k_{mn}r))^2 \\ cos^2(m\phi) \frac{m^2}{r^2} J_m(k_{mn}r)^2 sin^2(m\phi) + k_{n_z}^2 J_m(k_{mn}r)^2 cos^2(m\phi)\}]\hat{e}_z \end{aligned} \quad (3.41)$$

For an axisymmetric mode with no axial variation, i.e., a purely radial incident wave with quantum numbers $(0, n, 0)$, the velocity potential can be written as

$$\Psi_{in} = -\Psi_o J_0(k_{0n}r) sin(\omega t) \quad (3.42)$$

Following the procedure established before, the corresponding radial force can be obtained as

$$F_r = \pi R^3 \Psi_0^2 \rho k_{0n}^3 [\{J_0(k_{0n}r)(\frac{2f_1}{3} + \frac{f_2}{2}) - J_2(k_{0n}r)\frac{f_2}{2}\} J_1(k_{0n}r)] \quad (3.43)$$

According to Eqs. (3.32) & (3.33), the first four radial modes in a water-filled circular domain of 4 mm radius correspond to the following frequencies: 225.64, 431.21, 599.06, & 784.57 (kHz). A representative example of the acoustic pressures and radiation forces for purely radial forcing in a 2D circular domain of the modes mentioned above is shown in Fig. 3.1.

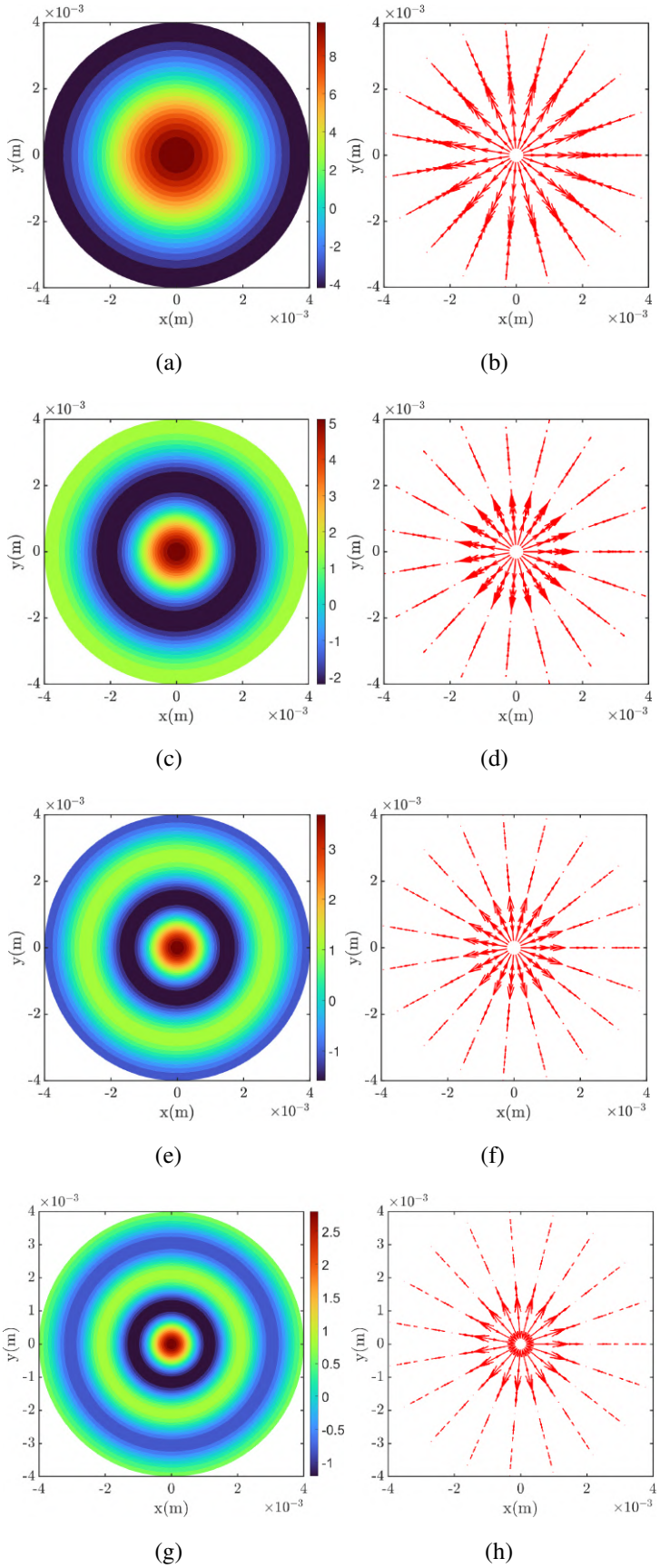

Fig. 3.1 Pressure contour plot and corresponding force vectors for the first four modes of radial acoustic forcing

From Fig.3.1, it can be inferred that the pressure nodes for this particular forcing and domain are concentric circles. If particles of positive acoustic contrast factor are introduced here, they will experience an acoustic radiation force given by Eq. (3.43), which would drive the particles towards the nearest pressure nodes, thereby forming concentric ring patterns as shown in Fig.3.2.

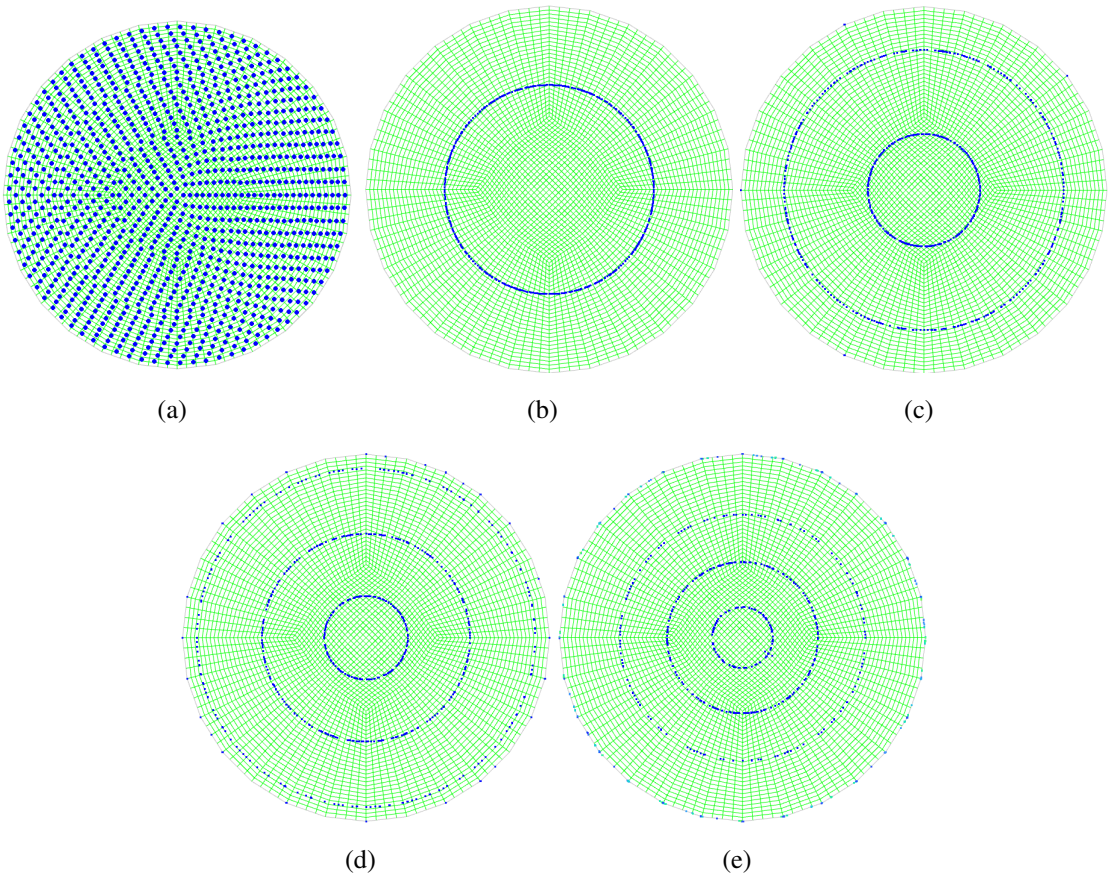

Fig. 3.2 Particle distribution (a) initial (b) with 1st radial mode (c) with 2nd radial mode (d) with 3rd radial mode (e) with 4th radial mode

3.3.2 Cuboidal/Rectangular Domain

This section investigates the acoustic radiation force components and the nodal surfaces for cuboidal/rectangular geometry (Barmatz & Collas [3]). For these domains, the spatial directions are designated by x, y, and z coordinates, and the normal modes are given by the integer quantum numbers (n_x, n_y, n_z). The velocity potential for a standing wave field in a

three-dimensional domain of dimensions, $l_x, l_y, \& l_z$, is given by

$$\Psi_{in} = -\Psi_o cos(k_x x) cos(k_y y) cos(k_z z) sin(\omega t) \tag{3.44}$$

where Ψ_o is the amplitude and ω is the temporal frequency. The wavenumber, k, is written as

$$k = \omega/c = (k_x^2 + k_y^2 + k_z^2)^{1/2} \tag{3.45}$$

where

$$\begin{aligned} k_x &= \frac{\pi n_x}{l_x} \\ k_y &= \frac{\pi n_y}{l_y} \\ k_z &= \frac{\pi n_z}{l_z} \end{aligned} \tag{3.46}$$

According to Eq. (3.27), the acoustic pressure and velocity fields for any given mode are

$$p_{in} = \Psi_o \rho \omega cos(k_x x) cos(k_y y) cos(k_z z) cos(\omega t) \tag{3.47}$$

$$\begin{aligned} \boldsymbol{v}_{in} = \Psi_o [k_x sin(k_x x) cos(k_y y) cos(k_z z) sin(\omega t) \hat{e}_x + k_y cos(k_x x) sin(k_y y) cos(k_z z) sin(\omega t) \hat{e}_y \\ + k_z cos(k_x x) cos(k_y y) sin(k_z z) sin(\omega t) \hat{e}_z] \end{aligned} \tag{3.48}$$

The time-averaged and squared values of these quantities are

$$< p_{in}^2 >= \frac{\Psi_o^2 \rho^2 \omega^2}{2} cos^2(k_x x) cos^2(k_y y) cos^2(k_z z) \tag{3.49}$$

$$\begin{aligned} < v_{in}^2 >= \frac{\Psi_o^2}{2} [k_x^2 sin^2(k_x x) cos^2(k_y y) cos^2(k_z z) + k_y^2 cos^2(k_x x) sin^2(k_y y) cos^2(k_z z) \\ + k_z^2 cos^2(k_x x) cos^2(k_y y) sin^2(k_z z)] \end{aligned} \tag{3.50}$$

Substituting these variables in Eq. (3.26) gives the expression for the acoustic force potential in a cuboidal chamber as

$$\begin{aligned} U = \pi R^3 \rho \Psi_o^2 [\frac{f_1 \omega^2}{3c^2} cos^2(k_x x) cos^2(k_y y) cos^2(k_z z) - \frac{f_2}{2} \{k_x^2 sin^2(k_x x) cos^2(k_y y) cos^2(k_z z) \\ + k_y^2 cos^2(k_x x) sin^2(k_y y) cos^2(k_z z) + k_z^2 cos^2(k_x x) cos^2(k_y y) sin^2(k_z z)\}] \end{aligned} \tag{3.51}$$

Thus, the acoustic radiation force in the x-spatial direction can be determined from Eq. (3.29) as

$$F_x = -\frac{\partial U}{\partial x}\hat{e}_x$$

$$F_x = \pi R^3 \rho \Psi_o^2 k_x [\frac{f_1 \omega^2}{3c^2} sin(2k_x x) cos^2(k_y y) cos^2(k_z z) + \frac{f_2}{2}\{k_x^2 sin(2k_x x) cos^2(k_y y) cos^2(k_z z) - k_y^2 sin(2k_x x) sin^2(k_y y) cos^2(k_z z) - k_z^2 sin(2k_x x) cos^2(k_y y) sin^2(k_z z)\}]\hat{e}_x \quad (3.52)$$

Similarly, the acoustic radiation forces in the other two spatial directions can be written as

$$F_y = \pi R^3 \rho \Psi_o^2 k_y [\frac{f_1 \omega^2}{3c^2} cos^2(k_x x) sin(2k_y y) cos^2(k_z z) + \frac{f_2}{2}\{-k_x^2 sin^2(k_x x) sin(2k_y y) cos^2(k_z z) + k_y^2 cos^2(k_x x) sin(2k_y y) cos^2(k_z z) - k_z^2 cos^2(k_x x) sin(2k_y y) sin^2(k_z z)\}]\hat{e}_y \quad (3.53)$$

$$F_z = \pi R^3 \rho \Psi_o^2 k_z [\frac{f_1 \omega^2}{3c^2} cos^2(k_x x) cos^2(k_y y) sin(2k_z z) + \frac{f_2}{2}\{-k_x^2 cos^2(k_x x) cos^2(k_y y) sin(2k_z z) - k_y^2 cos^2(k_x x) sin^2(k_y y) sin(2k_z z) + k_z^2 cos^2(k_x x) cos^2(k_y y) sin(2k_z z)\}]\hat{e}_z \quad (3.54)$$

In a 2D rectangular domain, the velocity potential is given by

$$\Psi_{in} = -\Psi_o cos(k_x x) cos(k_y y) sin(\omega t) \quad (3.55)$$

Following the procedure established before, the forces in the x and y directions are written as

$$F_x = -\pi R^3 \rho \psi_0^2 k_x sin(2k_x x) [\frac{-f_1 \omega^2}{3c^2} cos^2(k_y y) - \frac{f_2}{2}\{k_x^2 cos^2(k_y y) - k_y^2 sin(k_y y)^2\}]\hat{e}_x \quad (3.56)$$

$$F_y = -\pi R^3 \rho \psi_0^2 k_y sin(2k_y y) [\frac{-f_1 \omega^2}{3c^2} cos^2(k_x x) - \frac{f_2}{2}\{k_x^2 sin^2(k_x x) - k_y^2 cos(k_x x)^2\}]\hat{e}_y \quad (3.57)$$

Figure 3.3 shows a representative example of the above-mentioned 2D rectangular forcing in a 5mm x 5mm domain.

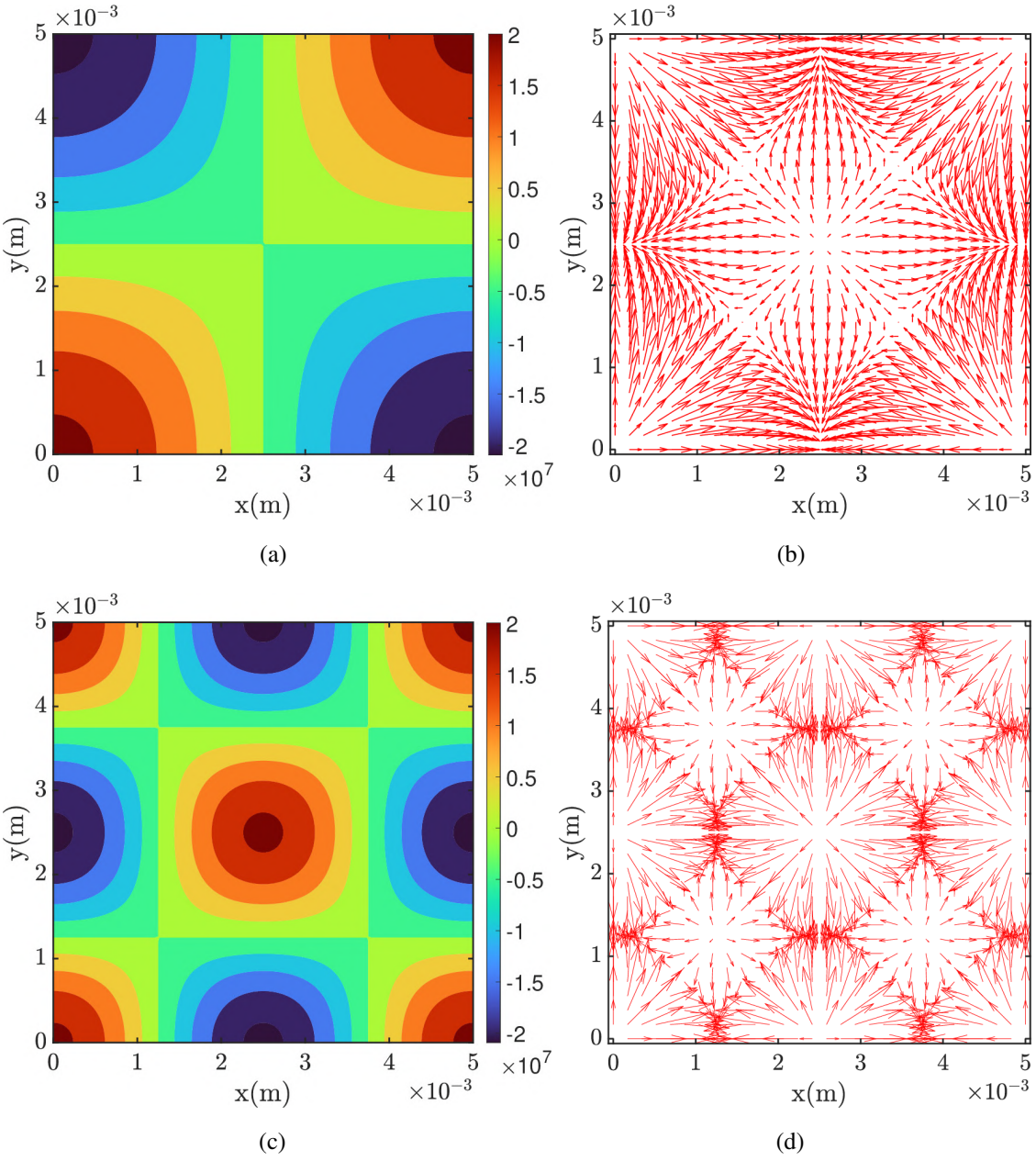

Fig. 3.3 2D rectangular (a) Acoustic pressure contour-mode1 (b) Acoustic force vectors-mode1 (c) Acoustic pressure contour-mode2 (d) Acoustic force vectors-mode2

From Figs. 3.3 (a) & (c), it can be seen that the pressure nodes ($p = 0$) are formed at regions marked by fluorescent green colour. If particles of positive acoustic contrast factor are introduced here, the particles experience acoustic radiation force given by Eq. (3.56) and Eq. (3.57) which push the particles to the aforementioned pressure nodes.

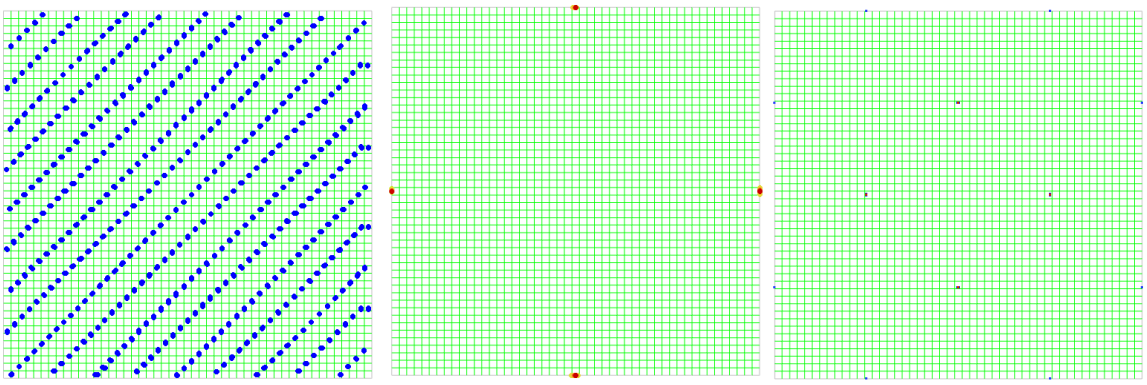

(a) (b) (c)

Fig. 3.4 Particle distribution (a)Initially (b) after acoustic forcing-mode1 (c) after acoustic forcing-mode2

It is evident from the Figures 3.3 & 3.4 that 2D rectangular forcing is incapable of propelling particles towards the centre of the domain. Thus, we go down a stratum and examine 1D rectangular forcing.

$$\Psi_{in} = -\Psi_o cos(k_x x) sin(\omega t) \tag{3.58}$$

The corresponding force in the x-direction is given as

$$F_x = \pi R^3 \rho \psi_0^2 k_x^3 sin(2k_x x)[\frac{f_1}{3} + \frac{f_2}{2}] \tag{3.59}$$

The analogous force in the y-direction can be written as

$$F_y = \pi R^3 \rho \psi_0^2 k_y^3 sin(2k_y y)[\frac{f_1}{3} + \frac{f_2}{2}] \tag{3.60}$$

Figure 3.5 shows pictorially the acoustic force contours and acoustic radiation force vectors for 1D rectangular forcing in x and y-directions, respectively, for the first two modes.

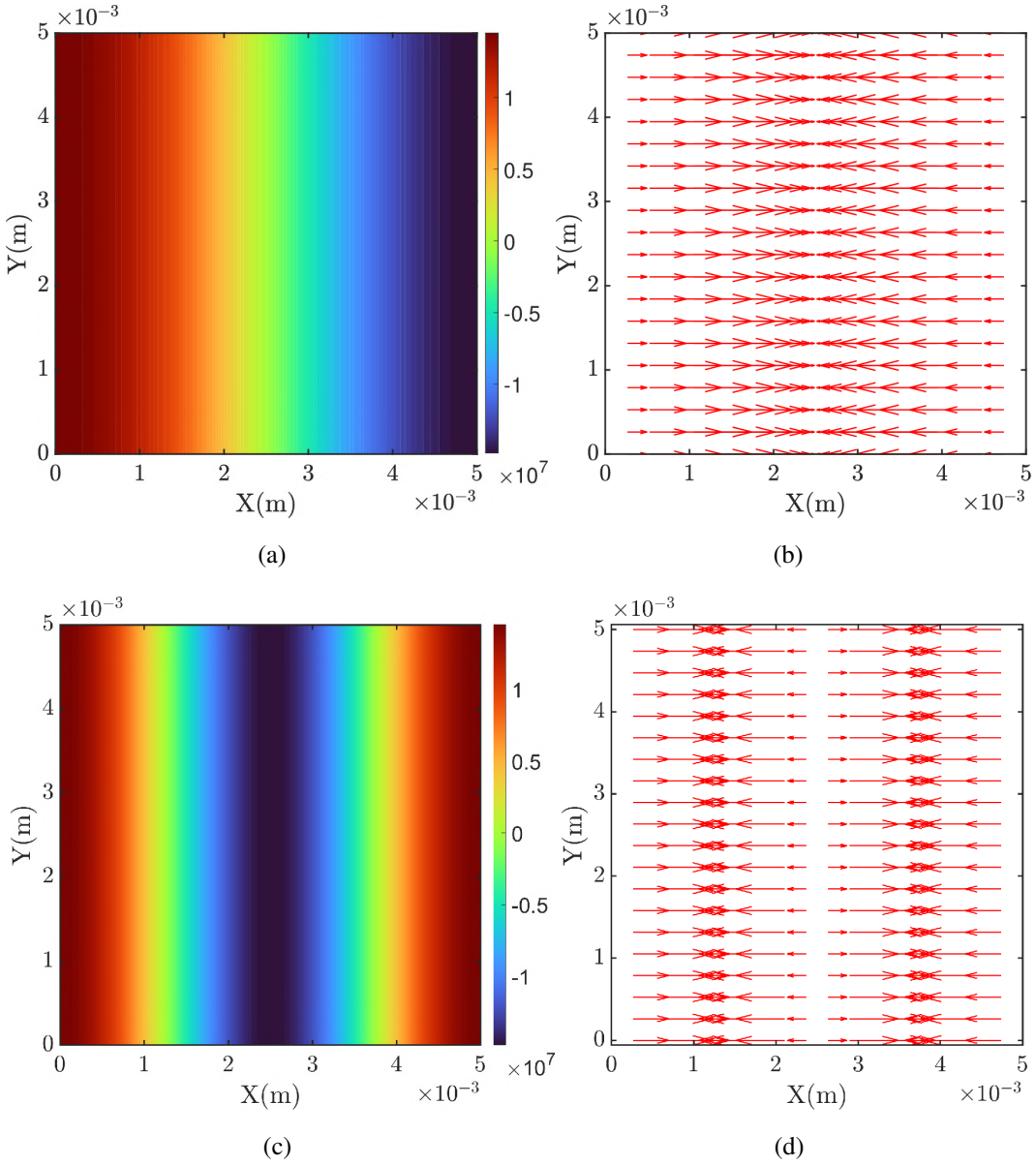

Fig. 3.5 Acoustic pressure contour and force vectors for 1D rectangular forcing in the x-direction: mode1 corresponding to 1st row and mode2 corresponding to 2nd row

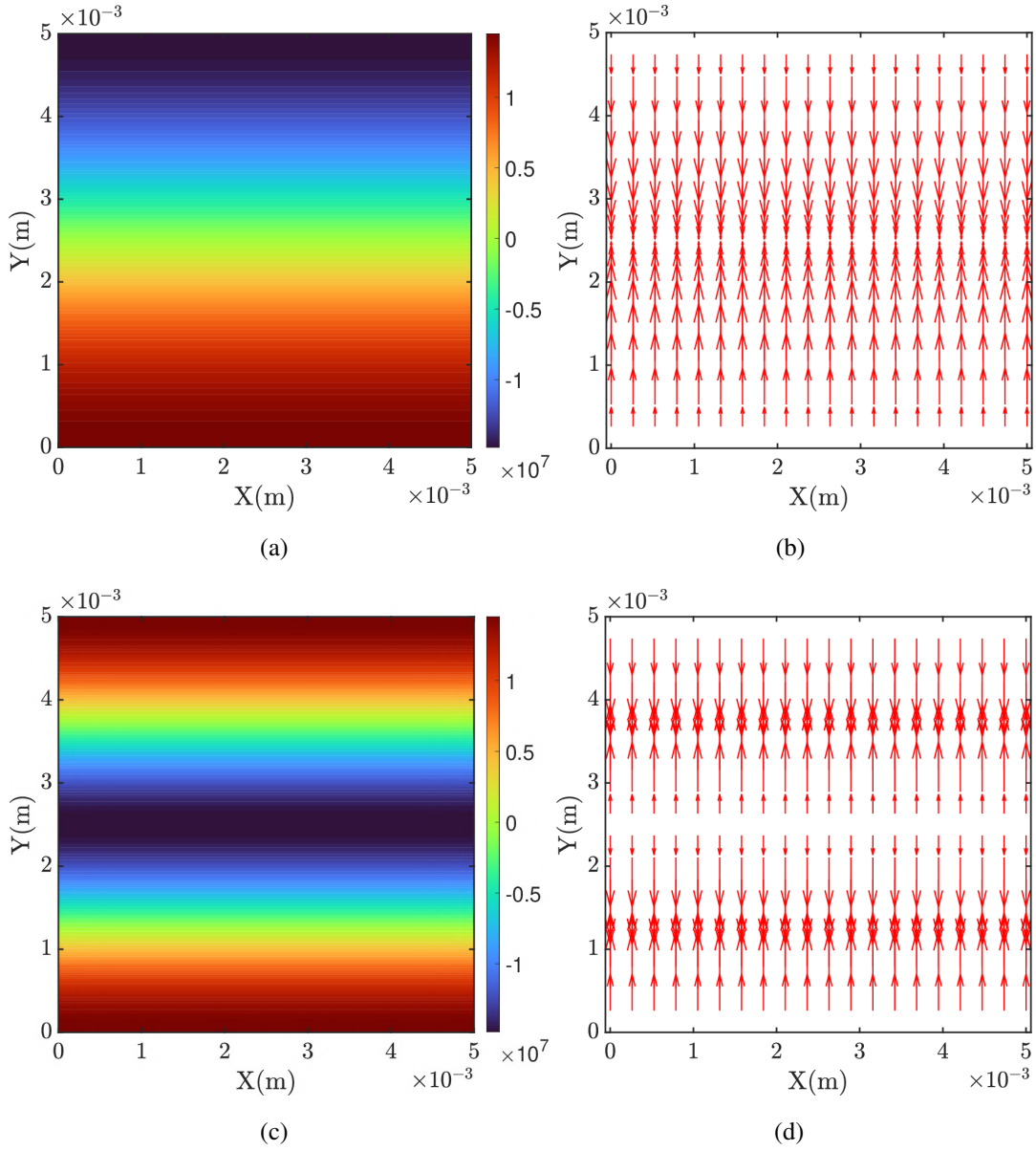

Fig. 3.6 Acoustic pressure contour and force vectors for 1D rectangular forcing in the y-direction: mode1 corresponding to 1st row and mode2 corresponding to 2nd row

The x-direction force drives the particles toward the $x = 0$ line, and the y-direction force drives them towards the $y = 0$ line for the first mode. Similarly, two different stripes of pressure nodes are formed for the second mode in each case. The combination of the forces of the first mode can be exploited to push particles toward the domain centre, which is the intersection of the two pressure node bands as shown in Figs. 3.7 and 3.8.

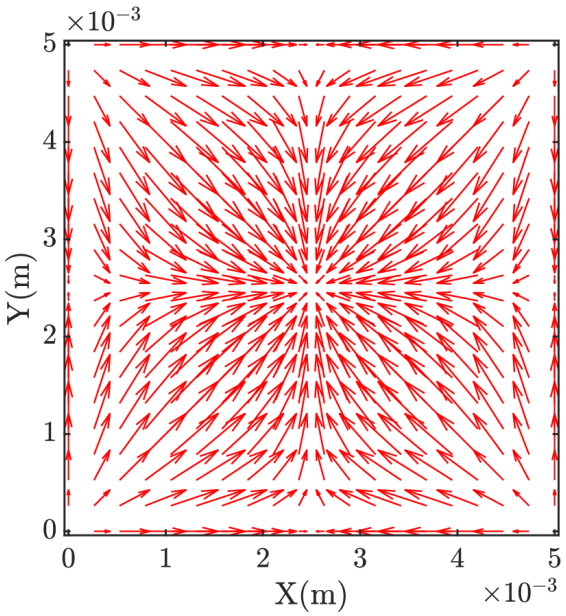

Fig. 3.7 Acoustic force vectors for composite forcing of the first mode

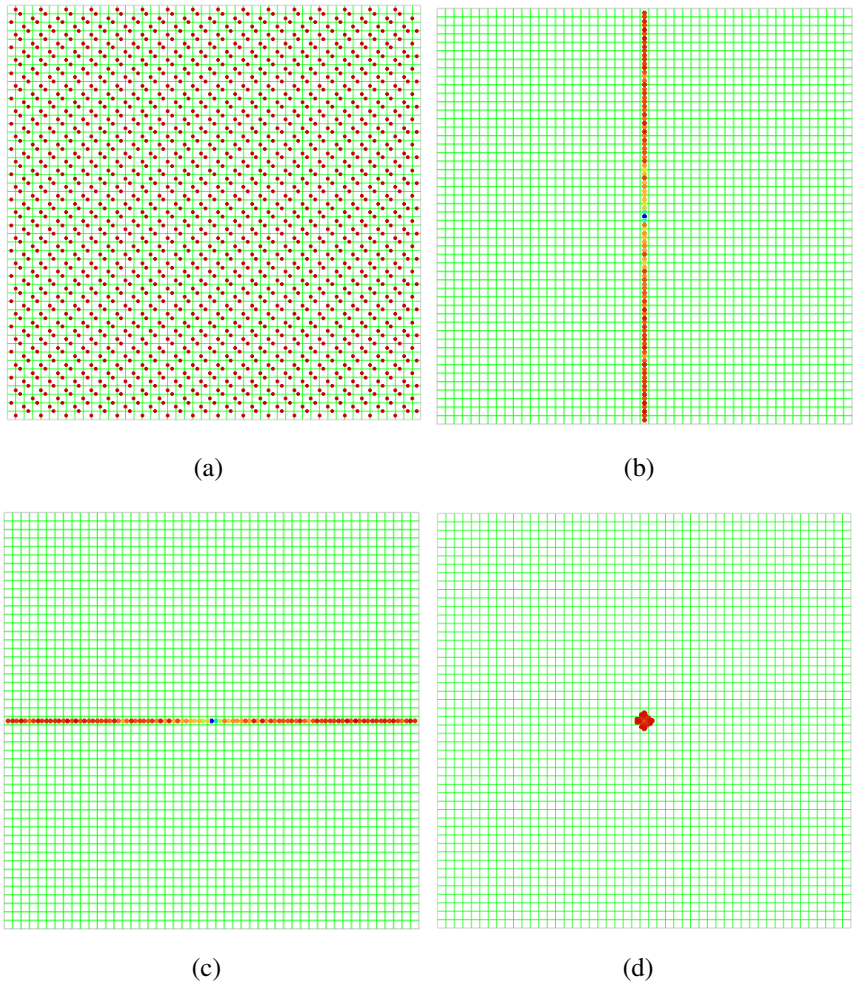

Fig. 3.8 (a)Initial particle distribution (b)Particle distribution with $x-$rectangular forcing (c)Particle distribution with $y-$rectangular forcing (d)Particle distribution with the composite forcing

3.4 Numerical Modelling of the FJP process

With the evaluation of the acoustic forcing terms on the particles, we now write down the equations pertaining to the modelling of the complete FJP process. An Eulerian-Lagrangian approach has been employed here to simulate the two-phase water jet impingement process and the dynamics of the abrasive particles. In this approach, the liquid/air phases are considered to form the continuous phase and their dynamics are modelled using an Eulerian VOF scheme. Meanwhile, the particles are viewed as discrete phases and tracked individually using Lagrangian force balance analysis. A one-way coupling strategy has been deployed wherein the continuous flow governs the particle dynamics, whereas there is no reverse influence. At the outset, the fluid flow is modelled without any abrasive particles. Subsequently, the discrete phase particle trajectories are computed, leading the way for erosion calculation. Both these models have been solved using Ansys-Fluent software.

3.4.1 Continuous Phase

The dynamics of the continuous phase are controlled by the Reynolds averaged Navier-Stokes equations. The energy equation is not explicitly considered, as the flow under analysis is assumed to be isothermal. These equations can be written as

$$\frac{\partial \bar{u}_i}{\partial x_i} = 0 \tag{3.61}$$

$$\rho \bar{u}_j \frac{\partial \bar{u}_i}{\partial x_j} = \frac{\partial}{\partial x_j}[-\bar{p}\delta_{ij} + \mu(\frac{\partial \bar{u}_i}{\partial x_j} + \frac{\partial \bar{u}_j}{\partial x_i}) - \rho\overline{u_i' u_j'}] + \rho \bar{f}_i \tag{3.62}$$

Here, the apparent stress $(-\rho\overline{u_i' u_j'})$ is due to the changing turbulent velocity field and is also known as the Reynolds stress. This Reynolds stress term can be expressed using the Eddy viscosity hypothesis by

$$-\rho\overline{u_i' u_j'} = \mu_t(\frac{\partial U}{\partial x_j} + \frac{\partial U}{\partial x_i} - \frac{2}{3}\frac{\partial U_k}{\partial x_k}\delta_{ij}) - \frac{2}{3}\rho k \delta_{ij} \tag{3.63}$$

where μ_t represents the turbulent viscosity eddy viscosity and k denotes the turbulent kinetic energy.

Turbulence Model

Here, the $k-\varepsilon$ turbulence model has been used to provide closure by relating the Reynolds stress to mean flow quantities. This two-equation model solves for the two variables:

turbulent dissipation rate (ε), which indicates the rate at which turbulent kinetic energy is dissipated, and turbulent kinetic energy (k), which determines the energy in turbulence. The corresponding transport equations are given as

$$\begin{aligned} \frac{\partial(\rho k)}{\partial t} + \frac{\partial(\rho k u_i)}{\partial x_i} &= \frac{\partial}{\partial x_j}[\frac{\mu_t}{\sigma_k}\frac{\partial k}{\partial x_j}] + 2\mu_t E_{ij}E_{ij} - \rho\varepsilon \\ \frac{\partial(\rho\varepsilon)}{\partial t} + \frac{\partial(\rho\varepsilon u_i)}{\partial x_i} &= \frac{\partial}{\partial x_j}[\frac{\mu_t}{\sigma_\varepsilon}\frac{\partial \varepsilon}{\partial x_j}] + C_{1\varepsilon}\frac{\varepsilon}{k}2\mu_t E_{ij}E_{ij} - C_{2\varepsilon}\rho\frac{\varepsilon^2}{k} \end{aligned} \tag{3.64}$$

E_{ij} represents component of rate of deformation and $\mu_t = \rho C_\mu \frac{k^2}{\varepsilon}$ represents the eddy viscosity. The default values provided in Ansys-Fluent have been used for the empirical constants and are given as
$C_\mu = 0.09$, $\sigma_k = 1.00$, $\sigma_\varepsilon = 1.30$, $C_{1\varepsilon} = 1.44$, and $C_{2\varepsilon} = 1.92$

The assumption of no-slip condition on the walls results in significant gradients of the solution variables near the walls, particularly the tangential velocity. The "Low Re" approach, which directly simulates near-wall turbulence, requires very small meshes and customised turbulence models, which significantly raises the computing cost. In this regard, the wall functions model has been utilised to mimic the effects of the near-wall region without resolving all the details of the viscous sublayer and buffer layer. The traditional wall functions use the dimensionless wall distance, y^+, given by

$$y^+ = \frac{u_\tau y}{\nu} \tag{3.65}$$

where y,$u_\tau = \sqrt{\frac{\tau_w}{\rho}}$, and τ_w are the distance from the wall to the first mesh cell centre, friction velocity, and wall shear stress, respectively. The traditional wall functions resemble the velocity profile in the log-law area of the boundary layer for y^+ values typically between 30 and 300.

Scalable wall functions adapt the classic wall functions to assure their validity independent of mesh refinement. This is achieved by introducing a modified dimensionless wall distance y^*, which ensures the wall function does not deteriorate as the first cell height becomes very small. The modified dimensionless wall distance y^* is defined as:

$$y^* = max(y^+, y^+_{scalable}) \tag{3.66}$$

where the threshold value $y^+_{scalable}$ is usually set at 11.225, which corresponds to the junction of the logarithmic (log-law region) and linear (viscous sublayer) profiles.

Volume of Fluid method

The Volume of Fluid (VOF) method by Hirt & Nichols [44] is implemented to simulate the multi-phase jet with water being the primary phase and air being the secondary phase. By working out a single set of momentum equations and monitoring the primary fluid's volume fraction $'F'$ over the domain, the VOF model simulates the dynamics of the immiscible fluids. Every cell in the computational grid tracks the volume fraction of the fluids, and all fluids share a single set of momentum equations. The value of F thus ranges between 0 and 1 based on the fraction of water contained in the cell. The transient evolution of the phases is evaluated using the scalar transport equation for F, given as

$$\frac{\partial F}{\partial t} + \boldsymbol{v}.\nabla F = 0, \tag{3.67}$$

Owing to the discontinuous nature of F, the above equation is often solved geometrically via two steps: a) interface reconstruction and b) fluid advection. The probable location and direction of the liquid-air interface within the cell are determined in the interface reconstruction step while taking the local volume constraint into consideration. The primary fluid's volumetric flux during the advection process is geometrically estimated at all the cell faces to arrive at its net efflux/influx in each cell. Subsequently, the mass and momentum conservation in the domain is achieved through a single set of equations, given as

$$\frac{\partial \rho}{\partial t} + \nabla.(\rho \boldsymbol{v}) = 0$$
$$\frac{\partial (\rho \boldsymbol{v})}{\partial t} + \nabla.(\rho \boldsymbol{v}\boldsymbol{v}) = -\nabla p + \nabla.\bar{\bar{\tau}} + \rho \boldsymbol{g}$$

where the static pressure, stress tensor, and gravitational body force are denoted by the variables p,$\bar{\bar{\tau}}$, and $\rho \boldsymbol{g}$, respectively.

Here, the local properties are calculated based on the volume fraction, F, as follows:

- Cell density: $\rho = F\rho_{water} + (1-F)\rho_{air}$
- Cell viscosity: $1/\mu = F/\mu_{water} + (1-F)/\mu_{air}$

Surface Tension

The VOF model additionally incorporates surface tension effects along the interface of the phases. The current work uses Ansys Fluent's Continuum Surface Force (CSF) model outlined by Brackbill *et al.* [12]. In the CSF model, instead of using a surface tensile

force or a surface boundary condition to mimic the discontinuity, a volume force owing to surface tension is presumed to exist in a small transition area around the interface. The CSF idea utilizes the reality that numerical models of abrupt changes in finite volume and finite difference algorithms are continuous transitions, with fluid properties shifting seamlessly from one fluid to the next. Surface curvature is determined using regional gradients in the surface perpendicular to the area of contact. As the volume fraction of the q_{th} phase, $\boldsymbol{n}$ is the surface normal and is defined as the gradient of α_q.

$$\boldsymbol{n} = \nabla \alpha_q \tag{3.68}$$

The curvature κ in relation to the divergence of the unit normal

$$\kappa = \nabla . \hat{\boldsymbol{n}} \tag{3.69}$$

where $\hat{\boldsymbol{n}} = \frac{\boldsymbol{n}}{|\boldsymbol{n}|}$. The pressure jump across the surface can be used to express surface tension. The divergence theorem can be used to represent the force at the surface as a volumetric force. The source term added to the momentum equation in this regard is as follows.

$$F_{vol} = \sigma_{ij} \frac{\rho \kappa_i \nabla \alpha_i}{\frac{1}{2}(\rho_i + \rho_j)}, \tag{3.70}$$

where ρ is the volume-averaged density.

3.4.2 Discrete Phase

The computation of abrasive particle motion is carried out by the Lagrangian particle tracking technique known as the Discrete Phase Model (DPM) [49]. The abrasive slurry is assumed to be of low concentration, allowing us to use a one-way coupling method without requiring particle-particle interactions. This means the continuous phase is modelled independently of the particulate phase, with the former being used as a basis for the latter's calculations. Inter-particle interactions have been neglected. The force balance on a particle under the DPM model (in x-direction) is written as

$$\frac{dU_p}{dt} = F_D(U - U_p) + \frac{g_x(\rho_p - \rho)}{\rho_p} + F_{add_x} \tag{3.71}$$

where U_p, ρ_p and d_p are the particle velocity, density and diameter. $F_D(U-U_p)$ is the drag force per unit particle mass and the F_D is given as

$$F_D = \frac{18\mu}{\rho_p d_p^2}\frac{C_D Re}{24} \tag{3.72}$$

In Eq. (3.71), U and ρ indicate the fluid velocity and density, and F_{add} denotes additional forces per unit particle mass. Pressure gradient, Saffman lift, and virtual mass forces were considered as the additional forces, which are given below. The acoustophoretic forces defined at the beginning of this chapter will form a part of this force whenever the acoustic effects are included in the analysis.

$$\begin{aligned} F_{p_x} &= (\frac{\rho}{\rho_p})U_{p_i}\frac{\partial U}{\partial x_i} \\ \boldsymbol{F}_{sl} &= \frac{2K\nu^{1/2}\rho d_{ij}}{\rho_p d_p (d_{lk}d_{kl})^{1/4}}(\boldsymbol{v}-\boldsymbol{v_p}) \\ F_{vm_x} &= \frac{1}{2}\frac{\rho}{\rho_p}\frac{d}{dt}(u-u_p) \end{aligned} \tag{3.73}$$

Since the particles used for FJP are not ideal spheres, the particle shape factor, ϕ, can be defined as the ratio of the particle's surface area to the surface area of a sphere with the same volume, is set as 0.8. For such particles, the drag coefficient, C_D, was given by Haider [35] as

$$C_D = \frac{24}{Re}(1+ARe^B) + \frac{C}{1+\frac{D}{Re}} \tag{3.74}$$

where the empirical constants $A, B, C, andD$ are given by

$$\begin{aligned} A &= exp(2.328 - 6.458\phi + 2.448\phi^2) \\ B &= 0.0964 + 0.5565\phi \\ C &= exp(4.905 - 13.894\phi + 18.422\phi^2 - 10.259\phi^3) \\ D &= exp(1.468 - 12.258\phi - 20.732\phi^2 + 15.885\phi^3) \end{aligned} \tag{3.75}$$

An abrasive particle might hit the target surface repeatedly as it passes through the flow field, losing energy with each impact. In particle tracking simulations, this energy expenditure is included by employing a coefficient of restitution (COR), defined as the ratio between a particle's impact and rebound velocities. The impact of the particles on the wall is modeled here using the Grant & Tabakoff [33] rebound model. The coefficient of restitution for the

normal e_n and tangential e_t directions in this model is

$$\begin{aligned} e_n &= 0.993 - 1.76\alpha + 1.56\alpha^2 - 0.49\alpha^3 \\ e_t &= 0.998 - 1.66\alpha + 2.11\alpha^2 - 0.76\alpha^3 \end{aligned} \tag{3.76}$$

where α is the particle impact angle (in radians). With increase in SOD, the average particle impact velocity & angle decreases slightly. This tells us that the vertical distance travelled by the rebounding particles also decreases with increase in SOD. However, the particle movement does not affect the air-fluid interface as we have used one-way coupling.

Rosin-Rammler distribution

The initial particle positions at the nozzle inlet are specified using the Rosin-Rammler distribution, which describes the probability (given below) of the particle's size being less than or equal to a given size. It is a widely used statistical distribution in particle size analysis, especially in the field of powder technology. It is particularly useful because it provides a good fit for a wide range of particle size distributions and can easily represent both coarse and fine particles.

$$F(d) = 1 - e^{-\left(d/\overline{d}\right)^n} \tag{3.77}$$

Here, d is the particle size, $\overline{d}$ is the measure of central tendency or the characteristic particle size at which 63.2% of particles are smaller, and n is the size distribution parameter where a higher n value indicates a narrower size distribution (more uniform particles). In comparison, a lower n value indicates a wider size distribution (more varied particle sizes).

Erosion Model

The particle trajectory and impact pattern obtained from the DPM model can help quantify the extent of erosion occurring on the target surface. In the current work, a modified version of the generalized erosion model presented by Mansouri [63] based on the work of Khanouki [52] has been utilized. The generalized model applies to a wide variety of fluid viscosities. This makes the model a function of Stokes number (St). The model gives the erosion rate, $E_{R,M}$, as a function of particle density, ρ, shape factor, F_s, and particle impact velocity, V_p as

$$E_{R,M} = C\,\rho_p\,F_s\,V_p^{2.41}\,g(\alpha) \tag{3.78}$$

Where,

$$g(\alpha) = \begin{cases} \frac{sin(\alpha)\,(2Kcos(\alpha) - sin(\alpha))}{2K^2P} & \alpha \leq 18.6^o \\ \frac{(cos^2(\alpha) - F(St)sin^2(\alpha))}{2P} & 18.6^o < \alpha < 70^o \\ 0.0005 + (90 - \alpha)0.0015 & 70^o < \alpha < 90^o \end{cases} \tag{3.79}$$

where

$$F(St) = 0.24St^{-0.503} \tag{3.80}$$

C and K are empirical constants. P represents the target material's plastic flow stress, which is thought to be the Vickers hardness H_v. St is the Stokes number of the fluid flow defined as

$$St = \frac{\tau_p U}{D} \tag{3.81}$$

wherein the particle relaxation time is given as

$$\tau_p = \frac{d_p^2 \rho_p}{18\mu_f} \tag{3.82}$$

The mean particle diameter and fluid viscosity are denoted by d_p and μ_f.

The erosion depth in the target material is eventually computed from the following expression

$$h = \frac{E_R \dot{m} t}{\rho_w A} \tag{3.83}$$

where $\dot{m}$ is the mass flow rate of the particulate matter, t is the run time of the test, ρ_w is the target wall density and A is the area of the target surface.

The above Oka and the generalized erosion models perform angular correction uniquely. Figure 3.9 shows the variation of the $g(\alpha)$ function for the two approaches. Here, the angles corresponding to the maxima of the functions are notably different. Incidentally, the original generalized erosion model of Mansouri [63] would have negative $g(\alpha)$ values beyond 75^o, thus yielding a non-physical result. The current model specified in Eq. (3.79) overcomes this issue by suitably modifying the angle function for α values greater than 70^o. The new angle function is always non-negative, as evident in Fig. 3.9.

3.5 Numerical Validation

To validate the above formulations, the submerged jet experiments of Mansouri [63] are now simulated. Though the focus of the current work is the exposed (non-submerged) jets, a

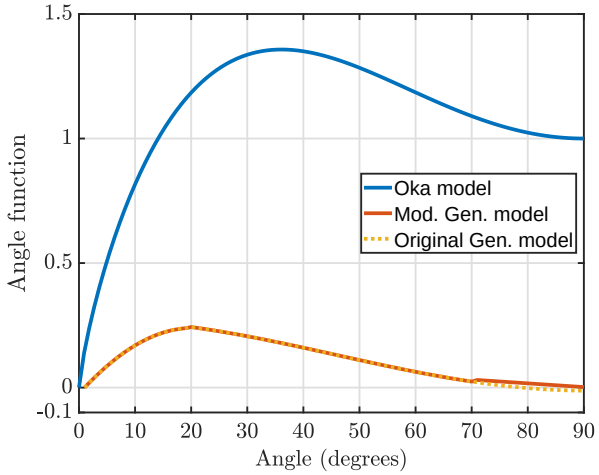

Fig. 3.9 Comparison of angular correction function between Oka model and the generalized model

submerged jet case is chosen here to exclusively validate the DPM and the modified erosion equation. The continuum flow dynamics are still obtained here by solving the Navier-Stokes equations in the Eulerian framework without involving the VOF model for capturing phase redistribution. The operating parameters of Mansouri's experiments [63] are mentioned in Table 1.

Nozzle diameter	8 mm
Stand-off distance	12.7 mm
Nozzle average velocity	14 m/s
Target material	Stainless Steel 316
Nominal particle size	300 μm
Particle concentration (by mass)	1%
Particle density	2650 kg/m^3
Angle of incidence	90^o
Test duration	6 hrs

Table 3.1 Operating parameters used by Mansouri (2015)

In the simulations, the particle distribution at the nozzle inlet has been specified via the Rosin-Rammler distribution, which describes the probability of a particle's size being less

than or equal to the given size as

$$F(d) = 1 - e^{-\left(d/\overline{d}\right)^n}. \tag{3.84}$$

Here, d is the particle size, $\overline{d}$ is the characteristic particle size at which 63.2% of particles are smaller, and n is the size distribution parameter. For the present computations, the specified characteristic particle diameter is 300 μm, and the size distribution parameter is 3.64.

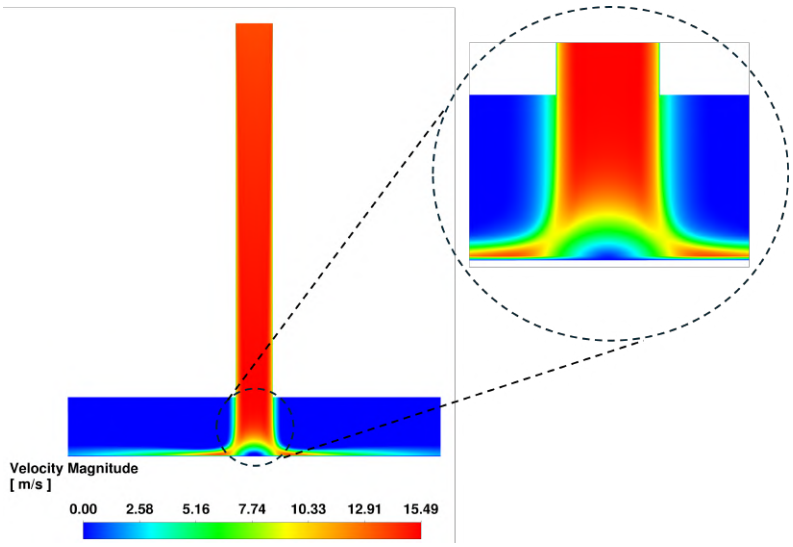

Fig. 3.10 Cross-sectional velocity contour of the submerged impinging jet

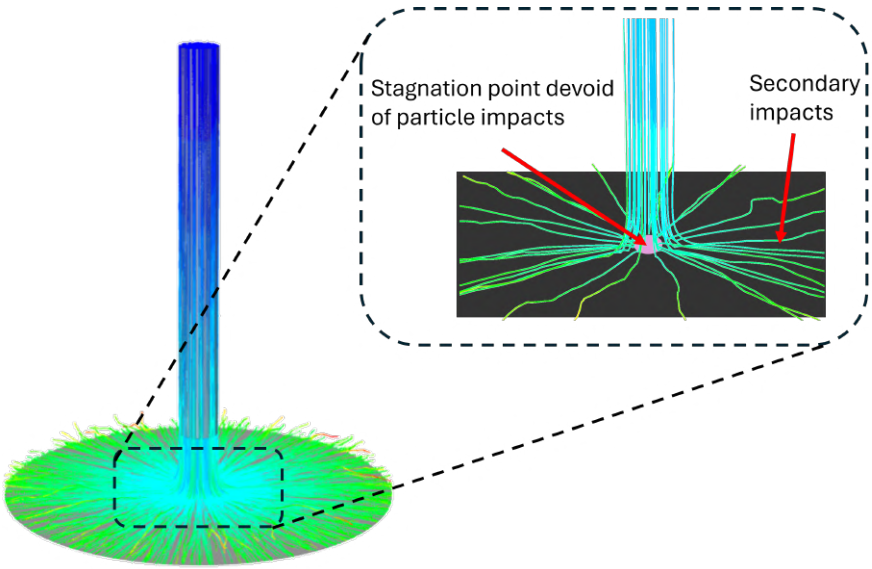

Fig. 3.11 Particle trajectories of circular impinging jet

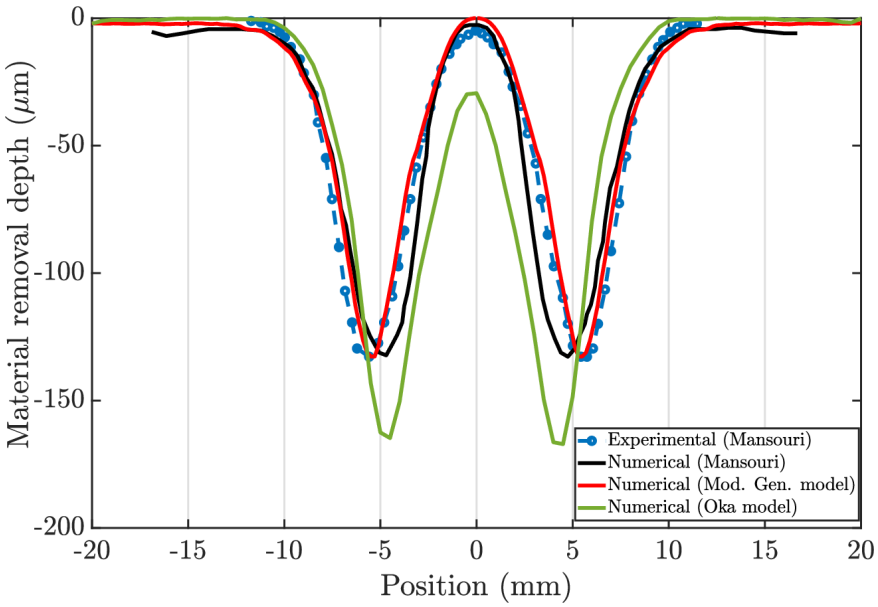

Fig. 3.12 Comparison of erosion profile obtained by Mansouri [63] and the present work

Figures 3.10 and 3.11 show the cross-sectional velocity contour and the particle tracks obtained from the present simulation of Mansouri's experiment [63]. The velocity contour prominently shows the stagnation zone and the features of the radial jet. The particles essentially follow the streamlines and the stagnation zone is devoid of particle impacts. This can be corroborated by the erosion depth data shown in Fig. 3.12, where a notable w-shaped profile can be observed. The maximum erosion occurs around the radius of 6-7 mm and beyond this range; though the erosion decays rapidly, it does not become zero owing to the secondary impacts of the particles in the radial jet region (refer to Fig.3.11). Figure 3.12 demonstrates the capability of the modified generalized erosion equation, whose results are much closer to the experimental data than the numerical simulations of Mansouri [63] and the Oka model. Despite this favourable manifestation by the generalized erosion model, one cannot be very sure of its universal applicability. Hence, we will continue to present the erosion data from both approaches to avoid any model bias.

3.6 Acoustic Levitation Experiments

This section will describe the small-scale acoustophoretic particle manipulation experiment performed to visually illustrate the acoustic radiation force. Acoustic levitation (a form of acoustophoresis) is a technique that uses the forces of acoustic radiation to hang material in the air against gravity. As described previously, the essential physics behind this technique

is the migration of particles toward the pressure nodes of an acoustic standing wave. When an acoustic transducer and a reflector (can be another transducer) are held at a distance which is an integer multiple of the half-wavelength of the wave, a standing pressure wave is established. Light particulate matter, such as styrofoam balls, small water droplets, etc., can be suspended at these particular pressure node locations where the acoustic force supports the weight of the particle. Acoustic levitation offers a wide range of applications because to its ability to prevent interference from the sides of the container and its ease of experimentation. Acoustic levitation has the potential for drop dynamics, biology, analytical chemistry, solidification, and pharmacy due to its ability to prevent intrusion from container walls and ease of experimentation [2].

3.6.1 Experimental Setup & Procedure

The experimental setup consists of a 25 kHz ultrasonic langevin transducer, which is driven sinusoidally by an arbitrary function generator through an RF amplifier. A parabolic reflector is used instead of a flat reflector for more efficient reflection of the sound waves. The light source is also connected to the same function generator and is driven synchronously with the transducer to create a stroboscopic effect. A concave mirror of focal length ($f = 116.4$ cm) is used, and a razor blade is used as the light block. The components required for Schlieren visualization, namely mirror, camera, light source, and light block, are appropriately positioned. Then the transducer, connected to the signal generator and the light source, is switched on, and the reflector position is adjusted vertically above the transducer so that the separation between them is an integer multiple of half-wavelength ($\lambda/2 = 0.685$ cm).

3.6.2 Schlieren visualization

Schlieren optics can be used to display light refraction caused by minute variations in the refractive index of air (n). Because the sound pressure alters the medium's density during sound wave propagation in the test object, affecting the medium's refractive index, it is a useful technique for determining the spread of the sound field in a transparent medium[83].

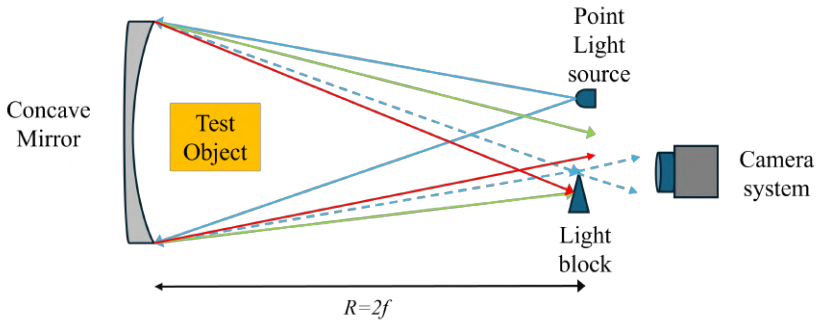

Fig. 3.13 Schemtaic of single mirror Schlieren imaging

A point source of light is focused onto a razor blade edge (shown by dashed lines in Fig. 3.13), which serves as a light block, using a long focal-length mirror. A camera is positioned precisely behind the light block that observes objects in front of the mirror, marked as the "Test Object". The portion of the object with the high refractive index functions as a weak converging lens, causing the light rays to converge somewhat in front of the block before diverging beyond the focal point (shown by red lines in Fig. 3.13). Conversely, the object's low refractive index region will function similarly to a weak diverging lens. As a result, light beams that were previously directed upon the block will converge somewhat behind it (shown by green lines in Fig.3.13). As a result, regions of higher or lower pixel density in the image are a function of variances in the refractive index (n) [25].

The Gladstone-Dale relation states that for gases, the refractive index is linearly dependent on the gas density.

$$n = K\rho + 1 \tag{3.85}$$

Here, the gas density is denoted by ρ and the Gladstone-Dale coefficient by K. A light ray passing obliquely through a change in n bends towards the area with greater n. The ray curvature of a light beam moving in the z-direction that intersects a region with variable n is given by

$$\frac{\partial^2 x}{\partial z^2} = \frac{1}{n}\frac{\partial n}{\partial x} \tag{3.86}$$

Here, x represents a direction perpendicular to the ray propagation. Integrating once, the angular ray deviation is

$$\varepsilon = \frac{1}{n}\int \frac{\partial x}{\partial z}\partial z \tag{3.87}$$

From Eq. (3.87), it can be seen that ray deflection is dependent on the gradients in n orthogonal to the ray propagation direction [18]. The Schlieren technique makes these deflections more apparent.

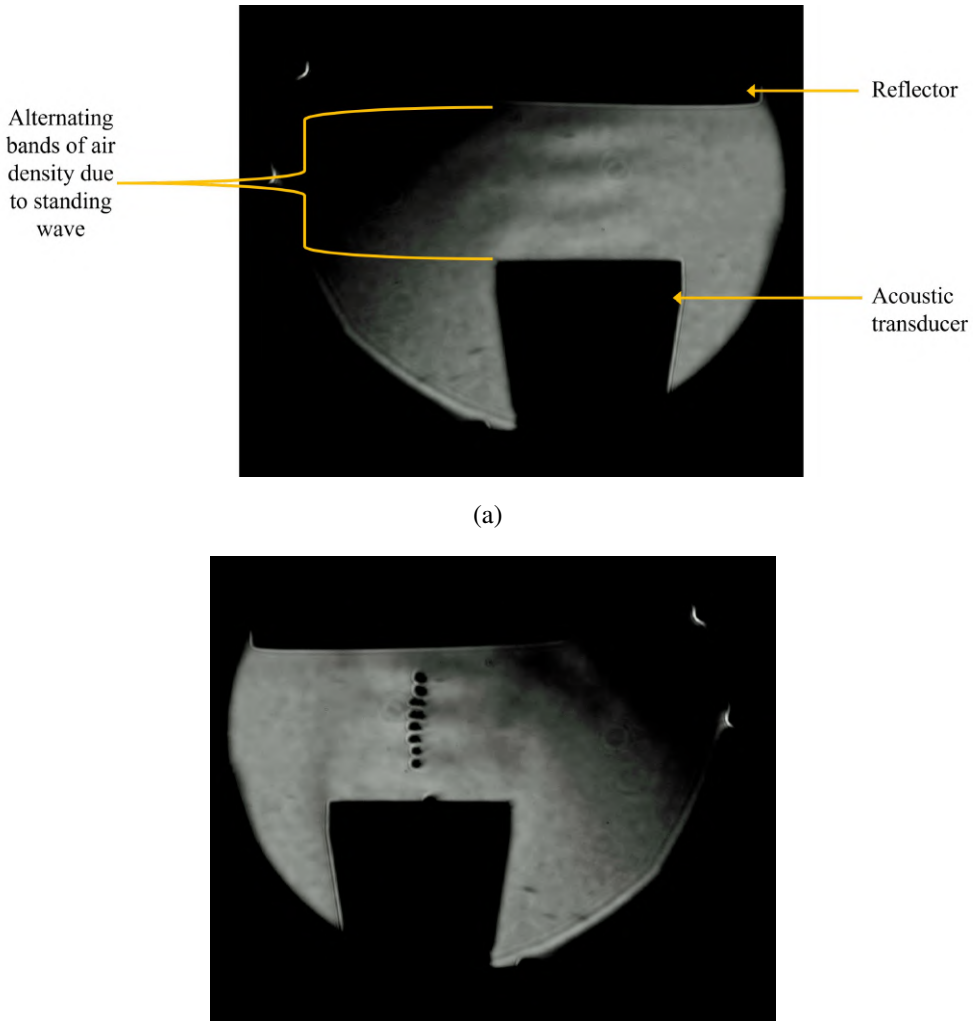

Fig. 3.14 Schlieren visualization of (a) Acoustic standing wave (b) Levitation of Styrofoam particles in the standing wave

Fig. (3.14)(a) shows a snapshot of Schlieren visualization of an acoustic standing wave established by positioning a reflector integer no. of wavelengths above a transducer. This particular technique makes it possible to perceive the acoustic waves via varying bands of air density. Fig. (3.14)(b) shows the levitation of styrofoam balls in the designed wavefield, which clearly shows that the acoustic radiation force counterbalances the weight of the particles. Fig. (3.15) shows the regular visualization of the same phenomenon of styrofoam levitation.

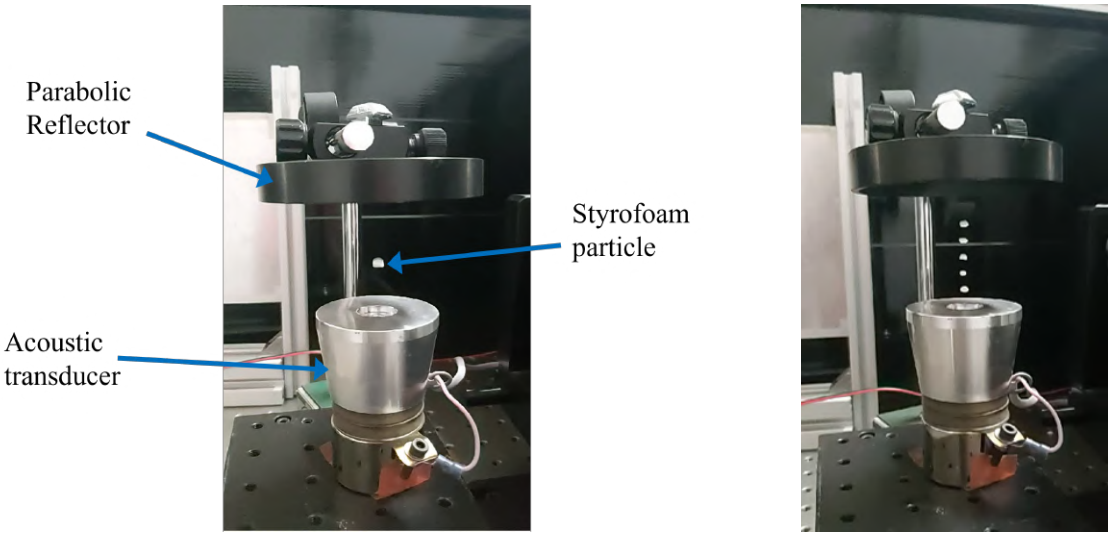

Fig. 3.15 Single-axis acoustic levitation of (a)Single particle (b)Multiple particles

3.7 Closure

This chapter presents the perturbation-based development of the Acoustic Radiation Force, which arises from the fundamental governing equations of continuity, momentum, and state. Under certain assumptions, the expressions for acoustic radiation forces in cylindrical and rectangular domains are derived from the general equation. Subsequently, the mathematical basis behind the different numerical models used to simulate the continuum and discrete phases is described. In addition to this, an erosion plot is presented which validates the above numerical model with the data given by Mansouri [63]. Apart from this, a brief account is provided of the single-axis levitation experiments, and its Schlieren visualization. In the next chapter, we perform detailed simulations of acoustophoretic particle excitation in jets issued from circular cross-sectioned nozzles.

Chapter 4

Acoustophoretic FJP in nozzles with circular cross-section

4.1 Chapter Overview

Conventional FJP systems typically use nozzles of circular cross-sections for various reasons, including maintaining jet stability, convenience of fabrication, etc. In this chapter, we will characterise the migration of abrasive particles under the influence of acoustophoresis in such circular cross-sectioned nozzles. We first describe a small experimental setup that demonstrates the aggregation of particles at circular pressure nodes. This is followed by numerical simulations that show the influence of acoustophoresis on the erosion process in such circular cross-sectioned nozzles. The influence of acoustophoresis on the particles is mimicked here by the forcing terms derived in Chapter 3. These forcing terms are implemented using User Defined Functions (UDFs) in Ansys-Fluent.

4.2 Experimental acoustophoresis in Cylindrical standing wave fields

In this segment, an experimental method to realise acoustophoresis in cylindrical cross-sections has been elucidated. When a radially poled tube transducer is driven sinusoidally, the standing wave pattern turns out to be concentric cylinders running throughout the length of the transducer with the number being proportional to the frequency [3, 68, 95]. This was theoretically described in Section 3.3.1 of the previous chapter. Particles suspended in the media under this pressure field migrate toward the nearest pressure node. Thus, particles appear to form concentric ring patterns when viewed from the top.

Figure 4.1 depicts the acoustic pressure and force in a cylindrical standing wave.

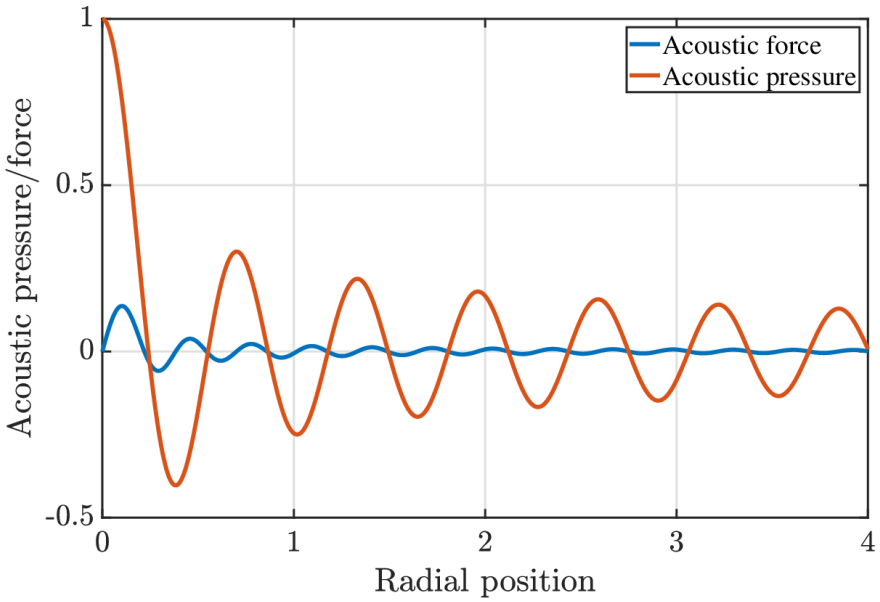

Fig. 4.1 Comparison plot of non-dimensional acoustic pressure & force wrt non-dimensional radial position

4.2.1 Experimental Setup & Procedure

Figure 4.2 shows the experimental setup and cylindrical piezoelectric transducer (PZT) attached to a glass slide. A PZT-5 grade radially poled transducer has been utilised with the following dimensions: outer diameter=12 mm, inner diameter=8mm & height=5mm. This transducer is adhered to a glass slide, and the outer surface is secured using an adhesive tack. The glass slide is then placed on a microscope platform that is illuminated from the bottom. It is then filled with water containing poly-amide micro-particles of size and density, 60 μm and 1030 kg/m^3, respectively. The inner and outer curved surfaces of the transducer, which act as the electrodes, are driven sinusoidally through a function generator and a power amplifier. An electrical sine wave of 10 Vpp was given as an input at the generator. The movement of the particles was observed, and the images were recorded using a camera fitted to the microscope.

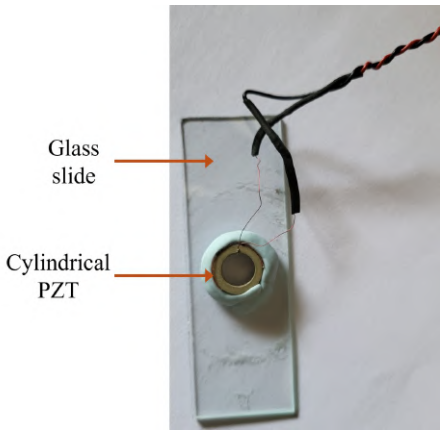

(a)

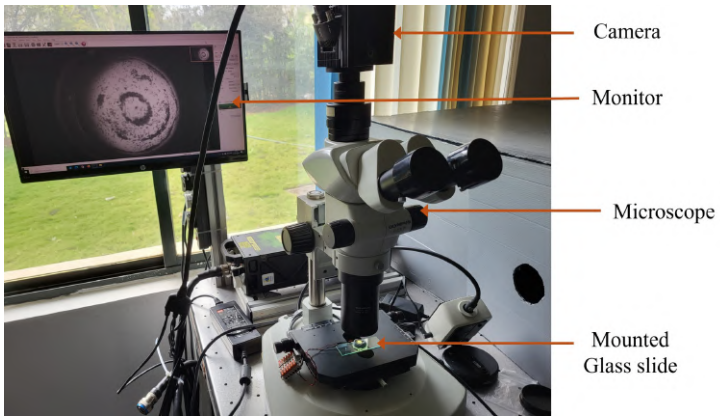

(b)

Fig. 4.2 (a) Glass slide with PZT (b) Visualisation setup of cylindrical acoustophoresis

4.2.2 Experimental Results

Figure 4.3 shows the variation of the concentric pressure node pattern as observed through the camera. A frequency sweep from 1 kHz to 1.2 MHz was performed; however, a few notable ones that show clear particle migration will be presented. Pressure node locations computed through numerical simulations are also presented in conjunction with the experimental results. The red region signals a positive pressure region, the blue region signals a negative pressure region, and the white region between them signals a zero pressure region, corresponding to the pressure node of the cylindrical standing wave (the intensity of the colour represents the amplitude).

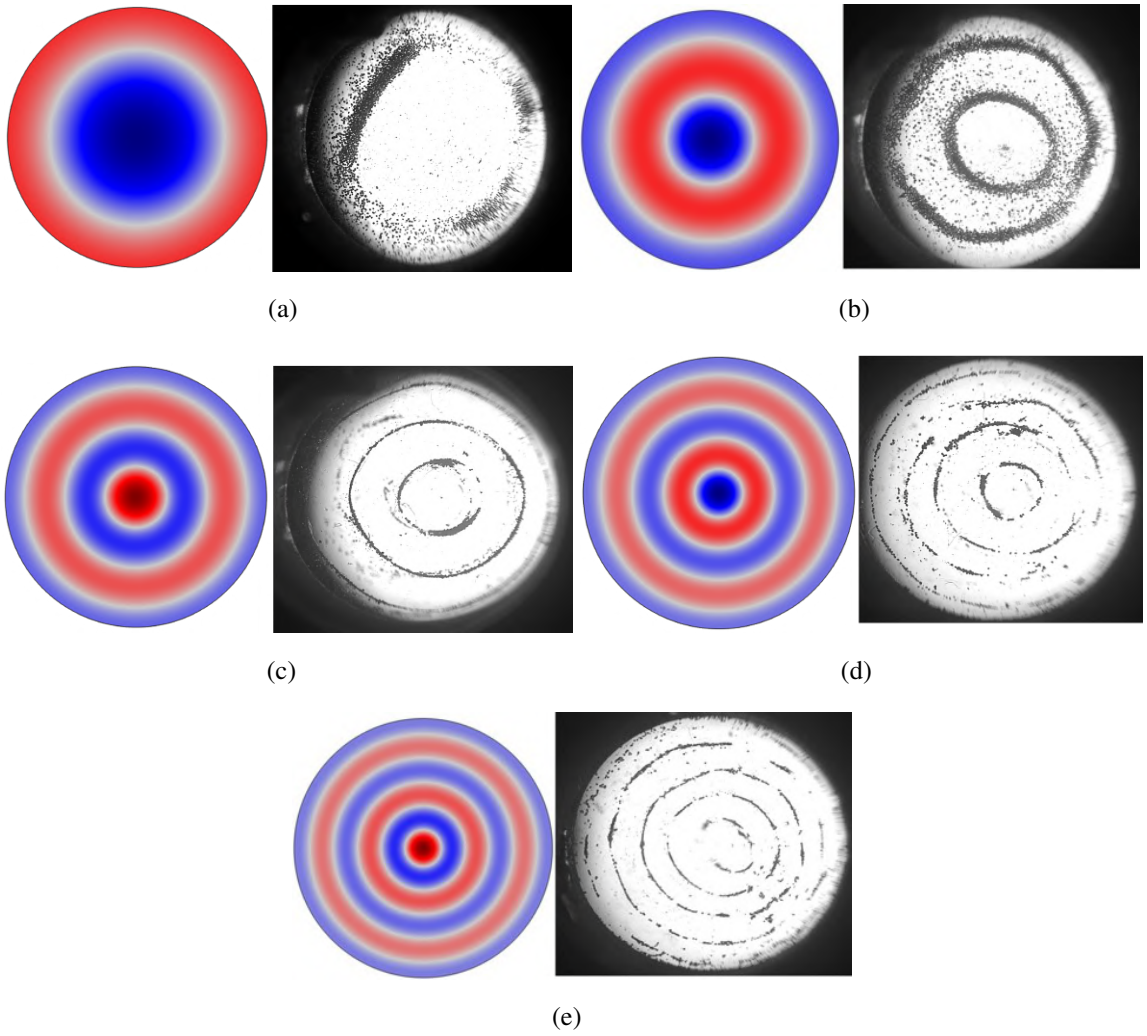

Fig. 4.3 Numerical pressure field contours and corresponding experimental particle migration pattern under different frequencies (a) 210 kHz (b) 415 kHz (c) 600 kHz (d) 800 kHz (e) 1 MHz

Figure 4.3 clearly illustrates the pressure nodes of a cylindrical standing wave at different frequencies and the migration of particles to these aforementioned nodes. The number of pressure nodes formed and the position of the said nodes are identical to the ones shown through numerical simulations for each corresponding frequency. One may see that the rings formed in the experiments are not perfect circles, unlike the numerical pressure field contours. This behaviour is understandable because of irregularities in the acoustic field generated by the PZT, the tendency of particles to agglomerate in the suspending media, and the formation of a meniscus inside the tube.

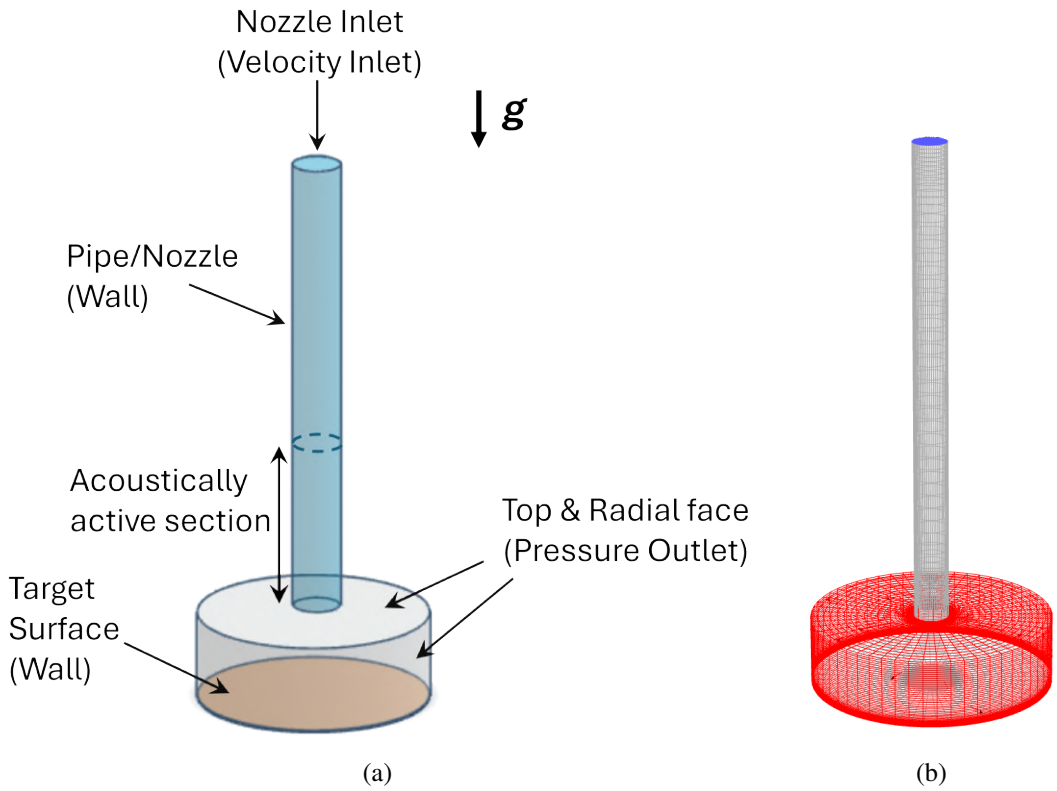

Fig. 4.4 (a)Circular jet geometry and boundary conditions (b) Mesh

4.3 Geometric setup and Boundary conditions of Numerical Simulations

With the experimental verification of concentric rings, we now proceed to the numerical simulation of the acoustophoresis-assisted FJP process. In this regard, the acoustophoretic body force acting on the particles is modelled via Eq.(3.43). Table 4.1 shows the operating parameters utilised for the present set of simulations. As shown in Fig. 4.4, the last 30mm above the nozzle exit is considered to be the acoustically active region. It is assumed that the imposed acoustic standing wave only affects the particle dynamics and does not influence the impinging jet hydrodynamics. In other words, the secondary effects, such as acoustic streaming, are ignored.

Nozzle diameter	5.642 mm
Nozzle length	80 mm
Stand-off distance	2.821, 5.642, 11.284, 22.568 mm
Target plate diameter	40 mm
Nozzle average velocity	10 m/s
Target material	Stainless Steel 316
Nominal particle size	60 μm
Particle concentration (by mass)	1%
Particle density	2650 kg/m^3
Angle of incidence	90^o
Test duration	6 hrs

Table 4.1 Operating parameters for FJP involving circular cross-sections

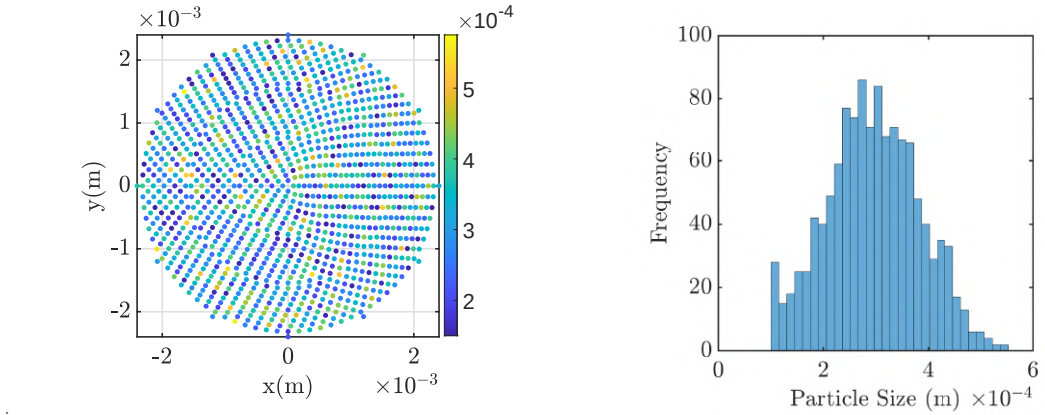

(a) (b)

Fig. 4.5 (a) Particle distribution at the nozzle inlet (b) Rosin-Rammler size distribution frequency

Henceforth, a customised particle injection procedure has been implemented in the discrete phase model for all the simulations presented. One thousand two hundred particles are injected at the discrete locations on the nozzle inlet, as shown in Fig. 4.5(a). These particles have been selected based on a Rosin-Rammler particle size distribution wherein the minimum particle diameter is 1 μm, the maximum particle diameter is 100 μm, the mean particle diameter is 60 μm, and the spread parameter is 3.64. Figure 4.5(b) shows the frequency distribution of particles across this size range.

Furthermore, a turbulent dispersion model is applied, which uses stochastic means to account for the influence of instantaneous turbulent velocity fluctuations on the particle

trajectories. This is achieved by solving the Lagrangian particle tracking equations for each particle using the instantaneous fluid flow velocity, $\overline{u} + u^{'}(t)$. The random effects of turbulence are accounted for by computing and averaging the trajectories for different "number of tries". In the present work, 50 tries have been found optimum as they provide a proper stochastic estimate without making the computations cumbersome.

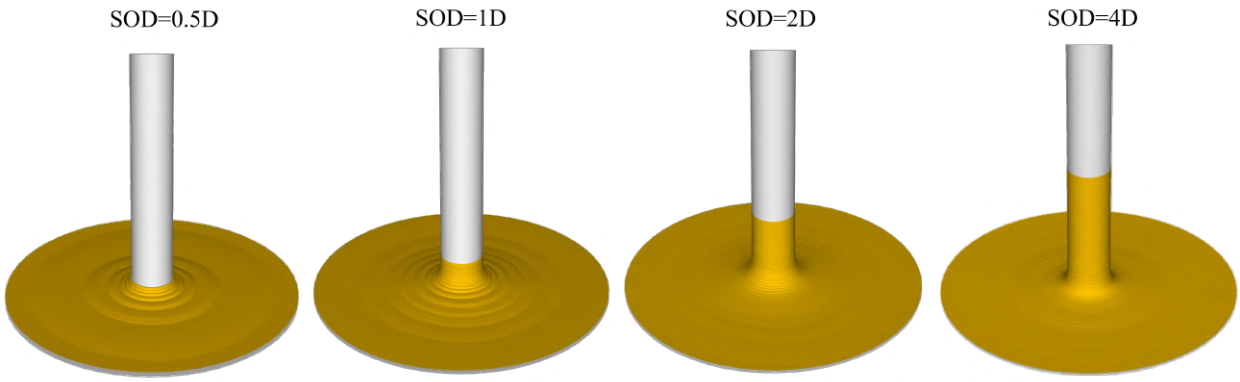

Fig. 4.6 Interface of circular impinging jets at different SODs

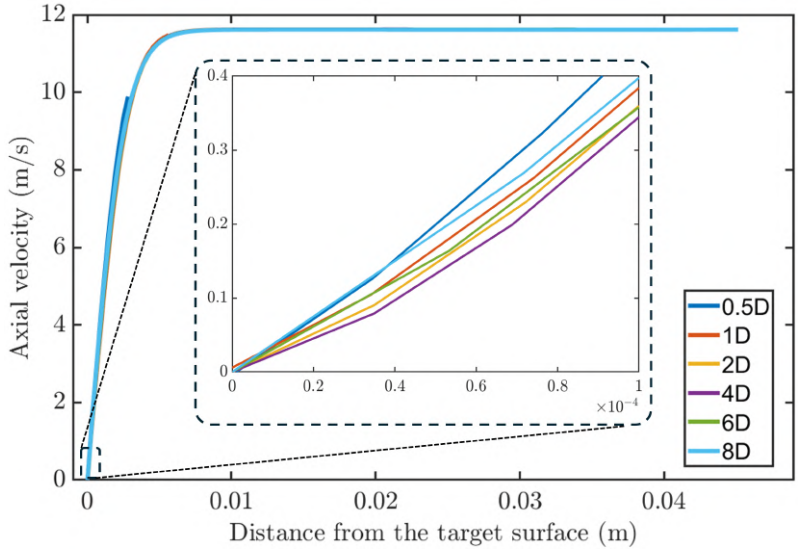

Fig. 4.7 Centreline axial velocity for different SODs

4.4 Results and Discussion

Figure 4.6 shows the impinging liquid jet profile for the four stand-off distances (*SOD*) considered in the present simulations of circular jets. As mentioned before, these profiles

are unaffected by the presence/absence of acoustic excitation. It is obvious that at the lowest *SOD*, i.e., at 0.5*D*, the free-jet region is overwhelmed by the stagnation zone, and the resulting radial jet has numerous surface undulations. These ripples become subdued at higher *SOD*s, and in fact, they completely vanish beyond the *SOD* of 4*D*, as the free-jet region would be adequately formed in such scenarios. It will be shown later that the present acoustophoretic-assisted FJP process becomes ineffective at larger SODs as the particle-focusing effect brought in by acoustophoresis within the nozzle becomes nullified by the turbulent dispersion in the free-jet region. The latter is quite significant for the present jet conditions as its Reynolds number (Re) is around 5.6×10^4. Hence, the analysis here is limited to smaller *SOD* values.

The works of Shi *et al.* [84, 85] and Wang *et al.* [92] show that the material removal depth (peak to valley distance) reaches a maximum at an optimum value of *SOD* and starts to drop thereupon. Such an erosion behaviour basically follows the liquid velocity pattern, which increases till the optimum SOD and decreases beyond it. However, the behaviour of flow velocity with *SOD* in the present simulations is notably different. The axial velocity along the jet axis, as shown in Fig. 4.7, decreases till the *SOD* of 4*D* and increases thereon. The reason for this unique behaviour compared to the published literature can be traced to the difference in the jet configuration. In the present simulations, a uniform 'velocity inlet' is specified at the nozzle inlet, and 'atmospheric pressure outlet' conditions are specified at the outflow boundaries. For such a configuration, the simulations yield the pressure drop in the nozzle to be around 18,000 Pa. However, the works mentioned above use an inlet pressure of around 7 to 8 bar, which far exceeds the pressure drop in the nozzle even after accounting for their smaller nozzle diameters, i.e. around 1.0 to 1.5 mm. Hence, the corresponding jets undergo further acceleration after being issued from the nozzle before the shear stress reigns in to decelerate them. Fortunately, such variations in jet dynamics do not sway the present focus/effort on understanding the influence of acoustophoresis, as the acoustic radiation force exclusively affects particle dynamics.

Proceeding further to the present objective of characterising the acoustophoretic-assisted FJP process in circular nozzles, we now analyse the erosion process for two different frequencies of acoustic excitation. A simple, isolated Lagrangian force calculation on particles in a circular geometry, as in Fig. 4.8(a), using Eq. (3.43) reveals vital information on their final focusing locations, which are concentric pressure nodes obtained from the solutions of the Bessel function. The diameters and the number of the pressure nodes change with the imposed excitation frequency, and it is evident from Fig. 4.8 that two rings are observed for 610 kHz and three rings for 850 kHz. Understandably, the particle impact locations and the erosion profiles in the corresponding acoustophoresis-enabled FJP process

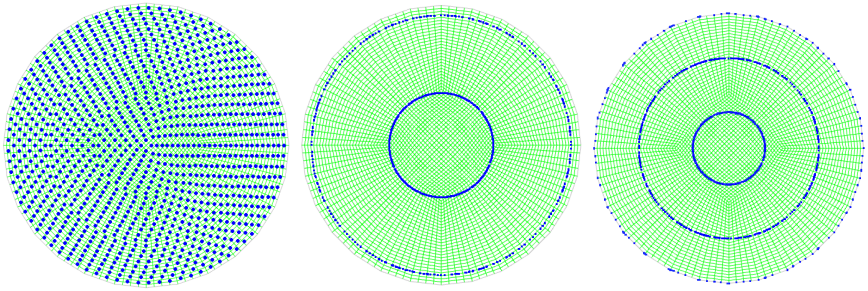

(a) (b) (c)

Fig. 4.8 (a) Initial particle distribution (b) Particle distribution with radial acoustic forcing of $f = 610$ kHz (c) Particle distribution with radial acoustic forcing of $f = 850$ kHz

are greatly influenced by these structures. If increasing the particle size leads to an increase in the volume fraction, then inter-particle interactions become important both for particle dynamics and acoustic field scattering, which has not been considered in this work. However, if the volume fraction is kept constant (in the dilute regime), there is no change in nodal pattern with variation in particle size.

Figure 4.9 shows the number density of particles impacting the target surface at different *SOD*s and acoustic excitation frequencies. Figures 5.7, 5.8, 5.9, and 5.10 show the plot of particle impact velocity and particle impact angle w.r.t radial position for $SOD = 0.5D, 1D, 2D, 4D$, respectively at different acoustic excitation frequencies. The corresponding erosion contours obtained using the Ansys-Fluent's implementation of the Oka model are shown in Fig. 4.14. The influence of acoustophoresis is overwhelmingly evident in these figures. In the case without acoustic excitation, there is a non-uniform scatter of particles over a large region that excludes the stagnation zone. However, with radial acoustic excitation, these particles are focused on precise concentric locations based on the imposed frequency. In fact, for the case of radial acoustic forcing at 610 kHz, the particles' impact and the erosion are focused around a single ring and the corresponding maximum material removal depth, as shown in Fig. 4.15, is twice that of the case without acoustics. Figure 4.15 compares the erosion depths obtained using the modified generalised and Oka models. Here, the two models have a significant difference in the magnitudes of the erosion depths. However, the locations of the peak erosion obtained from the two models seem relatable, and they clearly indicate a notable improvement in the erosion depth due to the additional acoustic excitation. Apart from this improvement, the current technique also provides the capability to adjust the location of the ring accurately by changing the acoustic excitation frequency. At higher frequencies, the number of radial pressure nodes increases and, correspondingly, the number of erosion rings, as observed in the case of 850

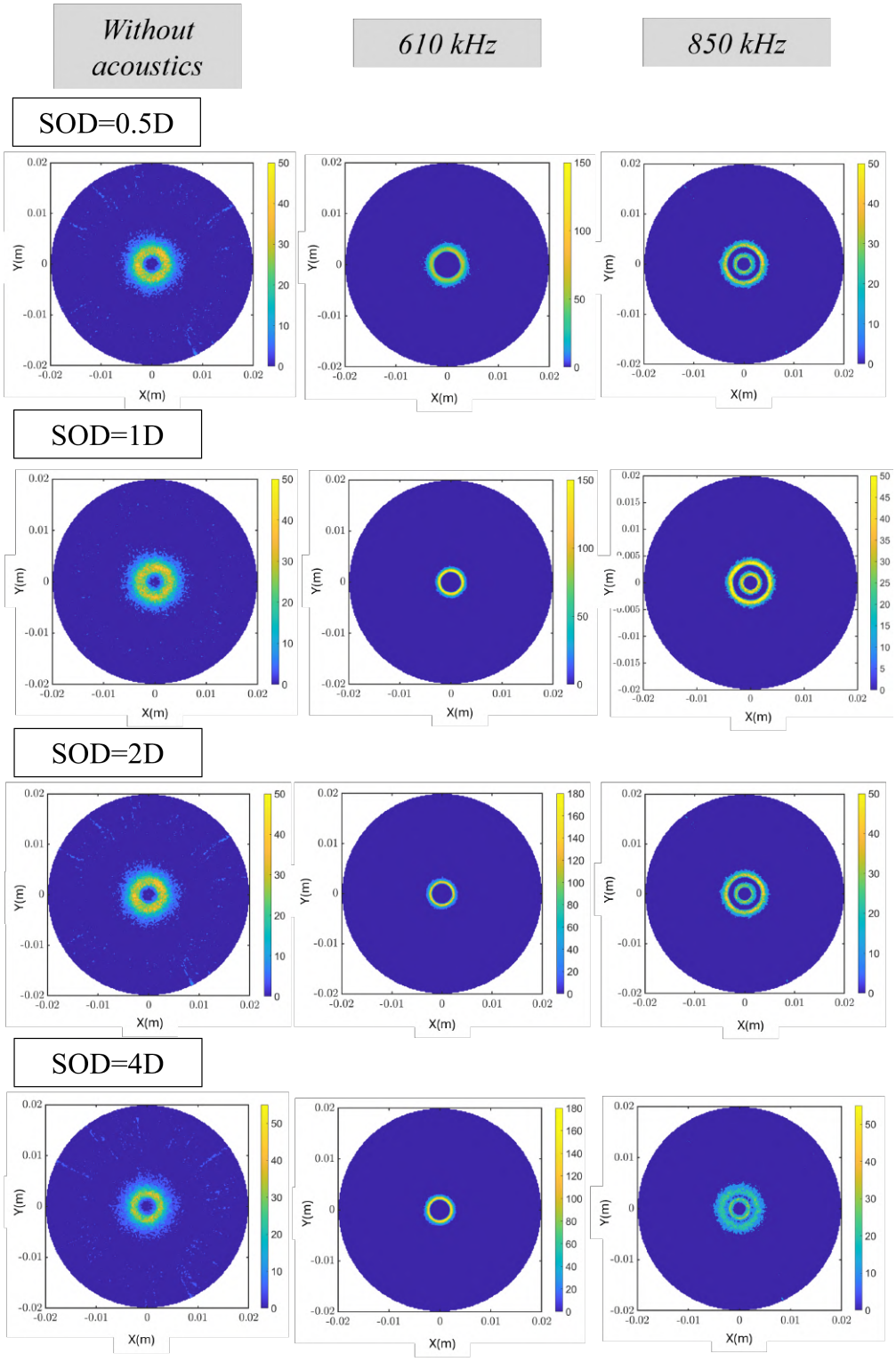

Fig. 4.9 Number density distribution of particles impacting the target surface for various SODs and acoustic frequencies

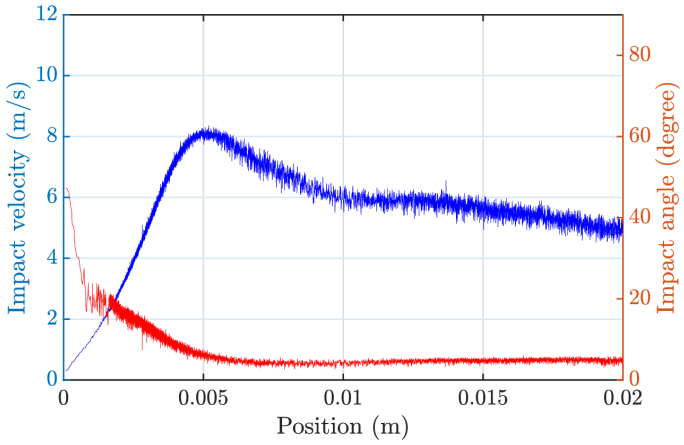

(a)

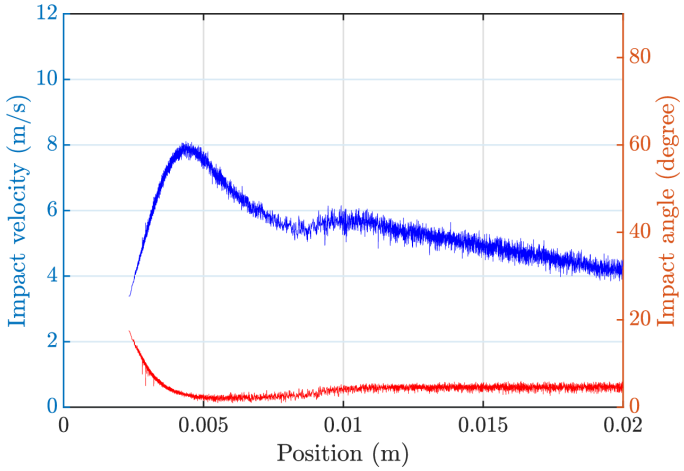

(b)

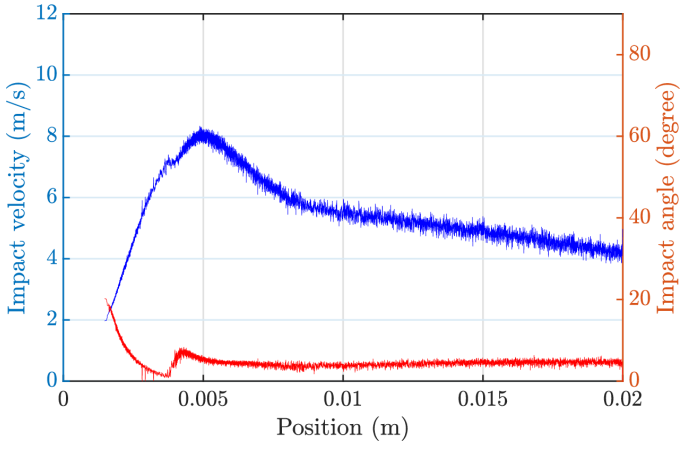

(c)

Fig. 4.10 Particle impact velocity and impact angle plot for SOD=0.5D (a) Without acoustics (b) 610 kHz (c) 850 kHz

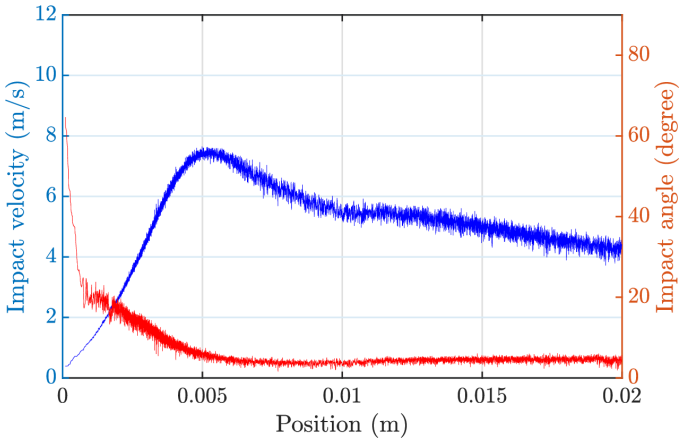

(a)

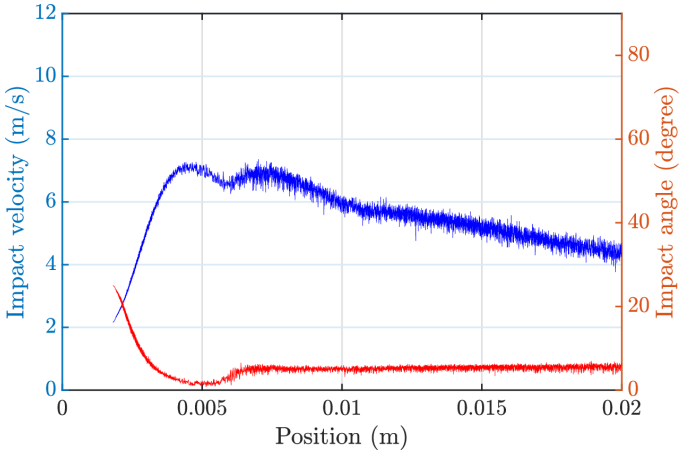

(b)

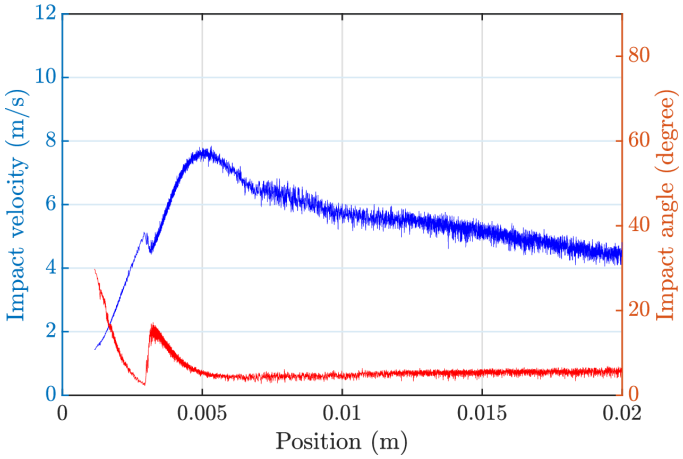

(c)

Fig. 4.11 Particle impact velocity and impact angle plot for SOD=1D (a) Without acoustics (b) 610 kHz (c) 850 kHz

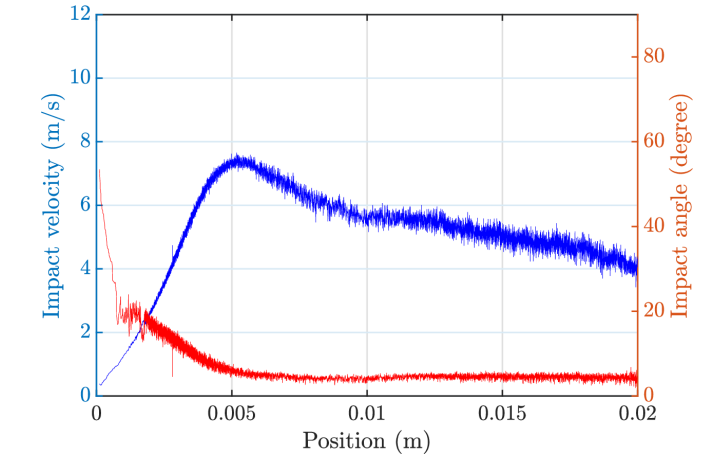

(a)

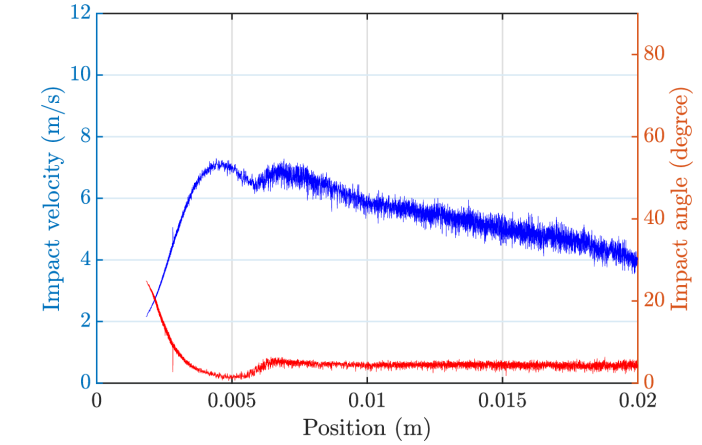

(b)

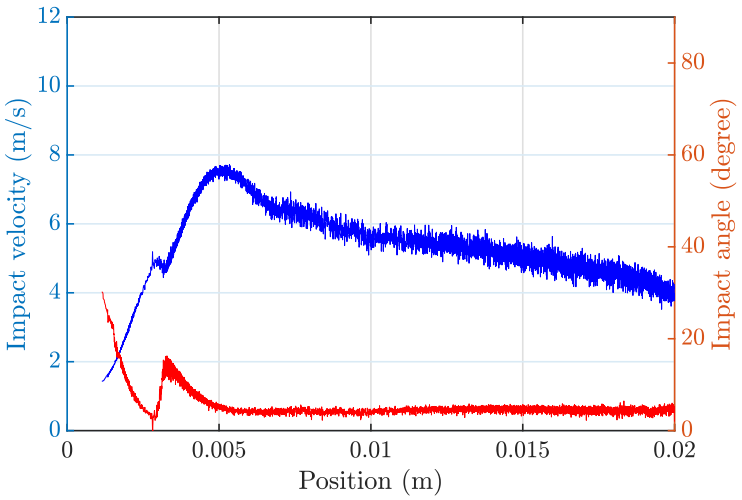

(c)

Fig. 4.12 Particle impact velocity and impact angle plot for SOD=2D (a) Without acoustics (b) 610 kHz (c) 850 kHz

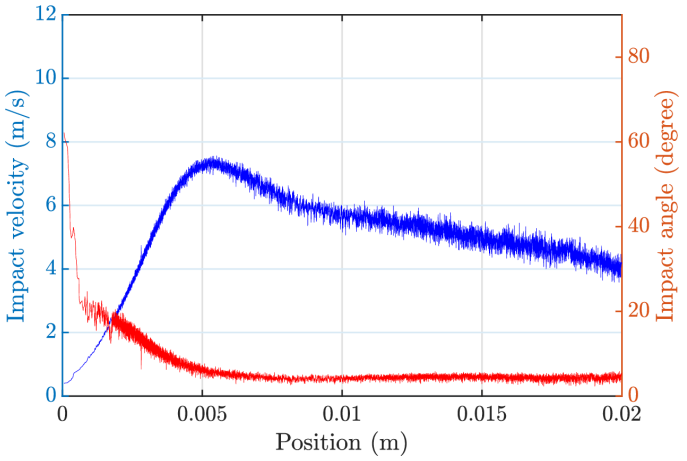

(a)

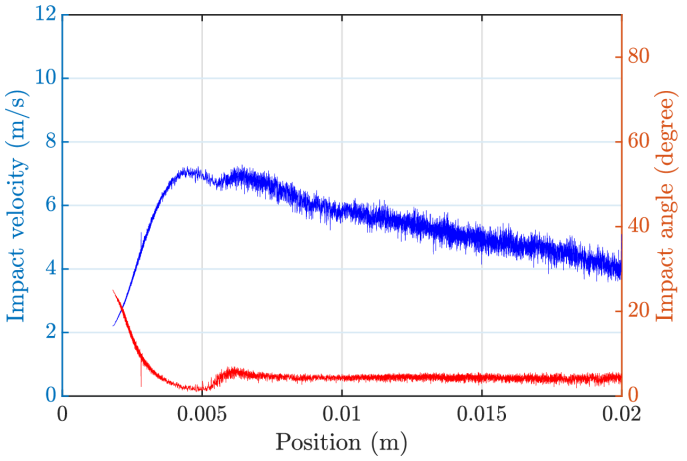

(b)

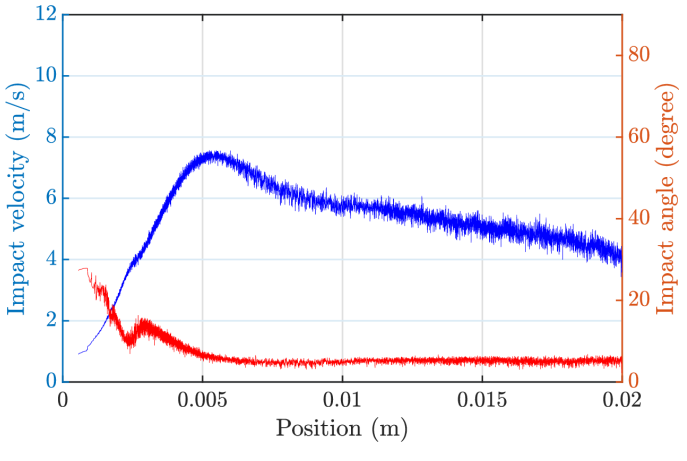

(c)

Fig. 4.13 Particle impact velocity and impact angle plot for SOD=4D (a) Without acoustics (b) 610 kHz (c) 850 kHz

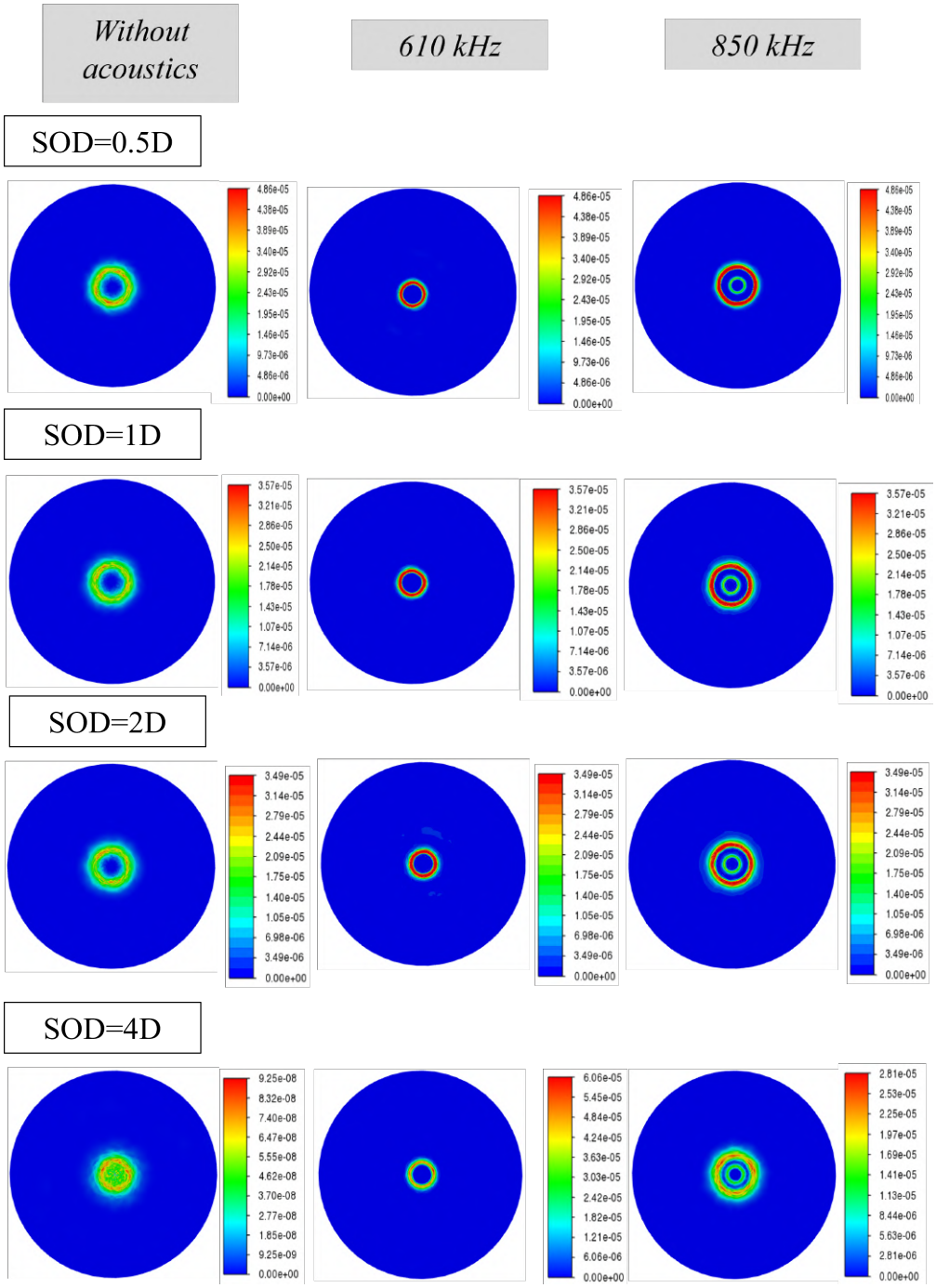

Fig. 4.14 Erosion rate per unit area (kg/m^2s) on the target surface obtained by the Oka Model for various SODs and acoustic frequencies

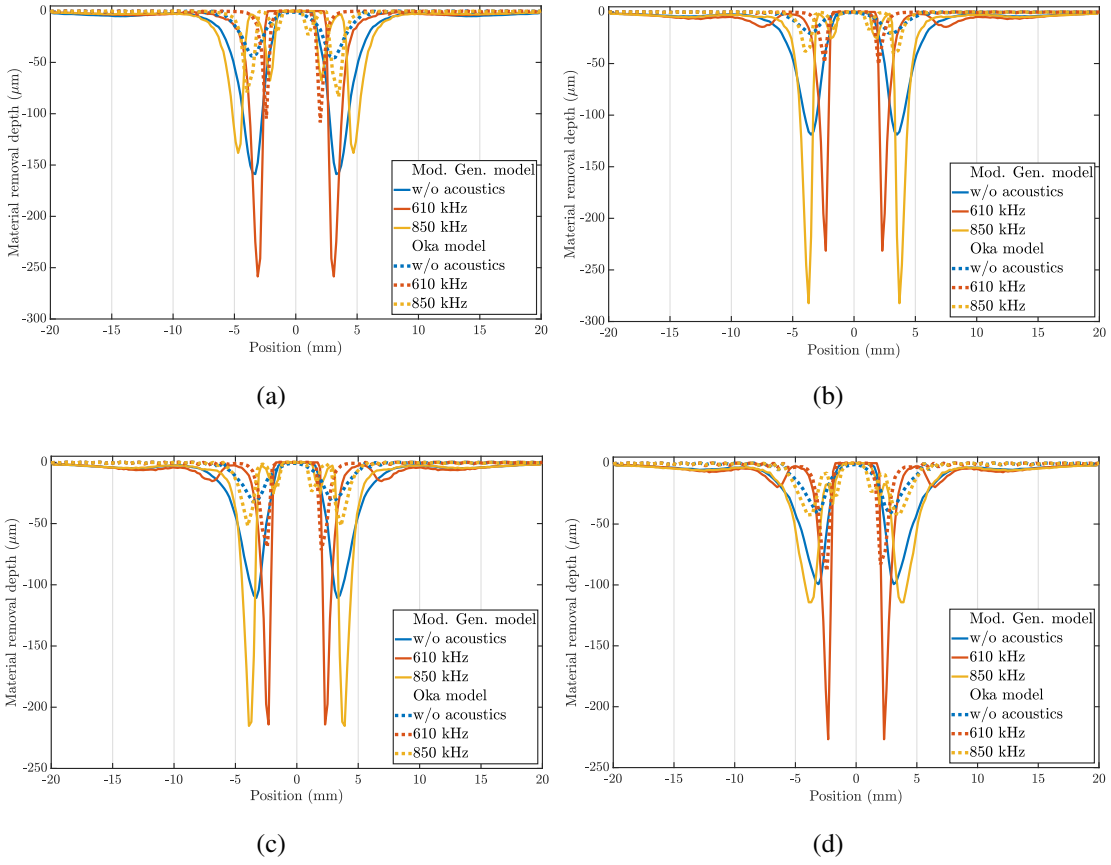

Fig. 4.15 Erosion profile comparison between conventional FJP and FJP with radial acoustic forcing with different frequencies for two erosion models: (a) SOD=0.5D (b) SOD=1D (c)SOD=2D (d)SOD=4D

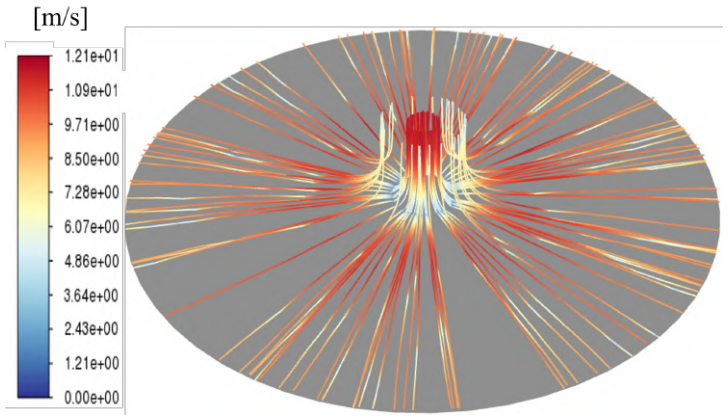

(a)

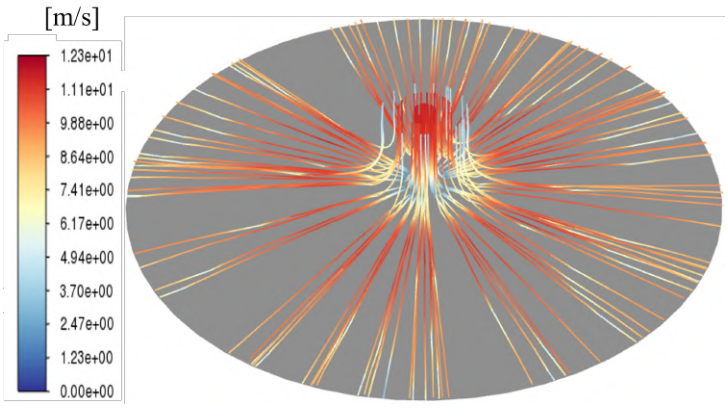

(b)

Fig. 4.16 Particle trajectories approaching the target surface for acoustic excitation of (a)610 kHz (b)850 kHz

kHz. It can be observed from Figs. 4.14 and 4.15 that the increase in *SOD* reduces the erosion magnitudes. This can be corroborated from the axial velocity plots in Fig. 4.7 where a reduction in axial velocity is observed till the *SOD* of four. As mentioned before, the higher *SOD* scenarios have not been considered here as the turbulent dispersion redistributes the particles away from their acoustically focused locations in the free jet and stagnation zones. Hence, with the acoustophoretic-assisted FJP in circular nozzles, one can achieve precise annular erosions as long as the surface stand-off distance is maintained small.

Comparing Figs. 4.8 and 4.9, one may observe that the number of rings corresponding to the particles' impact is one less than the number arrived with simple 2D force calculations. This difference can be explained using Fig.4.16 where the number of particles settling to the outermost ring is less, and they get easily carried away by the flow streamlines, thereby just grazing the target surface without having significant impact or contribution to the erosion process.

4.5 Closure

Despite the notable annular erosion, the primary issue of inhomogeneous erosion still persists in the circular geometries. In fact, the erosion at the stagnation zone is still trivial, and the particles have been actively pushed away from it. This behaviour is understandable as the pressure nodes are concentric circles whose position depends on the zeroth-order Bessel function, which is non-zero at $r = 0$. Hence, under no circumstances can a pressure node be expected at the nozzle centre so that the particles can be migrated to the jet axis. Thus, achieving a U-shaped erosion profile in circular cross-sectioned nozzles for smaller *SOD*s is nearly impossible. In order to overcome this drawback, we now investigate such possibilities in non-circular geometries such as rectangles. In the next chapter, we perform detailed simulations of acoustophoretic particle excitation in jets issued from square cross-sectioned nozzles.

Chapter 5

Acoustophoretic FJP using a square jet

5.1 Chapter Overview

This chapter aims to understand the influence of the acoustophoretic effect on a nozzle with a square cross-section. The essential idea is to focus particles along the jet centreline and, thereby, manifest a U-shaped erosion profile.

5.2 Geometry and boundary conditions

The basic framework of the square jet simulations, including the boundary and particle injection conditions, remains the same as that of the circular jets. As shown in Fig. 5.1(a), the geometry consists of a square cross-sectional nozzle and a target surface kept at the standoff distance, *SOD*. The corresponding mesh is shown in Fig. 5.1(b). The operating parameters utilised for the simulations are presented in Table 5.1.

Similar to Fig. 4.8, a simple, isolated Lagrangian force balance on the particles shown in Fig. 3.8 using Eq. (3.59) & (3.60) reveals their final equilibrium locations. In situations where a one-dimensional acoustic forcing is applied within the nozzle along the x-direction, the particles get concentrated on the mid-x plane. The same behaviour can be expected if the forcing is in the y-direction. Thus, we consider a composite forcing involving the x and y directions to focus the particles along the jet axis as in Fig. 3.8 & (3.7). The acoustic excitation frequency has been selected based on cross-sectional dimensions such that discrete half-wavelength standing waves are formed in both directions. For the present configuration specified in Table 5.1, the excitation frequency is around 148 kHz. In the following subsections, we will characterise the influence of different parameters, such as the

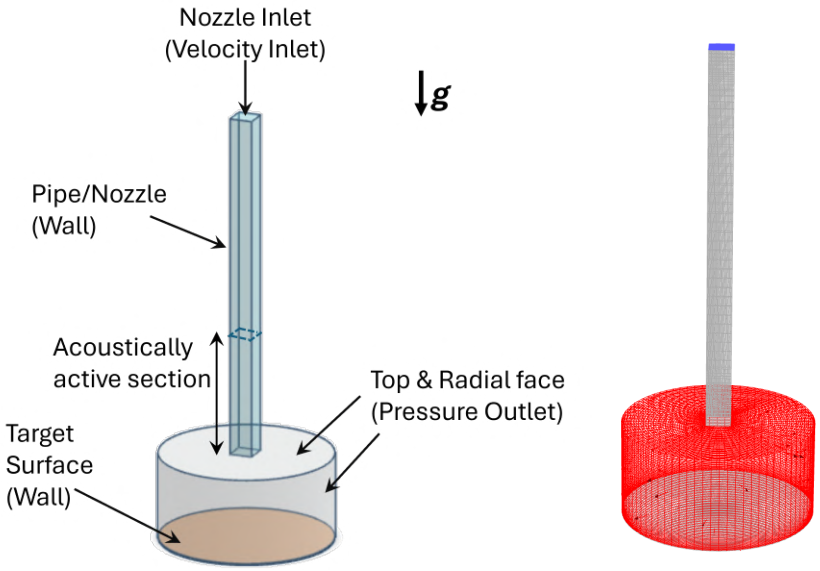

Fig. 5.1 (a)Geometry and boundary conditions of a square jet impingement (b)Mesh

Nozzle side	5 mm
Nozzle length	80 mm
Stand-off distance	2.5,5,10,20,30,40 mm
Target plate diameter	40 mm
Nozzle average velocity	10 m/s
Target material	Stainless Steel 316
Nominal particle size	60 μm
Particle concentration (by mass)	1%
Particle density	2650 kg/m^3
Angle of incidence	90^o
Test duration	6 hrs

Table 5.1 Operating parameters used in the present numerical work for acoustophoretic square FJP

standoff distance, the amplitude, the length, and the location of the acoustically active region on the particle impact locations and the resulting erosion process.

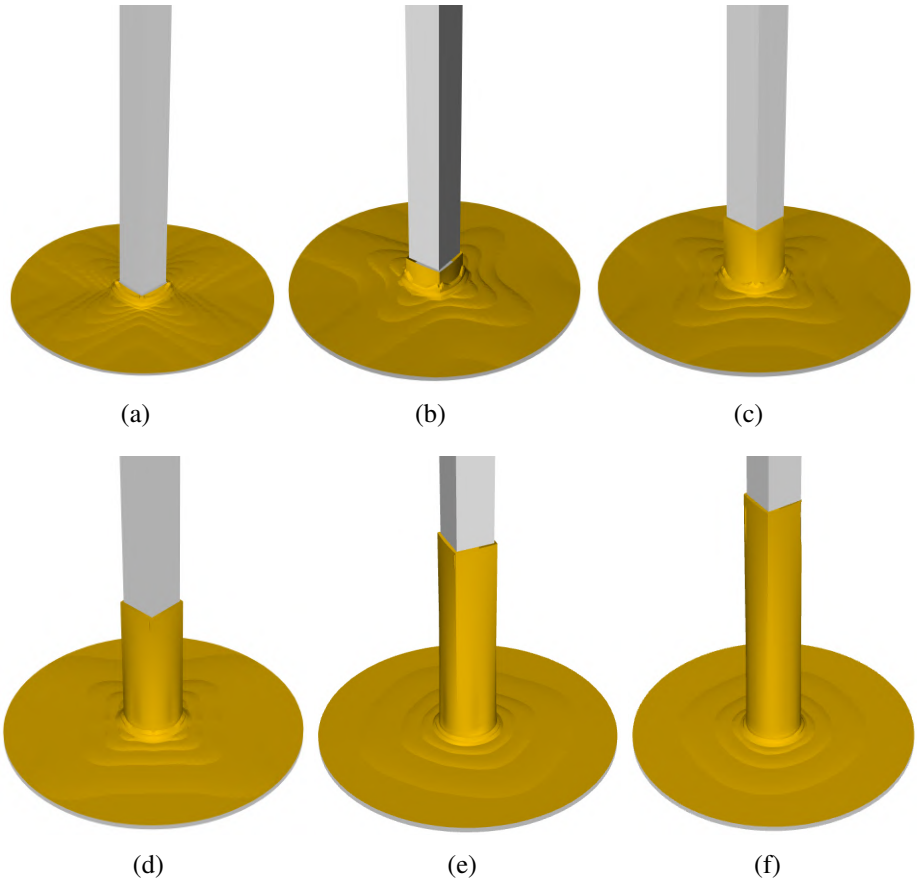

Fig. 5.2 Interface of square impinging jets at different SODs: (a) 0.5D, (b) D, (c) 2D, (d) 4D, (e) 6D, and (f) 8D.

5.3 Results and Discussion

5.3.1 Variation of Stand-off Distance (*SOD*)

Similar to the case of circular cross-sections, the standoff distance between the nozzle exit and the target surface plays a significant role here in deciding the erosion profile on the surface. To understand it better, we now consider six different values of *SOD*s viz. 0.5D, 1D, 2D, 4D, 6D, and 8D, where $D = 5mm$ is the side length of the square nozzle. Once again, the last 30 mm of the nozzle length is considered to be the acoustically active region. The optimality of such a consideration is analysed in the following subsections. Figure 5.2 shows

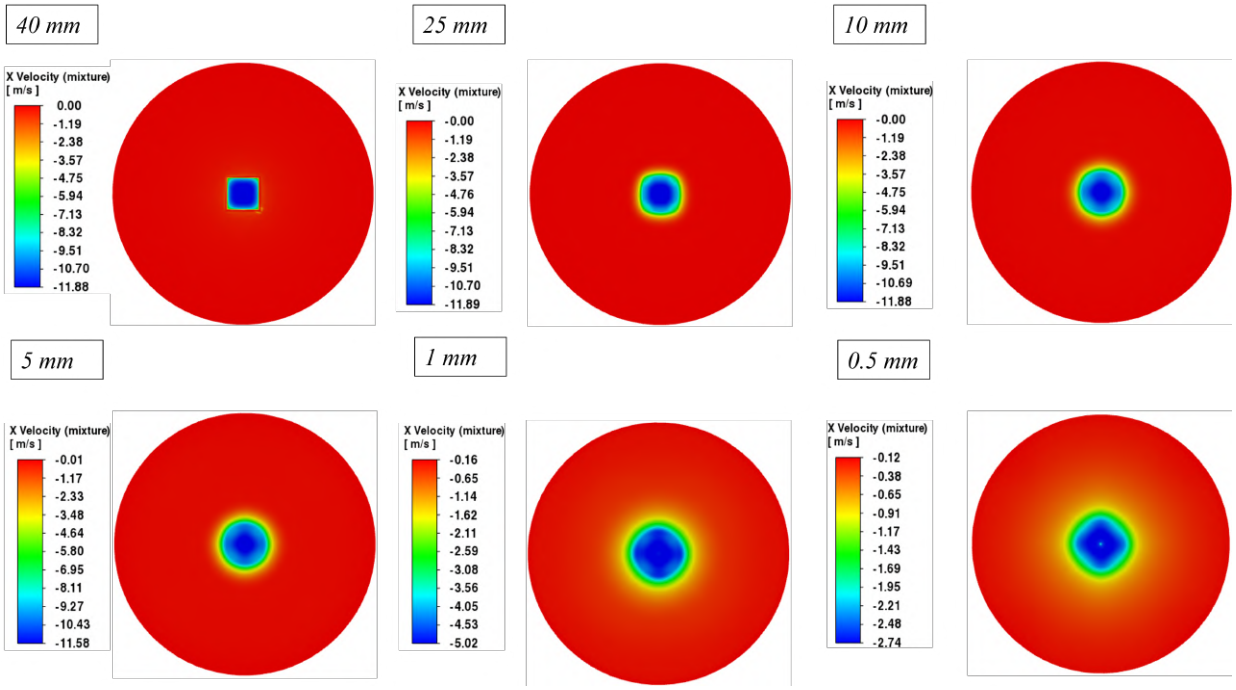

Fig. 5.3 Axial velocity contour of SOD=8D case at different distances from the target surface

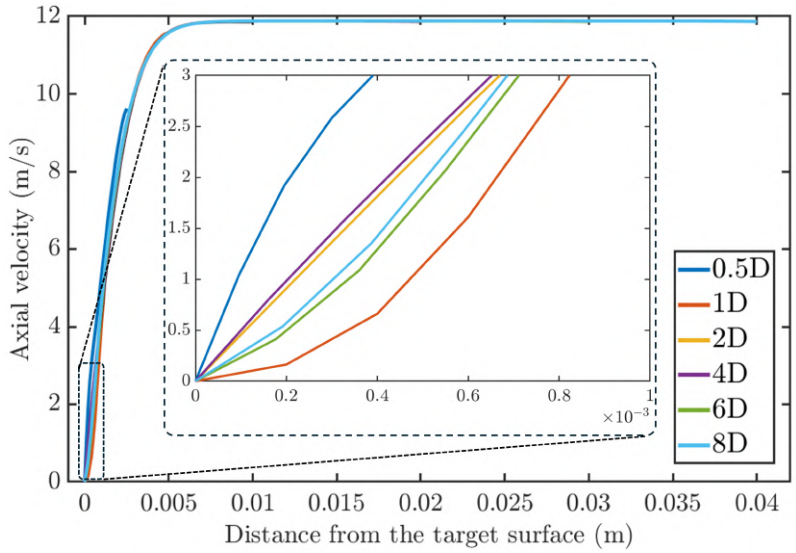

Fig. 5.4 Centreline axial velocity for different SODs

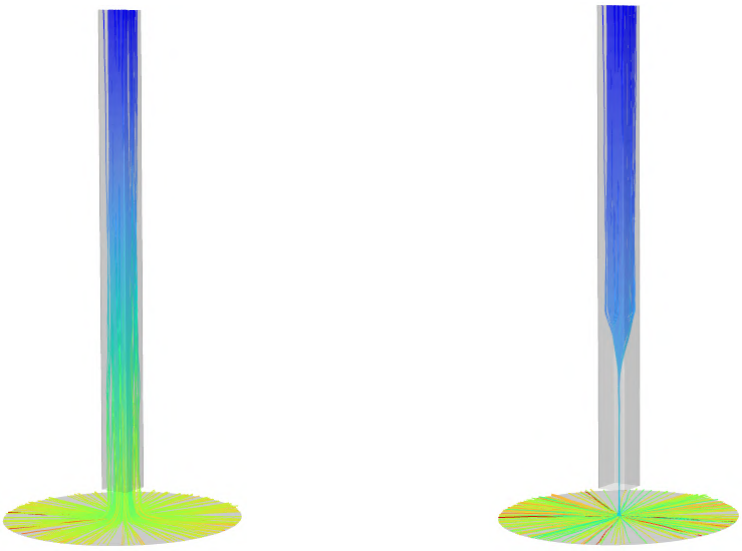

(a) (b)

Fig. 5.5 (a)Particle tracks without acoustics (b)Particle tracks with rectangular acoustic forcing

the corresponding interfacial profiles where a notable transition of the jet profile from the square cross-section is evident at higher *SOD*s. Despite the profile change, the simulations do not show any manifestation of jet instability even at the *SOD* of $8D$. Unlike the circular case, there is a persistent surface undulation even at the largest *SOD*. The reason for this behaviour can be understood from Fig. 5.3 wherein the sectional velocity profiles are shown at different horizontal planes above the target surface. There is a notable non-uniformity in the cross-sectional velocity profile, though the outer form of the jet seems to transition initially to a circular shape. The four-pronged hub profile within the liquid jet brings in its own dynamics and particle distribution patterns, which are very different from those of circular jets. The axial velocity profile resembles the shape of a rhombus closer to the impact surface. A quick comparison of the axial velocity profiles of the square jets, as in Fig. 5.4, and the circular jets, as in Fig. 4.7, reveals a notable change in the flow patterns. In the circular jet case, the approach velocity was found to gradually decrease till the *SOD* of $4D$ and increase thereafter. However, in the present square case, the axial velocity closer to the target surface has a unique pattern wherein the velocity for the $SOD = 1D$ case drops drastically as compared to the $SOD = 0.5D$ scenario. The values again increase for $SOD = 2D$ case before dropping again for higher *SOD*s. While the exact reasons for such peculiar behaviour require further exploration that is beyond the scope of the present work, it is likely related to the liquid jet shape transition, as observed in Fig.5.2. Notwithstanding such distinctive behaviour,

we now focus on understanding the influence of acoustophoresis in particle migration for each of the SODs considered.

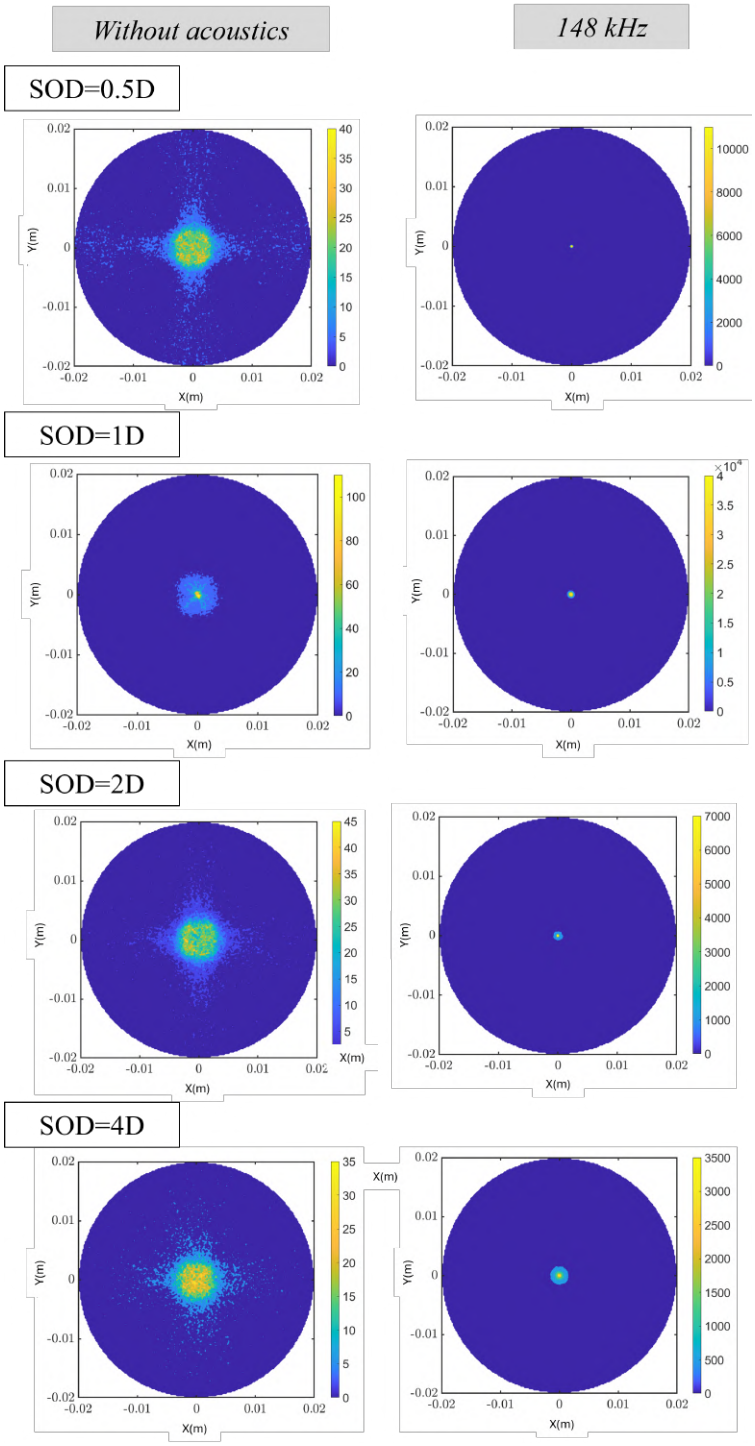

Fig. 5.6 Number density of particle impacting on the target surface for various SODs with and without acoustics

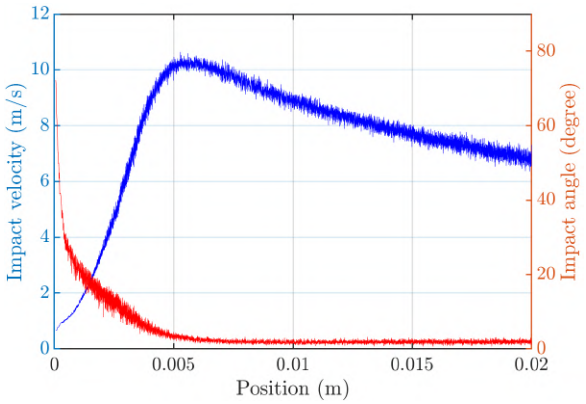

(a)

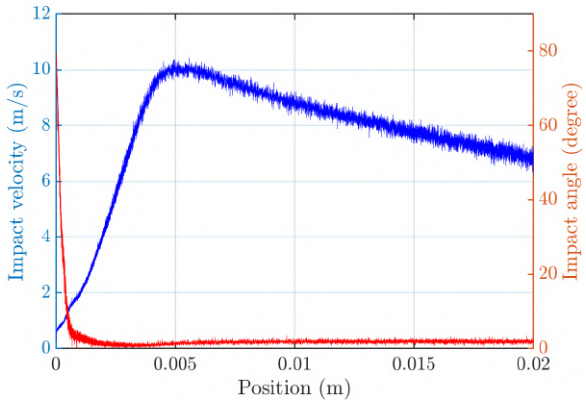

(b)

Fig. 5.7 Particle impact velocity and impact angle plot for SOD=0.5D (a) Without acoustics (b) 148 kHz

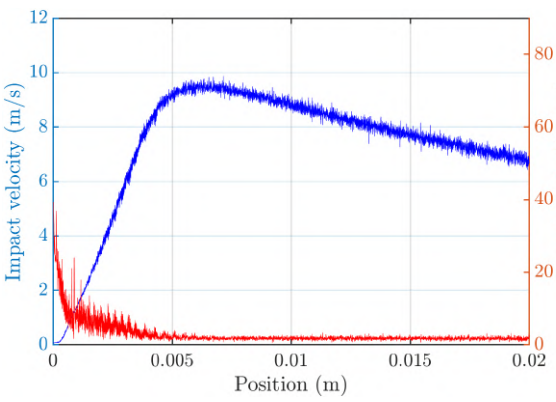

(a)

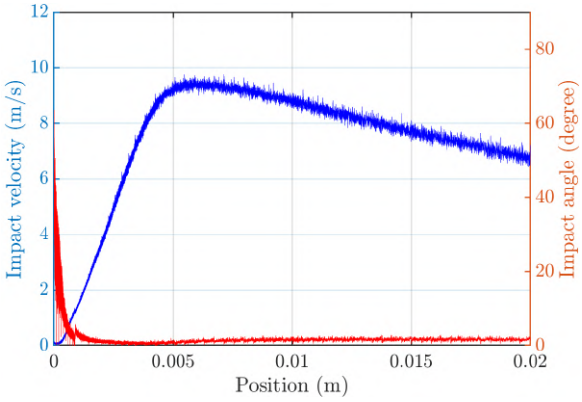

(b)

Fig. 5.8 Particle impact velocity and impact angle plot for SOD=1D (a) Without acoustics (b) 148 kHz

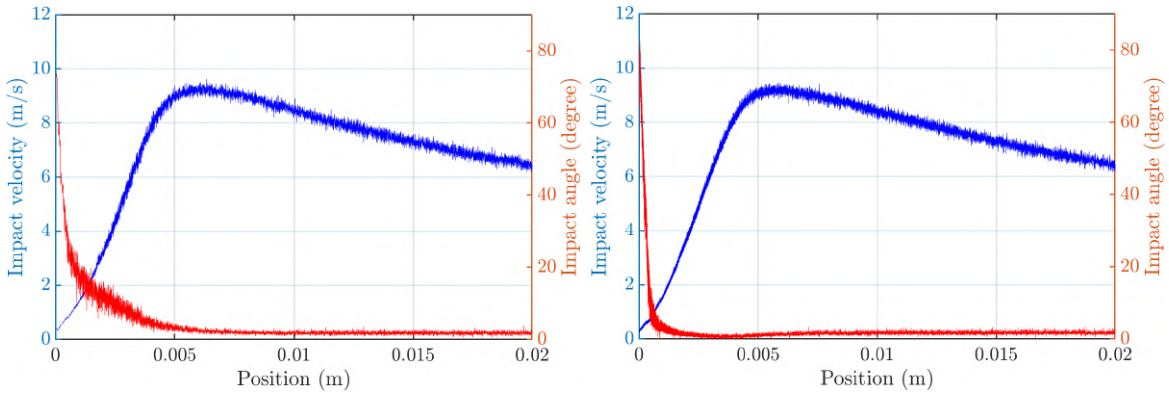

(a) (b)

Fig. 5.9 Particle impact velocity and impact angle plot for SOD=2D (a) Without acoustics (b) 148 kHz

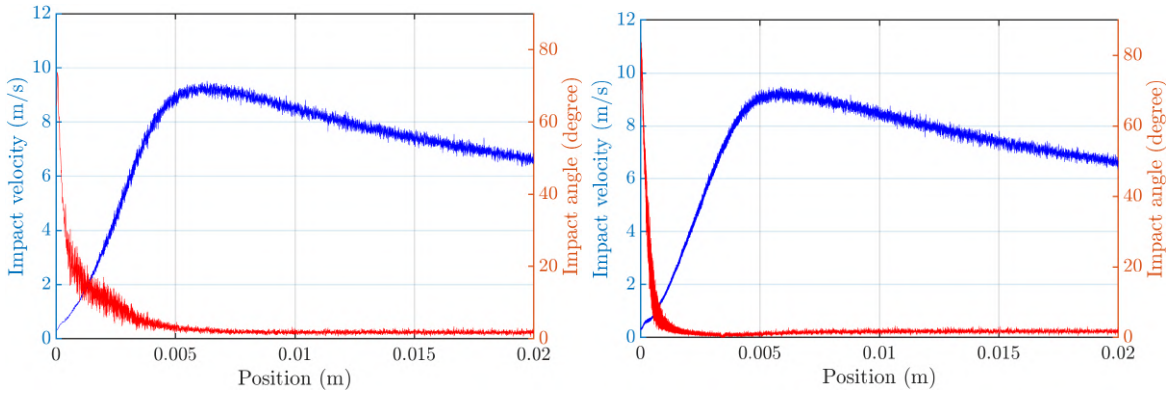

(a) (b)

Fig. 5.10 Particle impact velocity and impact angle plot for SOD=4D (a) Without acoustics (b) 148 kHz

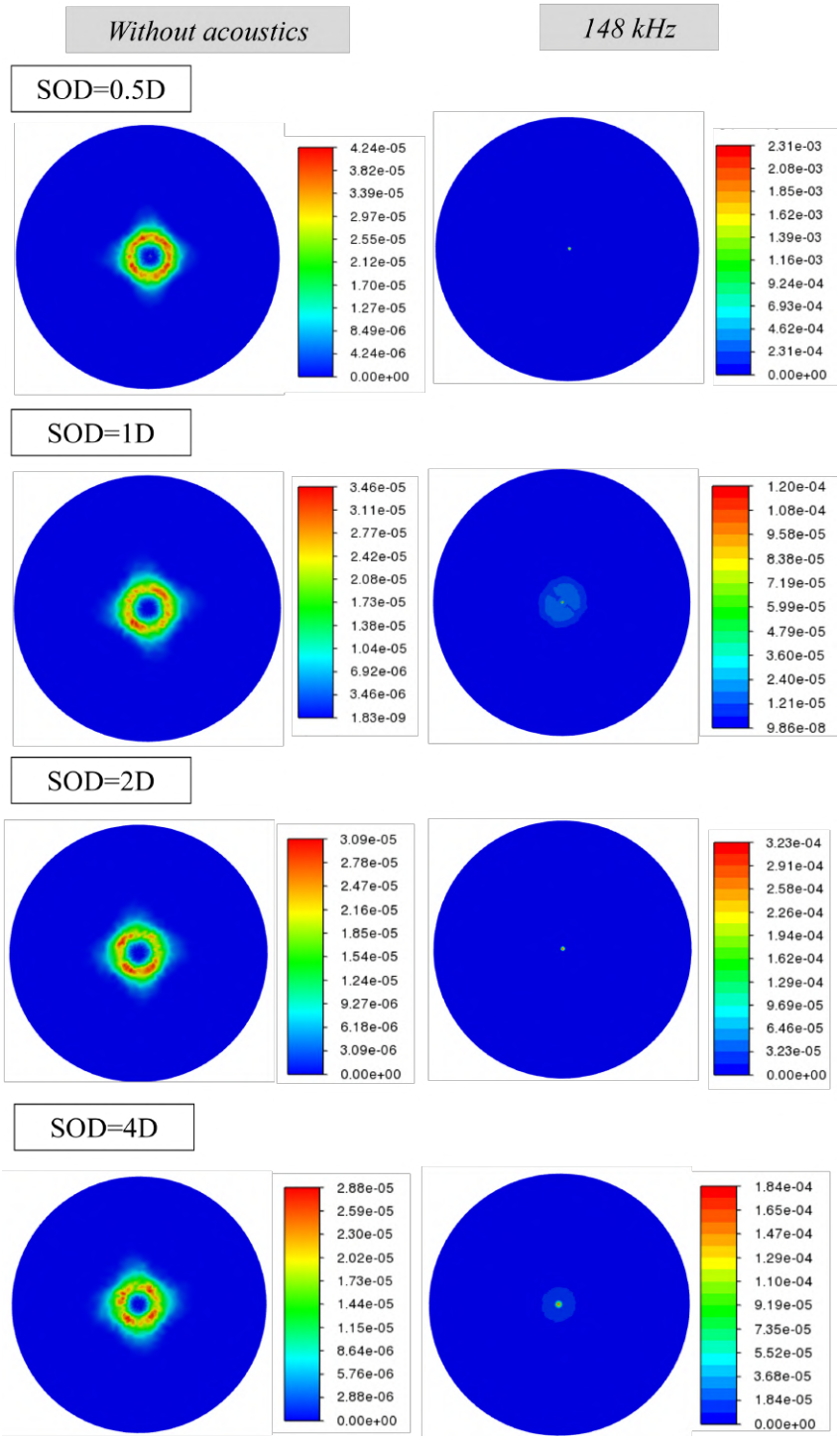

Fig. 5.11 Erosion rate (kg/m^2s) as per Oka Model on the target surface for various SODs with and without acoustics

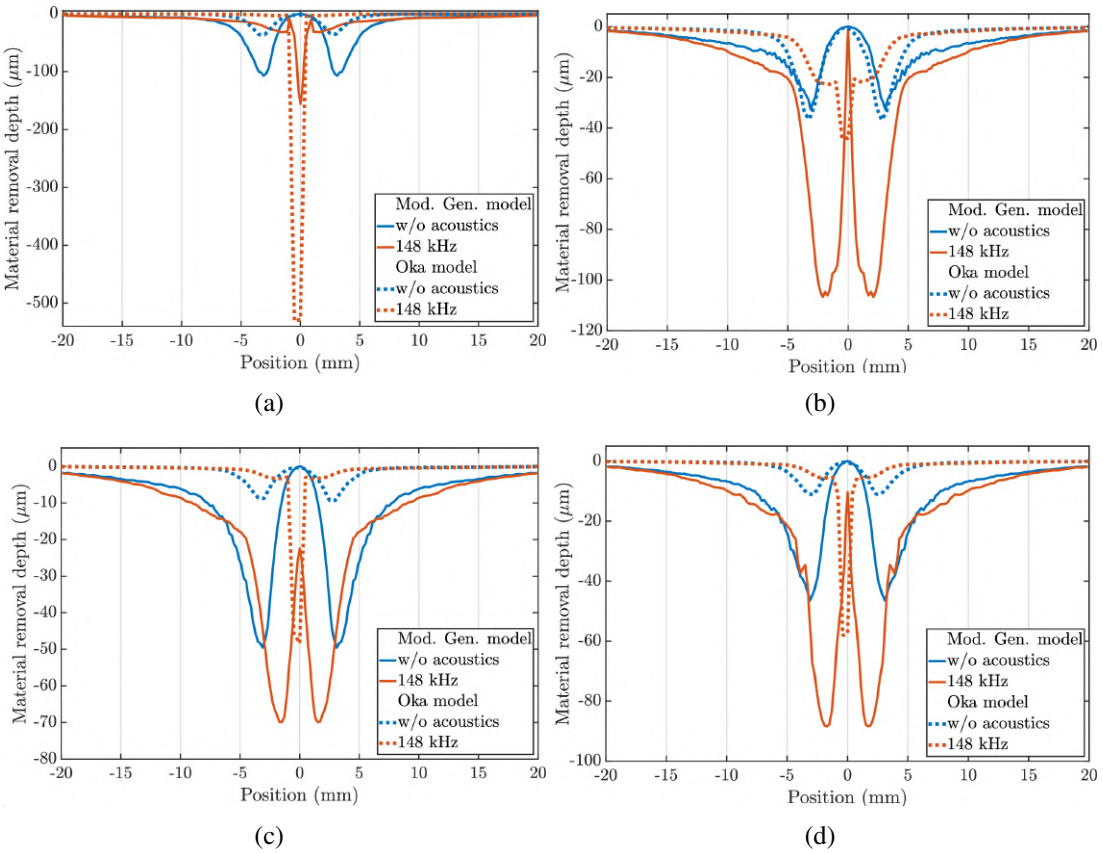

Fig. 5.12 Erosion profile comparison for square FJP with and without acoustics for two erosion models: (a) SOD=0.5D (b) SOD=1D (c)SOD=2D (d)SOD=4D

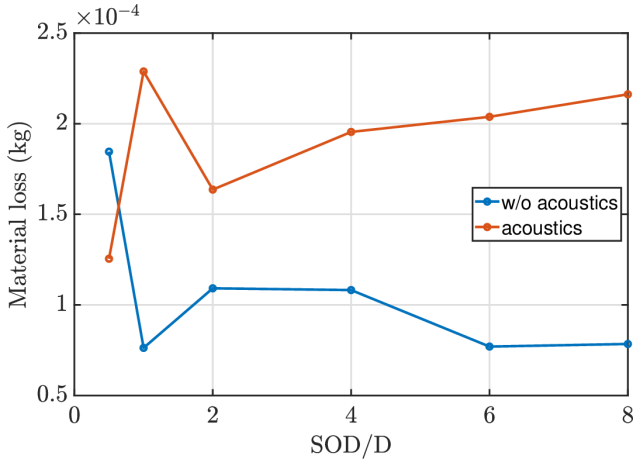

Fig. 5.13 Material loss comparison at different SODs (with and without acoustics) obtained using the modified Generalised model

Figure 5.5 compares the particle trajectories obtained with and without the acoustic excitation for a sample *SOD* of 1*D*. A clear migration of particles towards the jet axis and their subsequent targeted impingement on the surface is evident in the figure. In fact, this behaviour is consistent for all the *SOD*s as shown in Fig. 5.6, which shows the distribution of particle impact density on the target surface. The widely distributed region for the case without acoustic excitation is now focused on a point strictly at the centre of the surface. One may observe that the range of legend in the acoustic case is orders of magnitude higher than the unexcited scenario. The peculiarity mentioned in the previous paragraph regarding the axial velocities at different *SOD*s also has its signature in the number density plot. When there is no additional acoustic excitation, the wide region of impact observed for the $SOD = 0.5D$ case becomes less pronounced for the SOD=$1D$. Here, the reduction in the axial velocity of the particles allows for them to be carried away by streamlines without significantly impacting the target surface. With the increase of axial velocities for higher *SOD*s, the particle impact scenario improves once again. For the cases with the imposed acoustic excitation, the singular impact point becomes visibly larger with the increase of *SOD* as the particles are spread out before impact due to turbulent dispersion.

The above particle impact density pattern has a direct influence on the erosion process, as evident in the erosion contours obtained from the Oka model in Fig. 5.11. The case without any acoustic excitation is characterised by a non-uniform annular erosion that essentially avoids the stagnation point and its vicinity. However, with acoustic excitation, the erosion is focused at the stagnation point, a feat normally challenging to achieve by any other modifications of the FJP process. The erosion depth data presented for both the Oka and the modified generalised erosion models in Fig. 5.12 corroborates these features. Though the magnitude of erosion is different for these models, the corresponding erosion profiles are relatable when there is no acoustic excitation. However, one can observe a notable difference in the profiles when the acoustic excitation is active. Though both the models manifest a U-shaped erosion profile for the *SOD* of 0.5*D*, their manifestation is different for the higher *SOD*s. While the modified generalised erosion model shows a W-shaped profile, the Oka model consistently shows a U-shaped profile. This disparity can be traced back to the manner of angular correction performed by these models as illustrated in Fig. 3.9. Only systematic experimentation may help bridge the gap between the two models.

Apart from the shape of the erosion profile, there is also a notable improvement in the quantity of material removal or the erosion depth. The erosion depths shown in Fig. 5.12 consistently demonstrate improved and focused material removal while using acoustic excitation. A surrogate measure for understanding the efficacy of material removal can be obtained by spatially integrating the data in Fig. 5.12 to arrive at the total material loss (in

kg). Figure 5.13 compares the material loss for the two scenarios (with and without acoustic excitation) using the modified generalised model, which yields a more conservative estimate. The above graph shows that the amount of material removal is generally well-enhanced by acoustophoretic intervention. However, for the case with $SOD = 0.5D$, a reduction in material loss is observed with acoustics excitation though the centre line depth is orders of magnitude higher. Despite this single point anomaly, acoustophoretic excitation improves the FJP process, both in terms of the material removal rate, as well as through the manifestation of a U-shaped erosion profile. Continuing further, we now analyse the influence of different acoustic parameters on the particle trajectories and erosion profiles obtained during square jet impingement.

5.3.2 Variation of acoustic amplitude

The first parameter considered in the present analysis is the amplitude of the input acoustic standing wave, Ψ_0, which is defined in section (3.3.2) as the ratio of the acoustic particle velocity, v_0, to the wavenumber. A constant value of $v_0 = 10 m/s$ has been used for all the simulations presented till now. We now characterise how the erosion patterns change with Ψ_0, i.e., v_0, for a specific SOD of $0.5D$. In this regard, the entire nozzle length has been chosen to be acoustically active. All the other relevant system and simulation parameters are maintained to be the same as in Table 5.1.

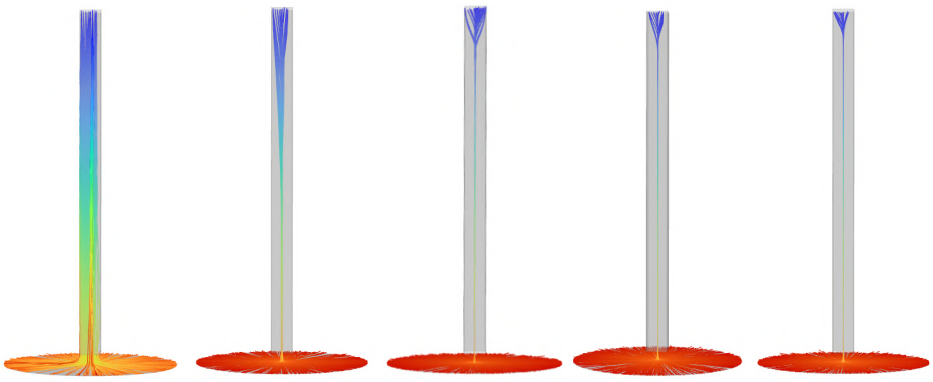

Fig. 5.14 Particle trajectories with acoustic amplitude (a)$0.1v_0$ (b)$0.5v_0$ (c)$1v_0$ (d)$1.5v_0$ (e)$2v_0$

Figure 5.14 shows the particle trajectories for five different v_0. Here, the larger the acoustic amplitude, the greater the acoustic radiation pressure acting on the particles, and hence, the quicker the migration of particles to the jet axis. Figure 5.15 shows the corresponding erosion depth data, which understandably increases with the amplitude. For lower

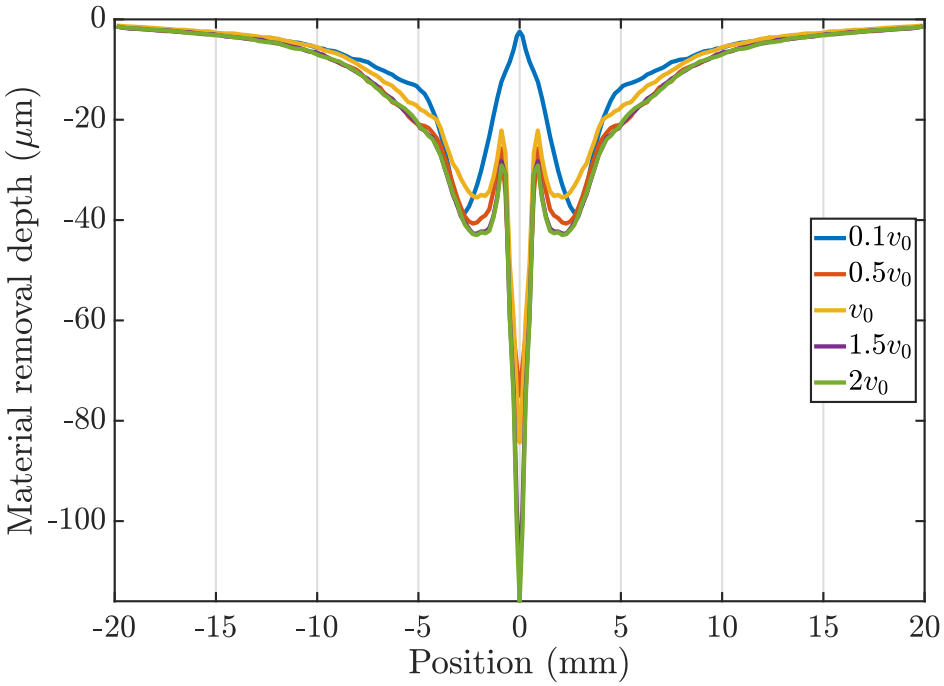

Fig. 5.15 Variation of acoustic amplitude

acoustic amplitudes, i.e., $v_0 < 5.0 m/s$, the erosion profile is the default W-shaped one due to insufficient forcing. However, beyond this range of v_0, the migration of particles to the centre line is complete, and the erosion profile becomes U-shaped. Considering the facts that the convergence of the particles does not change much beyond $v_0 = 10 m/s$ in Fig. 5.14 and the energy input requirements are higher at larger amplitudes, a nominal acoustic velocity of $10 m/s$ has been consistently utilised in the current work.

5.3.3 Variation in the length of acoustically active region

With the above selection of the acoustic amplitude, we now evaluate the minimum length of acoustic activation required within the nozzle so that the particles can be wholly migrated towards the jet axis. Note that this length would depend on both the amplitude of the acoustic excitation and the flow velocity within the nozzle. As shown in the previous sub-section, the larger the former quantity, the shorter the excitation length required for complete particle migration. At the same time, the latter quantity decides the residence time of the moving particles within the acoustic section. Hence, for the present consideration of acoustic velocity, v_0, being $10 m/s$ and average flow velocity of $10 m/s$, we now estimate the minimum length required for effectuating the complete particle migration.

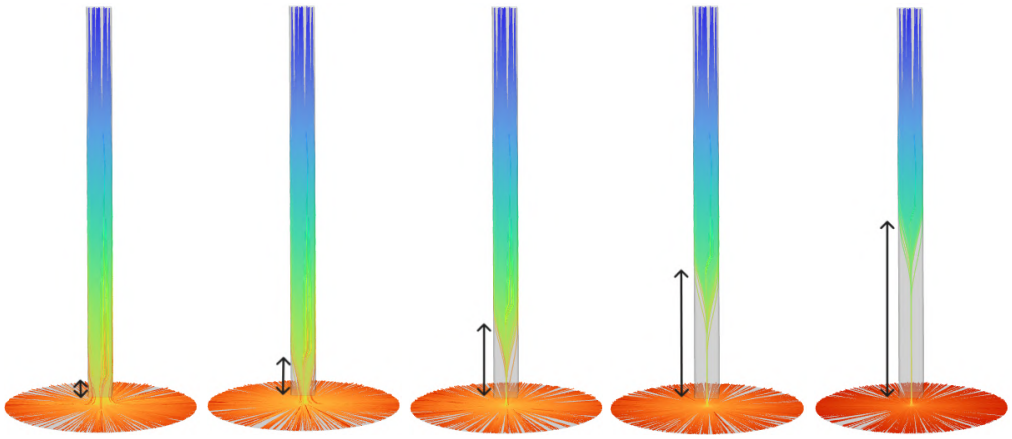

Fig. 5.16 Particle trajectories for different acoustically active lengths: (a) 5mm (b) 10mm (c) 20mm (d) 30mm (e) 40mm

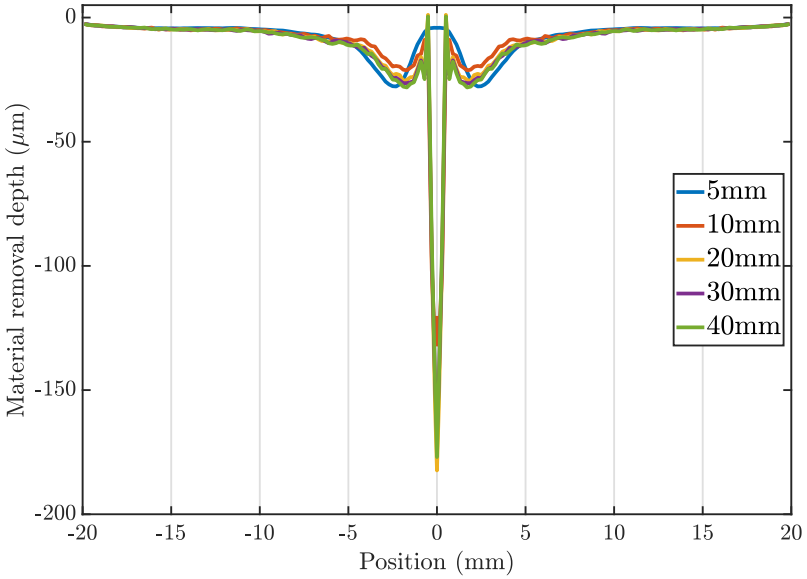

Fig. 5.17 Erosion depth comparison for different acoustically active lengths

Figure 5.16 shows the particle trajectories for different acoustically active lengths wherein it is evident that the particle migration to the centre line is complete for acoustical lengths greater than $20mm$. This information can be corroborated by the erosion plots shown in Fig. 5.17. Thus, for the present velocity considerations mentioned above, $30mm$ has been chosen as the optimum length. Any larger length of acoustic activation might unnecessarily involve more number of transducers for excitation. It is worth re-emphasising that this optimum length will have to increase if the acoustic amplitude is decreased or the flow velocity is increased.

5.3.4 Location of acoustic activation

Finally, it is essential to determine the location or the region within the nozzle where the acoustical activation results in the best performance. In this regard, we now assess the particle migration and erosion profiles for acoustic excitation at three different regions within the nozzle, as shown in Fig. 5.18. The optimal values of acoustic velocity and excitation length obtained from the previous analyses have been used here.

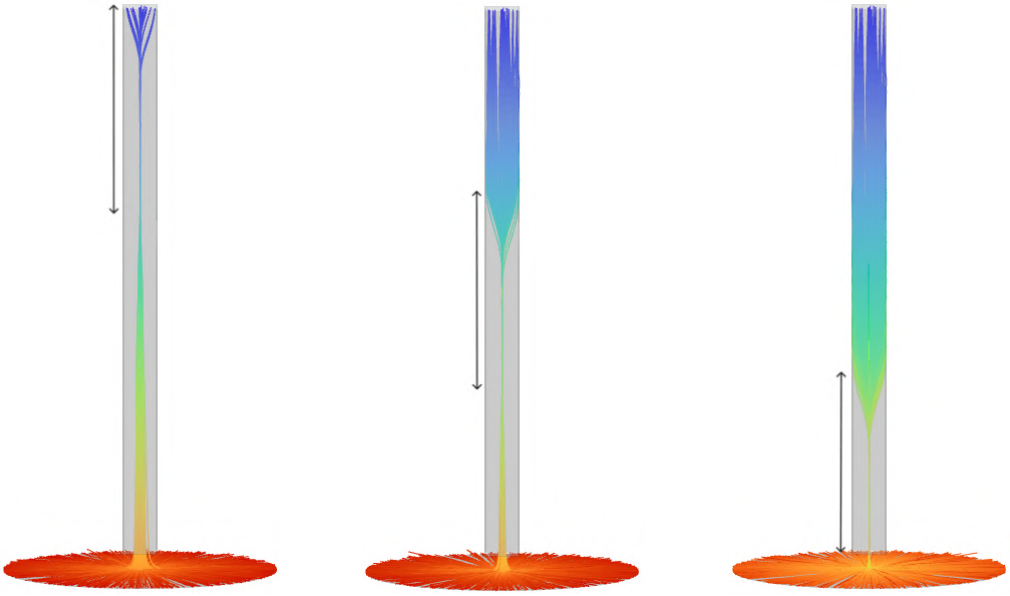

(a) (b) (c)

Fig. 5.18 Particle trajectories with acoustically active length (a) z=0.0525m to z=0.0825m (b) z=0.0275m to z=0.0575 m (c) z=0.0025m to z=0.0325m

Figure 5.18 shows the particle tracks for three different excitation scenarios within the nozzle. Once again, a SOD of $0.5D$ has been utilised for the comparison. Note that all the distances mentioned are with reference to the target surface, which is at $z = 0$. It is evident

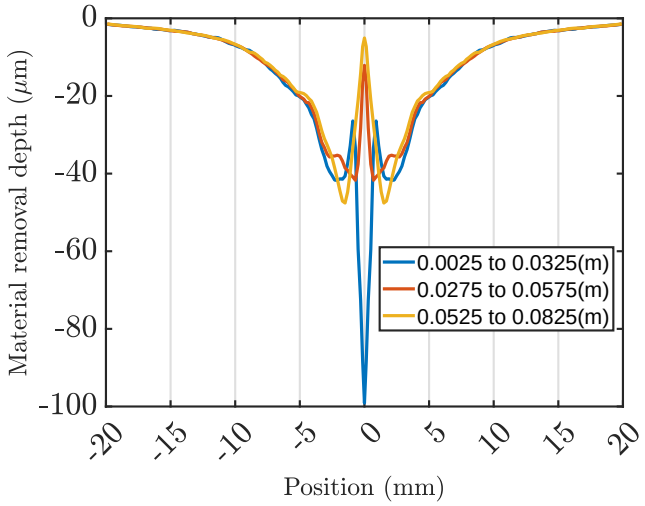

Fig. 5.19 Erosion profile comparison for different locations of the acoustically active section

from the figure that the turbulent dispersion in the unforced regions of the nozzle plays an important role in redistributing the particles downstream of the acoustically active region. Hence, it becomes essential to have the acoustical excitation closer to the nozzle exit, as it limits the effect of turbulent dispersion on the focused particles. Figure 5.19 substantiates this observation wherein a U-shaped erosion profile is markedly evident when the active section is between $z = 0.0025m$ and $z = 0.0325m$. Excitation at the other two locations results in W-shaped erosion profiles owing to the availability of sufficient downstream time wherein the particles are dispersed due to turbulence.

5.4 Closure

The analysis of rectangular acoustic forcing of appropriate frequency in particle-laden jets of square cross-sectional nozzles of different *SODs* reveals the desired particle migration effect. The particle impact density contours and the erosion depth plots clearly show a 'U' shaped erosion profile and improved material removal rate. Acoustic parametric studies such as variation of acoustic excitation amplitude, length of acoustically active region and location of acoustic activation have been presented to characterise the acoustophoretic square FJP further.

Chapter 6

Summary and Conclusions

The current work presents a proof-of-concept study of acoustophoretic-assisted fluid jet polishing. The technique involves migrating abrasive particles within the impinging jet using bulk acoustic waves. The underlying phenomenon has been analyzed using numerical simulations involving a combination of Eulerian and Lagrangian approaches that effectively mimic the multiphase, turbulent jet impingement and erosion process on the target surface. The added influence of acoustophoresis has been modeled via appropriate body force formulations. Using the above combination of procedures, the acoustophoretic FJP has been analyzed here for circular and square cross-sectioned nozzles. In the case of circular nozzles, acoustic excitation results in precise and controllable annular erosions. Here, the particles are focused on concentric pressure nodes that do not occur at the axis of the impinging jet, making the inhomogeneity of the erosion process inevitable. On the other hand, composite one-dimensional acoustic excitations in square cross-sections enable the focusing of particles along the jet axis. This results in U-shaped erosion profiles for specific operating conditions that have been estimated here using detailed parametric analysis. The precise focusing of the particles increases their effective utilization by further enabling their interaction with the target surface and, correspondingly, improving the material removal rate. Drifting particles away from the nozzle walls controls their unintended erosion, making the process repeatable and cost-effective. The improved material removal rate, along with the possibility of focused erosion, makes the proposed FJP technique capable of handling ultra-precise machining requirements, including pattern formation. The current work, though involving limited numerical simulations, demonstrates all the above capabilities sufficiently. Understandably, the realization of these findings in common applications is bound to be accompanied by translational challenges, including the design of PZT-embedded nozzles that can establish proper standing waves perpendicular to the flow.

6.1 Scope for Future extension

1. The present work uses the theoretically available acoustophoretic force as a supplementary body force in DPM calculations. A more holistic way of approaching the problem would be to model a piezoelectric layer encompassing the water-filled tube. There, the sinusoidal deformation of the piezo material creates a pressure field inside the tube which acts on the suspended particles subsequently.

2. A dynamic meshing technique for the target surface that deforms progressively with erosion due to particle impacts can be employed for highly accurate flow structures.

3. In addition to this, experimental attempts have to be undertaken on particle-laden flow with acoustophoresis to understand its effects in macro-scales.

References

[1] ANAND, KSKH, HOVIS, SK, CONRAD, H & SCATTERGOOD, RO 1987 Flux effects in solid particle erosion. *Wear* **118** (2), 243–257.

[2] ANDRADE, MARCO AB, PÉREZ, NICOLÁS & ADAMOWSKI, JULIO C 2018 Review of progress in acoustic levitation. *Brazilian Journal of Physics* **48**, 190–213.

[3] BARMATZ, M & COLLAS, P 1985 Acoustic radiation potential on a sphere in plane, cylindrical, and spherical standing wave fields. *The Journal of the Acoustical Society of America* **77** (3), 928–945.

[4] BARNES, ROSEMARY ANN, JENKINS, P & COAKLEY, WILLIAM TERENCE 1998 Preliminary clinical evaluation of meningococcal disease and bacterial meningitis by ultrasonic enhancement. *Archives of disease in childhood* **78** (1), 58–60.

[5] BEAUCAMP, ANTHONY, KATSUURA, TOMOYA & KAWARA, ZENSAKU 2017 A novel ultrasonic cavitation assisted fluid jet polishing system. *CIRP Annals - Manufacturing Technology* **66**.

[6] BEAUCAMP, ANTHONY & NAMBA, YOSHIHARU 2013 Super-smooth finishing of diamond turned hard x-ray molding dies by combined fluid jet and bonnet polishing. *CIRP annals* **62** (1), 315–318.

[7] BELLMAN JR, ROBERT & LEVY, ALAN 1981 Erosion mechanism in ductile metals. *Wear* **70** (1), 1–27.

[8] BITTER, JGA 1963 A study of erosion phenomena part i. *wear* **6** (1), 5–21.

[9] BJERKNES, VFK, DIE, KRAFIFELDER & OTHERS 1909 Braunschweig .

[10] BÖHM, H, ANTHONY, P, DAVEY, MR, BRIARTY, LG, POWER, JB, LOWE, KC, BENES, E & GRÖSCHL, M 2000 Viability of plant cell suspensions exposed to homogeneous ultrasonic fields of different energy density and wave type. *Ultrasonics* **38** (1-8), 629–632.

[11] BOOIJ, SILVIA M, VAN BRUG, HEDSER, BRAAT, JOSEPH JM & FA¨ HNLE, OLIVER W 2002 Nanometer deep shaping with fluid jet polishing. *Optical engineering* **41** (8), 1926–1931.

[12] BRACKBILL, JEREMIAH U, KOTHE, DOUGLAS B & ZEMACH, CHARLES 1992 A continuum method for modeling surface tension. *Journal of computational physics* **100** (2), 335–354.

[13] BRUUS, HENRIK 2012 Acoustofluidics 7: The acoustic radiation force on small particles. *Lab on a Chip* **12** (6), 1014–1021.

[14] CAO, ZHONG-CHEN, CHEUNG, CHI FAI & REN, MINGJUN 2016 Modelling and characterization of surface generation in fluid jet polishing. *Precision Engineering* **43**, 406–417.

[15] ÇETIN, BARBAROS & LI, DONGQING 2011 Dielectrophoresis in microfluidics technology. *Electrophoresis* **32** (18), 2410–2427.

[16] CLEMENT-SENGEWALD, ANNETTE, SCHÜTZE, KARIN, ASHKIN, ARTHUR, PALMA, GUSTAVO A, KERLEN, GERTRUDE & BREM, GOTTFRIED 1996 Fertilization of bovine oocytes induced solely with combined laser microbeam and optical tweezers. *Journal of assisted reproduction and genetics* **13**, 259–265.

[17] COUSINS, CM, HOLOWNIA, P, HAWKES, JJ, LIMAYE, MS, PRICE, CP, KEAY, PJ & COAKLEY, WT 2000 Plasma preparation from whole blood using ultrasound. *Ultrasound in medicine & biology* **26** (5), 881–888.

[18] CROCKETT, ALLEN & RUECKNER, WOLFGANG 2018 Visualizing sound waves with schlieren optics. *American Journal of Physics* **86** (11), 870–876.

[19] CRUM, LAWRENCE A 1971 Acoustic force on a liquid droplet in an acoustic stationary wave. *The Journal of the Acoustical Society of America* **50** (1B), 157–163.

[20] DOBLHOFF-DIER, O, GAIDA, TH, KATINGER, H, BURGER, W, GROSCHL, M & BENES, E 1994 A novel ultrasonic resonance field device for the retention of animal cells. *Biotechnology progress* **10** (4), 428–432.

[21] DU, JIONG-RONG, JUANG, YI-JE, WU, JIE-TANG & WEI, HSIEN-HUNG 2008 Long-range and superfast trapping of dna molecules in an ac electrokinetic funnel. *Biomicrofluidics* **2** (4).

[22] ECKART, CARL 1948 Vortices and streams caused by sound waves. *Physical review* **73** (1), 68.

[23] FÄHNLE, OLIVER W, VAN BRUG, HEDSER & FRANKENA, HANS J 1998 Fluid jet polishing of optical surfaces. *Applied optics* **37** (28), 6771–6773.

[24] FANG, HUI, GUO, PEIJI & YU, JINGCHI 2006 Surface roughness and material removal in fluid jet polishing. *Applied optics* **45** (17), 4012–4019.

[25] FANG, QING-TING, LI, ZE-YOU, YU, QI-PAN, ZOU, CAO-YI, LI, SI-QING & LUO, DUAN-BIN 2021 Visualization of ultrasonic wave fields and demonstration of sound wave property in undergraduate physics experiment. *Physics Education* **56** (6), 065016.

[26] FINNIE, IAIN 1960 Erosion of surfaces by solid particles. *wear* **3** (2), 87–103.

[27] FINNIE, IAIN 1972 Some observations on the erosion of ductile metals. *wear* **19** (1), 81–90.

[28] FINNIE, IAIN 1995 Some reflections on the past and future of erosion. *Wear* **186**, 1–10.

[29] FITZGERALD, JANICE A. & GARIMELLA, SURESH V. 1998 A study of the flow field of a confined and submerged impinging jet. *International Journal of Heat and Mass Transfer* **41**, 1025–1034.

[30] FOLDYNA, JOSEF, SITEK, LIBOR, SVEHLA, BRANISLAV & SVEHLA, STEFAN 2004 Utilization of ultrasound to enhance high-speed water jet effects. *Ultrasonics sonochemistry* **11**, 131–7.

[31] FROSELL, T, FRIPP, M & GUTMARK, E 2015 Investigation of slurry concentration effects on solid particle erosion rate for an impinging jet. *Wear* **342**, 33–43.

[32] GOR'KOV, L. P. 1961 Forces acting on a small particle in an acoustic field within an ideal fluid. *Dokl. Akad. Nauk SSSR* .

[33] GRANT, G. & TABAKOFF, WIDEN 1975 Erosion prediction in turbomachinery resulting from environmental solid particles. *Journal of Aircraft* **12**, 471–478.

[34] GUCK, JOCHEN, ANANTHAKRISHNAN, REVATHI, MAHMOOD, HAMID, MOON, TESS J, CUNNINGHAM, C CASEY & KÄS, JOSEF 2001 The optical stretcher: a novel laser tool to micromanipulate cells. *Biophysical journal* **81** (2), 767–784.

[35] HAIDER, A. 1989 Drag coefficient and terminal velocity of spherical and non-spherical particles. *Powder Technology - POWDER TECHNOL* **58**, 63–70.

[36] HAUGEN, K, KVERNVOLD, O, RONOLD, A & SANDBERG, R_ 1995 Sand erosion of wear-resistant materials: Erosion in choke valves. *Wear* **186**, 179–188.

[37] HAWKES, JEREMY J, BARBER, ROBERT W, EMERSON, DAVID R & COAKLEY, W TERENCE 2004 Continuous cell washing and mixing driven by an ultrasound standing wave within a microfluidic channel. *Lab on a Chip* **4** (5), 446–452.

[38] HAWKES, JEREMY J, BARBER, ROBERT W, EMERSON, DAVID R & COAKLEY, W TERENCE 2004 Continuous cell washing and mixing driven by an ultrasound standing wave within a microfluidic channel. *Lab on a Chip* **4** (5), 446–452.

[39] HAWKES, JEREMY J & COAKLEY, W TERENCE 2001 Force field particle filter, combining ultrasound standing waves and laminar flow. *Sensors and Actuators B: Chemical* **75** (3), 213–222.

[40] HAWKES, JEREMY J, LONG, MICHAEL J, COAKLEY, W TERENCE & MCDONNELL, MARTIN B 2004 Ultrasonic deposition of cells on a surface. *Biosensors and Bioelectronics* **19** (9), 1021–1028.

[41] HERTZ, HM 1995 Standing-wave acoustic trap for nonintrusive positioning of microparticles. *Journal of applied physics* **78** (8), 4845–4849.

[42] HILL, MARTYN & HARRIS, NICHOLAS R 2007 Ultrasonic particle manipulation. In *Microfluidic technologies for miniaturized analysis systems*, pp. 357–392. Springer.

[43] HILL, MARTYN & WOOD, ROBERT JK 2000 Modelling in the design of a flow-through ultrasonic separator. *Ultrasonics* **38** (1-8), 662–665.

[44] HIRT, C.W & NICHOLS, B.D 1981 Volume of fluid (vof) method for the dynamics of free boundaries. *Journal of Computational Physics* **39** (1), 201–225.

[45] HOU, RONG, WANG, TAO, LV, ZHE & FENG, YANSEN 2018 Apparatus developments of ultrasonic vibration-assisted microabrasive waterjet polishing. *Advances in Materials Science and Engineering* **2018**, 1–9.

[46] HULTSTRÖM, JESSICA, MANNEBERG, OTTO, DOPF, KATJA, HERTZ, HANS M, BRISMAR, HJALMAR & WIKLUND, MARTIN 2007 Proliferation and viability of adherent cells manipulated by standing-wave ultrasound in a microfluidic chip. *Ultrasound in medicine & biology* **33** (1), 145–151.

[47] HUTCHINGS, IM 1981 A model for the erosion of metals by spherical particles at normal incidence. *Wear* **70** (3), 269–281.

[48] HUTCHINGS, IAN M 1992 Ductile-brittle transitions and wear maps for the erosion and abrasion of brittle materials. *Journal of Physics D: Applied Physics* **25** (1A), A212.

[49] INC, ANSYS 2013 Ansys fluent theory guide. *ANSYS, Inc Canonsburg* pp. 90311–2.

[50] JOHNSON, DWAYNE A & FEKE, DONALD L 1995 Methodology for fractionating suspended particles using ultrasonic standing wave and divided flow fields. *Separations Technology* **5** (4), 251–258.

[51] KARIMI, A, YAZDI, S & ARDEKANI, AM 2013 Hydrodynamic mechanisms of cell and particle trapping in microfluidics. *Biomicrofluidics* **7** (2).

[52] KHANOUKI, HADI ARABNEJAD 2015 Development of erosion equations for solid particle and liquid droplet impact. PhD thesis, The University of Tulsa.

[53] KING, LOUIS VESSOT 1934 On the acoustic radiation pressure on spheres. *Proceedings of the Royal Society of London. Series A-Mathematical and Physical Sciences* **147** (861), 212–240.

[54] KLEIS, I, UUEMOIS, H, UKSTI, L, PAPPEL, T, GP, TILLY & SAGE, W 1975 Comments on" a two stage mechanism of ductile erosion". reply. .

[55] KÖNIG, WALTER 1891 Hydrodynamisch-akustische untersuchungen. *Annalen der Physik* **279** (5), 43–60.

[56] KREFT, JENNIFER, CHEN, YENG-LONG & CHANG, HSUEH-CHIA 2008 Conformation and trapping rate of dna at a convergent stagnation point. *Physical Review E—Statistical, Nonlinear, and Soft Matter Physics* **77** (3), 030801.

[57] LEVY, ALAN V 1995 *Solid particle erosion and erosion-corrosion of materials*. Asm International.

[58] LEVY, ALAN V & CHIK, PAULINE 1983 The effects of erodent composition and shape on the erosion of steel. *Wear* **89** (2), 151–162.

[59] LI, SIMON KA-KEUNG, HUMPHREY, JOSEPH AC & LEVY, ALAN V 1981 Erosive wear of ductile metals by a particle-laden high velocity liquid jet. *Wear* **73** (2), 295–309.

[60] LIEBHARD, MARKUS & LEVY, ALAN 1991 The effect of erodent particle characteristics on the erosion of metals. *Wear* **151** (2), 381–390.

[61] LIU, YANG & LIM, KIAN-MENG 2011 Particle separation in microfluidics using a switching ultrasonic field. *Lab on a Chip* **11** (18), 3167–3173.

[62] MANDRALIS, ZENON I & FEKE, DONALD L 1993 Continuous suspension fractionation using acoustic and divided-flow fields. *Chemical engineering science* **48** (23), 3897–3905.

[63] MANSOURI, AMIR 2016 A combined cfd-experimental method for developing an erosion equation for both gas-sand and liquid-sand flows. PhD thesis, The University of Tulsa.

[64] MANSOURI, AMIR, ARABNEJAD, HADI, KARIMI, SOROOR, SHIRAZI, SIAMACK A & MCLAURY, BRENTON S 2015 Improved cfd modeling and validation of erosion damage due to fine sand particles. *Wear* **338**, 339–350.

[65] MASUDO, TAKASHI & OKADA, TETSUO 2006 Particle separation with ultrasound radiation force. *Current Analytical Chemistry* **2** (2), 213–227.

[66] MATSUMURA, T, MURAMATSU, T & FUEKI, S 2011 Abrasive water jet machining of glass with stagnation effect. *CIRP annals* **60** (1), 355–358.

[67] MCLAURY, BRENTON SCOTT 1996 *Predicting solid particle erosion resulting from turbulent fluctuations in oilfield geometries*. The University of Tulsa.

[68] MERRELL, TM & SAYLOR, JR 2017 Demisting using an ultrasonic standing wave field. *The Journal of the Acoustical Society of America* **141** (1), 172–182.

[69] MESSELINK, WILHELMUS ACM, WAEGER, RETO, WONS, TORSTEN, MEEDER, MARK, HEINIGER, KURT C & FAEHNLE, OLIVER W 2005 Prepolishing and finishing of optical surfaces using fluid jet polishing. In *Optical manufacturing and testing VI*, , vol. 5869, pp. 38–43. SPIE.

[70] MORGAN, J, SPENGLER, JF, KUZNETSOVA, L, COAKLEY, WT, XU, J & PURCELL, WM 2004 Manipulation of in vitro toxicant sensors in an ultrasonic standing wave. *Toxicology in Vitro* **18** (1), 115–120.

[71] MULLER, PETER BARKHOLT, BARNKOB, RUNE, JENSEN, MADS JAKOB HERRING & BRUUS, HENRIK 2012 A numerical study of microparticle acoustophoresis driven by acoustic radiation forces and streaming-induced drag forces. *Lab on a Chip* **12** (22), 4617–4627.

[72] NEILSON, JH & GILCHRIST, A 1968 Erosion by a stream of solid particles. *wear* **11** (2), 111–122.

[73] OBERTI, STEFANO, MOELLER, DIRK, NEILD, ADRIAN, DUAL, JURG, BEYELER, FELIX, NELSON, BRADLEY J & GUTMANN, SASCHA 2010 Strategies for single particle manipulation using acoustic and flow fields. *Ultrasonics* **50** (2), 247–257.

[74] OKA, Y ISOMOTO, MATSUMURA, M & KAWABATA, T 1993 Relationship between surface hardness and erosion damage caused by solid particle impact. *Wear* **162**, 688–695.

[75] OKA, Y ISOMOTO, OKAMURA, K & YOSHIDA, T 2005 Practical estimation of erosion damage caused by solid particle impact: Part 1: Effects of impact parameters on a predictive equation. *Wear* **259** (1-6), 95–101.

[76] PAMME, NICOLE 2006 Magnetism and microfluidics. *Lab on a Chip* **6** (1), 24–38.

[77] PENG, WENQIANG, GUAN, CHAOLIANG & LI, SHENGYI 2013 Material removal mode affected by the particle size in fluid jet polishing. *Applied Optics* **52**, 7927–33.

[78] POHL, HA, POLLOCK, K & CRANE, JS 1978 Dielectrophoretic force: A comparison of theory and experiment. *Journal of biological physics* **6**, 133–160.

[79] QI, HUAN, WEN, DONGHUI, LU, CONGDA & LI, GANG 2016 Numerical and experimental study on ultrasonic vibration-assisted micro-channelling of glasses using an abrasive slurry jet. *International Journal of Mechanical Sciences* **110**, 94–107.

[80] RAVULA, SURENDRA K, BRANCH, DARREN W, JAMES, CONRAD D, TOWNSEND, ROSEMARY J, HILL, MARTYN, KADUCHAK, GREGORY, WARD, MIKE & BRENER, IGAL 2008 A microfluidic system combining acoustic and dielectrophoretic particle preconcentration and focusing. *Sensors and Actuators B: Chemical* **130** (2), 645–652.

[81] SCHLICHTING, HERMANN 1932 Berechnung ebener periodischer grenzschichtstromungen. *Physikalische Zeit.* **33**, 327–335.

[82] SCHNELLE, THOMAS, HAGEDORN, ROLF, FUHR, GÜNTER, FIEDLER, STEFAN & MÜLLER, TORSTEN 1993 Three-dimensional electric field traps for manipulation of cells—calculation and experimental verification. *Biochimica et Biophysica Acta (BBA)-General Subjects* **1157** (3), 127–140.

[83] SETTLES, GARY S 2001 *Schlieren and shadowgraph techniques: visualizing phenomena in transparent media*. Springer Science & Business Media.

[84] SHI, CHUNYAN, YUAN, JIAHU, WU, FAN & WAN, YONGJIAN 2011 Influence of standoff distance on material removal function in fluid jet polishing. *Infrared and Laser Engineering* **40** (4).

[85] SHI, CHUNYAN, YUAN, JIAHU, WU, FAN & WAN, YONGJIAN 2011 Ultra-precision figuring using submerged jet polishing. *Chinese Optics Letters* **9** (9), 092201.

[86] SOORAJ, VS & RADHAKRISHNAN, V 2013 Elastic impact of abrasives for controlled erosion in fine finishing of surfaces. *Journal of Manufacturing Science and Engineering* **135** (5), 051019.

[87] STRUTT, JOHN WILLIAM 1884 I. on the circulation of air observed in kundt's tubes, and on some allied acoustical problems. *Philosophical Transactions of the Royal Society of London* (175), 1–21.

[88] SUGIYAMA, KENICHI, HARADA, KENJI & HATTORI, SHUJI 2008 Influence of impact angle of solid particles on erosion by slurry jet. *Wear* **265** (5-6), 713–720.

[89] TILLY, GP 1973 A two stage mechanism of ductile erosion. *Wear* **23** (1), 87–96.

[90] TURENNE, SYLVAIN, FISET, MICHEL & MASOUNAVE, JACQUES 1989 The effect of sand concentration on the erosion of materials by a slurry jet. *Wear* **133** (1), 95–106.

[91] WANG, CHUNJIN, CHEUNG, BENNY C.F., HO, LAI, LIU, MINGYU & W.B., LEE 2016 A novel multi-jet polishing process and tool for high-efficiency polishing. *International Journal of Machine Tools and Manufacture* **115**.

[92] WANG, CHUN JIN, CHEUNG, CHI FAI, HO, LAI TING & LOH, YEE MAN 2020 An investigation of effect of stand-off distance on the material removal characteristics and surface generation in fluid jet polishing. *Nanomanufacturing and Metrology* **3**, 112–122.

[93] WANG, ZHAOWEI, GRABENSTETTER, PAUL, FEKE, DONALD L & BELOVICH, JOANNE M 2004 Retention and viability characteristics of mammalian cells in an acoustically driven polymer mesh. *Biotechnology progress* **20** (1), 384–387.

[94] WEISER, MAH, APFEL, RE & NEPPIRAS, EA 1984 Interparticle forces on red cells in a standing wave field. *Acta Acustica united with Acustica* **56** (2), 114–119.

[95] YANG, JEONGWON, HWANG, HAERANG, BAE, YOUNG MIN, KIM, MOOJOON & HA, KANGLYEOL 2013 Trapping of microparticles in cylindrical standing wave fields. *Japanese Journal of Applied Physics* **52** (7S), 07HE14.

[96] YOSIOKA, KAWASHIMA & KAWASIMA, YUKIHIKO 1955 Acoustic radiation pressure on a compressible sphere. *Acta Acustica united with Acustica* **5** (3), 167–173.

[97] YU, ZONG-RU, KUO, CHING-HSIANG, CHEN, CHUN-CHENG, HSU, WEI-YAO & TSAI, DIN PING 2011 Study of air-driving fluid jet polishing. In *Optical Manufacturing and Testing IX* (ed. James H. Burge, Oliver W. Fähnle & Ray Williamson), , vol. 8126, p. 812611. International Society for Optics and Photonics, SPIE.

[98] ZHANG, Y, REUTERFORS, EP, MCLAURY, B SF, SHIRAZI, SA & RYBICKI, EF 2007 Comparison of computed and measured particle velocities and erosion in water and air flows. *Wear* **263** (1-6), 330–338.